Radiation damage produced by swift heavy ions in rare earth phosphates

Strahlenschäden durch Schwerionenbestrahlung in Seltenerd-Phosphaten

Vom Fachbereich Physik der Technischen Universität Darmstadt
zur Erlangung des Grades eines Doktors der Naturwissenschaften (Dr. rer. nat.)
genehmigte Dissertation von Mag. Anton Romanenko aus Energodar
Tag der Einreichung: 28.06.2016, Tag der Prüfung: 18.07.2016
Darmstadt, 2017 — D 17

1. Gutachten: Prof. Dr. Franz Fujara
2. Gutachten: Prof. Dr. Christina Trautmann

TECHNISCHE UNIVERSITÄT DARMSTADT

Institut für Festkörperphysik
AG Fujara
in Zusammenarbeit mit dem GSI Helmholtzzentrum für Schwerionenforschung GmbH
Bereich Materialforschung

Radiation damage produced by swift heavy ions in rare earth phosphates
Strahlenschäden durch Schwerionenbestrahlung in Seltenerd-Phosphaten

Genehmigte Dissertation von Mag. Anton Romanenko aus Energodar

1. Gutachten: Prof. Dr. Franz Fujara
2. Gutachten: Prof. Dr. Christina Trautmann

Tag der Einreichung: 28.06.2016
Tag der Prüfung: 18.07.2016

Darmstadt — D 17

Erklärung zur Dissertation

Hiermit versichere ich, die vorliegende Dissertation ohne Hilfe Dritter nur mit den angegebenen Quellen und Hilfsmitteln angefertigt zu haben. Alle Stellen, die aus Quellen entnommen wurden, sind als solche kenntlich gemacht. Diese Arbeit hat in gleicher oder ähnlicher Form noch keiner Prüfungsbehörde vorgelegen.

Darmstadt, den 13.02.2017

_____

(Anton Romanenko)

Abstract

This work is devoted to the study of radiation damage produced by swift heavy ions in rare earth phosphates, materials that are considered as perspective for radioactive waste storage. Single crystals of rare earth phosphates were exposed to 2.1 GeV gold (Au) and 1.5 GeV xenon (Xe) ions of and analyzed mainly by Raman spectroscopy. All phosphates were found almost completely amorphous after the irradiation by 2.1 GeV Au ions at a fluence of 1×10^{13} ions/cm^2. Radiation-induced changes in the Raman spectra include the intensity decrease of all Raman bands accompanied by the appearance of broad humps and a reduction of the pronounced luminescence present in virgin samples. Analyzing the Raman peak intensities as a function of irradiation fluence allowed the calculation of the track radii for 2.1 GeV Au ions in several rare earth phosphates, which appear to be about 5.0 nm for all studied samples. Series of samples were studied to search for a trend of the track radius depending on the rare earth element (REE) cation. Among the monoclinic phosphates both Raman and small-angle X-ray scattering (SAXS) suggest no significant change of the track radius with increasing REE mass. In contrast, within the tetragonal phosphates Raman spectroscopy data suggests a possible slight decreasing trend of the track radius with the increase of REE atomic number. That finding, however, requires further investigation due to the low reliability of the qualitative Raman analysis. Detailed analysis of Raman spectra in $HoPO_4$ showed the increase of peak width at the initial stage of the irradiation and subsequent decrease to a steady value at higher fluences. This observation suggested the existence of a defect halo around the amorphous tracks in $HoPO_4$. Raman peaks were found to initially shift to lower wavenumbers with reversing this trend at the fluence of 5×10^{11} for $NdPO_4$ and 1×10^{12} ions/cm^2 for $HoPO_4$. At the next fluence steps peaks moved in the other direction, passed positions assigned for virgin materials and moved even further at the fluence step of 1×10^{13} ions/cm^2. This study has also shown that variation of beam parameters could drastically affect material degradation. Increase of Au ion flux was shown to produce partial sample annealing, most likely due to macroscopic temperature increase. At the same time the increase of 1.5 GeV Xe ion beam pulse intensity was shown to invoke enhanced amorphization in comparison to beams of low pulse intensity.

Zusammenfassung

Diese Arbeit widmet sich der Erforschung von Strahlenschäden durch hochenergetische Schwerionen in Phosphaten der seltenen Erden, Materialien die vielleicht neue Lösungen für die Lagerung von radioaktiven Abfällen ermöglichen. Einkristalle der Phosphate der seltenen Erden wurden Ionenstrahlen aus Gold und Xenon mit einer jeweiligen Energie von 2.1 GeV bzw. 1.5 GeV ausgesetzt und anschließend analysiert, hauptsächlich durch Ramanspektroskopie. Nach der Bestrahlung mit 1×10^{13} Goldionen/cm^2 mit einer Energie von 2.1 GeV konnte in allen untersuchten Phosphaten eine fast vollständige Amorphisierung festgestellt werden. Die strahleninduzierten Materialveränderungen konnten auch in den Ramanspektren festgestellt werden. Nach Bestrahlung ist vorallem ein starker Intensitätsabfall der Ramanbanden und der Lumineszenz gegenüber den unbestrahlten Proben auffällig. Zusätzlich sind in den bestrahlten Proben breite, für amorphe Materialien typische Banden zu erkennen. Die Analyse der Intensitäten der Ramanbanden erlaubt die Berechnung des Ionenspurradius für 2.1 GeV Gold-Ionen, der in fast allen untersuchten Phosphaten um die 5.0 nm beträgt. Die Probenserie wurde untersucht, um einen Trend des Ionenspurradius in Abhängikeit des jeweiligen Cations der seltenen Erden (rare earth element cation - REE) festzustellen. Die Ergebnisse sowohl von Ramanspektroskopie als auch klein-Winkel Röntgenbeugung (SAXS) weisen darauf hin, dass bei den monoklinischen Phosphaten der Ionenspurradius und die REE-Masse in Proportion stehen, wobei der Trend marginal ist. In tetragonalen Phosphaten weisen die Ergebnisse der Ramanspektroskopie auf eine umgekehrte Proportionalität zwischen Spurradius und REE-Masse hin. Diese Befunden benötigen allerdings weitere Nachforschungen wegen der geringen Reliabilität der durchgeführten qualitativen Ramananalyse. Die detaillierte Analyse der Ramanspektren von $HoPO_4$ zeigte beim ersten Fluenzschritt zunächst eine Verbreiterung des Ramanbandes, bei fortgesetzter Bestrahlung lässt sich allerdings eine Verengung des Bandes feststellen, die zu höheren Fluenzen hin saturiert. Diese Beobachtung weist darauf hin, dass in diesem Material bei der Bestrahlung Defekthalos um die amorphen Ionenspuren herum entstehen. Ab Fluenzen von 5×10^{11} Ionen/cm^2 für $NdPO_4$ bzw. 1×10^{12} Ionen/cm^2 für $HoPO_4$ verschieben sich die Ramanbanden hin zu niedrigeren Wellenzahlen. Bei weiterer Bestrahlung verschieben sich die Banden zurück zu den Werten des unbestrahlten Materials und bei Fluenzen größer als 1×10^{13} Ionen/cm^2 sogar hin zu höheren Wellenzahlen. Diese Untersuchung hat ebenfalls gezeigt, dass eine Veränderung der Ionenstrahlparameter die Materialdegradierung drastisch beeinflussen kann. Es wurde nachgewiesen, dass eine Erhöhung des Gold-Ionenflux ein partielles Ausheilen der Probe zur Folge hat, das wahrscheinlich durch die makroskopische

Temperaturerhöhung zu erklären ist. Gleichzeitig wurde gezeigt, dass eine Erhöhung der Pulsintensität beim 1.5 GeV Xenon-Ionenstrahl eine verstärkte Amorphisierung im Material auslöst.

Contents

List of Figures

List of Tables

List of Abbreviations

- SRIM - The Stopping and Range of Ions in Matter
- SHI - swift heavy ions
- UNILAC - Universal Linear Accelerator
- SIS - (*in german*) Schwerionensynchrotron
- SETRAM - secondary electron transmission monitor
- Ln - Lanthanides
- REE - rare earth elements: include all Lanthanides, scandium (Sc) and yttrium (Y);
- XRD - X-ray diffraction
- SAXS - small-angle X-ray scattering
- TEM - transmission electron microscopy
- SEM - scanning electron microscopy
- AFM - atomic force microscopy

1 Introduction

The discovery of the internal structure of atoms, objects, that even by their given name ($\acute{\alpha}\tau o\mu o\varsigma$) were considered to be the smallest existing unit, is undeniably the most important breakthrough in the modern history of science. Nuclear energy accumulated inside of atoms with a size millions times smaller than dust particles - makes the beautiful night sky shining with myriads of glittering stars, provides electricity to many millions of people's homes - and is equally capable of creating devastating weapons. Intelligent handling of atomic power requires not only approaching situation in the rational, deliberate and humanistic way, but also being fully aware and prepared for the treatment of possible consequences and aftereffects. Among all the problems that nuclear engineers and scientists seek answers for, the safe long term disposal of generated radioactive waste remains one of the very first, urgent, and yet not completely solved tasks [1]. Despite the development of alternative energy sources over the last decades, the nuclear energy still remains the only solid alternative to conventional fossil fuels that produces no CO_2 emission and outperforms it on 3 to 5 orders of magnitude in severe risk indicators [2]. It also provides the lowest ratio of accident risks (frequency of severe accidents) to the amount of electricity produced among all the known energy sources. Having in addition one of the lowest total costs, nuclear energy is also one of the most sustainable energy sources nowadays [3]. So, desirable economical benefit from one of the most prominent energy sources, requires a solution to the problem of the disposal of accumulated waste over an extremely long time period [4]. To visualize the scale of the problem, it should be mentioned, that solely in the countries belonging to the Organization for Economic Cooperation and Development (OECD), the annual amount of produced radioactive waste is around 81,000 m^3 [5]. The main sources of radioactive waste are the high-level waste (HLW) that originates from the spent nuclear fuel itself [6] and waste generated from the reprocessing of burned nuclear fuel, and plutonium retrieved from dismantled nuclear weapons or obtained in the reprocessing of nuclear fuel [7]. Other types of waste account for large volumes, but produce rather little radioactivity compare to the previously mentioned ones [5].

One of the promising solutions to the problem of radioactive waste handling is its incorporation in a waste-bearing material (waste form) and subsequent disposal in a geologic repository [8, 9]. This approach puts certain requirements on the properties of a waste form: a) it should readily incorporate actinides into its structure; b) it should have chemical stability and durability on a large time-scales (more than hundreds of thousand years); c) it should have high resistance to radiation damage [9].

To date, numerous materials have been studied for the role of waste form, in particular for immobilization of actinides [10] and plutonium [11] including but not limited to:

- simple oxides: zirconia (ZrO_2), uraninite (UO_2), thorianite (ThO_2);
- complex oxides: pyrochlore ($(Na,Ca,U)_2(Nb,Ti,Ta)_2O_6$), muratanite ($(Na,Y)_4(Zn,Fe)_3(Ti,Nb)_6O_{18}(F,OH)_4$), zirconolite ($CaZrTi_2O_7$);
- silicates: zircon ($ZrSiO_4$), thorite ($ThSiO_4$), garnet ($(Ca,Mg,Fe^{2+})_3(Al,Fe^{3+},Cr^{3+})_2(SiO_4)$), britholite ($(Ca,Ce)_5(SiO_4)_3(OH,F)$), titanite ($CaTiSiO_5$);
- titanates: pyrochlore (Ca, REE)Ti_2O_7;
- phosphates: monazite (LnPO4), apatite ($Ca_{4-x}Ln_{6+x}(PO_4)_y(O,F)_2$), xenotime ($YPO_4$).

From this list of compounds, a long-term durability is confirmed by study of naturally occurring minerals for several silicates (zircon, thorite, garnet) and all listed phosphates (monazite, apatite and xenotime). Thus, phosphates play an important role in consideration as nuclear waste hosts and this concerns various crystal structures - including hexagonal apatite, monoclinic monazite and tetragonal xenotime [7]. Due to its remarkable properties, monazite is probably the most studied phosphate. This rare earth phosphate crystallizes into the monoclinic ($P2_1/n$) structure. Natural monazite ($(Ce,REE)PO_4$) could hardly be found in the amorphous state [7, 12], indicating either the high radiation hardness, or low temperature for recrystallization. Natural monazite can incorporate actinides into its structure e.g. $(REE,Th)PO_4$. It has long-term chemical durability and is often present in rocks and sands. It is an abundant mineral what allows systematic research of radiation damage accumulated for decades due to self-irradiation from actinides that were present in the mineral [13].

In irradiation experiments performed at laboratory conditions, both natural and synthetic rare earth phosphates were successfully amorphized by ion beams of various energies. Both tetragonal YPO_4 and monoclinic $(Ce,La,Y)PO_4$ were found in metamict (disordered) state after irradiation with 3 MeV Argon ions [14]. Systematic studies of natural monazite and the series of synthetic pure rare earth element phosphates (REE-PO_4) have shown amorphization by 800 keV Kr ion bombardment, with the trend of monoclinic structure having lower temperatures where recrystallization starts in comparison to the tetragonal phosphates. Furthermore, the same authors observed a trend of critical amorphization temperature increasing with the increase of the atomic number of rare earth cations [15]. Irradiations performed in $LaPO_4$ and $ScPO_4$ with 1.5 MeV Kr ions have shown that larger energies lead to an increase of the critical amorphization dose and a decrease of the recrystallization temperature [12]. This finding raised the question how the different ion energy regimes contribute to the resulting damage production. Radiation hardness of different rare earth phosphates is of great interest not only due the possible application as nuclear waste host materials, but also for the development of a general understanding of the material response to ion irradiation.

Interaction of energetic heavy ions with solids strongly depends on their kinetic energies. At low kinetic energies below 1 MeV/u radiation induced changes in the material are induced in the regime of a nuclear energy loss. During this process the incoming ion transfer the energy to the material via creation of collision cascades. Response of different materials including rare earth phosphates to the damage in this regime is well understood. At specific projectile ion energies above 1 MeV/u, the slowing down of the ions is given by the electronic energy loss. The electronic energy loss describes inelastic interaction of charged energetic ions with the electronic subsystem of the solid. Description of energy transfer during the electronic energy loss requires completely different models and more delicate approach due to the complications with the extremely short interaction times, damage localization and interaction of incoming ion with the electronic subsystem of a solid [16].

Despite of existence of models that can use particular criteria to explain existed radiation hardness of one material compared to another, the predictive capability of current models is far from optimum. Analysis of crucial factors for radiation hardness involves considerations of chemical bonding character [17], bonding type (bond ionicity, competition of long-range ionic and short-range covalent forces), glass-forming ability and crystalline structure [18]. The neutron irradiation experiments are well established, so extended data concerning the material response in the regime of nuclear stopping is available in literature [19]. In contrast, irradiation where electronic stopping dominates is achievable by the irradiations with heavy ions and require usage of big machines - ion accelerators. With the development of machinery and resulting rise of projectile's kinetic energy, the heavy ions impacting the solid introduced the phenomena of ion tracks - the extended damaged area around the projectile ion trajectory of typical diameter about 10 nm.

The phenomenon of ion track formation has been observed in many materials including simple (oxides, halides, nitrides etc) [20–22] and complex compounds (silicates, zirconates, titanates etc) [23–28] for the case of semiconductors, insulators, amorphous materials and some metals [20]. Electronic excitations as primary cause of ion track formation, produce different effects ranging from the creation of color centers (with the preservation of crystallinity) in alkali halides [29] to the production of amorphous tracks in many insulators [21, 28, 30]. The electronic energy loss, the amount of energy that an impacting ion releases per unit of its path within the material, plays an important role in the ion track formation. In most materials there seems to be a threshold value for the electronic energy loss to initiate the process of ion track formation, where close to the critical energy deposition ion tracks start to be discontinuous and below this value to not form tracks at all [26–28]. The track morphology can be rather complex. In e.g. SiO_2 ion tracks are reported having a low dense track core surrounded by high density shell structure [21]. In pyrochlores the track radius and morphology correlate with the chemical composition and ratio of cation radii [22, 28, 31]. The description of ion track phenomena in variety of materials considers the amount and mobility of excited electrons, electron-phonon

coupling for energy transfer to the lattice, the material's thermal conductivity in the process of energy diffusion from the overheated area along the ion path, rate of defect recombination and other parameters [20]. Many different models try to explain this complicated nature of the process of ion track formation but their predictive efficiency still requires further developments. That dictates a demand for more experimental data on observations of ion tracks in individual materials as well as in series of closely related compounds.

This work will shed some light on the response of series of phosphates of rare earth elements to the radiation damage induced by swift heavy ions. Several pure synthetic phosphates of monoclinic monazite-type [Pr, Nd,Sm,Eu]PO_4 and tetragonal xenotime-type [Y, Tm,Ho,Lu]PO_4 structures were irradiated by 2.1 GeV ^{197}Au ions covering a broad fluence regime from single to largely overlapping ion tracks (from 5×10^{11} ions/cm^2 up to 5×10^{13} ions/cm^2). All materials were found to be completely amorphous at the highest fluence. Raman spectroscopy measurements allowed the determination of amorphization rates and damage cross-sections for some of the compounds. Values of ion track radii for monazite-type phosphates were supported by transmission electron microscopy (TEM) and small angle X-ray scattering (SAXS) measurements. The analysis of Raman peak shifts indicated the unusual behavior in comparison with naturally metamict samples: Raman peaks initially shift to the lower wavenumbers, while at the fluences between 5×10^{12} and 1×10^{12} ions/cm^2 this trend reverses. This shift was explained by the appearance of defect halo around the amorphous track. Ion flux was found to play significant role on the material amorphization. Irradiation of with the Au ion beam of high flux (10^9 ions/cm^2·s) was shown to induce less amorphization than Au ion beam of 10^8 ions/cm^2·s flux. This partial damage recovery appeared most likely due to macroscopic sample heating. Irradiations by 1.5 GeV Xe ion beams having low and high pulse intensity showed difference in the material response depending on the ion beam conditions. The rise of overall background level and increased intensity of a broad hump at the region of stretching modes suggest the increase of amorphous material fraction for the high pulse intensity Xe ion beam. Raman spectra of samples irradiated under the low pulse intensity ion beam have higher Raman peak shifts relative to the initial position, than for the high pulse intensity beam. This suggests that the irradiation with the high pulse intensity produces an increased amorphization and reduced amount of defected halos.

2 Theory

2.1 Radiation damage in solids

2.1.1 Ion-solid interaction

Radiation damage appears when material is exposed to neutrons, ions, electrons or gamma rays. All these types of radiation may cause the displacements of atoms from their regular position in the lattice. Radiation damage results in changes of the crystalline structure of the exposed material and consequently modify different physical properties. One of the most well-known examples is radiation damage induced by neutrons in nuclear reactors, where different components were shown to suffer from changes in shape and volume (swelling), severe increase of hardness, embrittlement and cracking ([32, 33]). Interaction of an incident projectile with the material in case of neutrons is done by the kinetic energy transfer from the incoming particle with lattice atom. Incident particle together with displaced atom (also called as primary knocked-on atom) propagate in the solid creating additional knock-on atoms forming collision cascade.

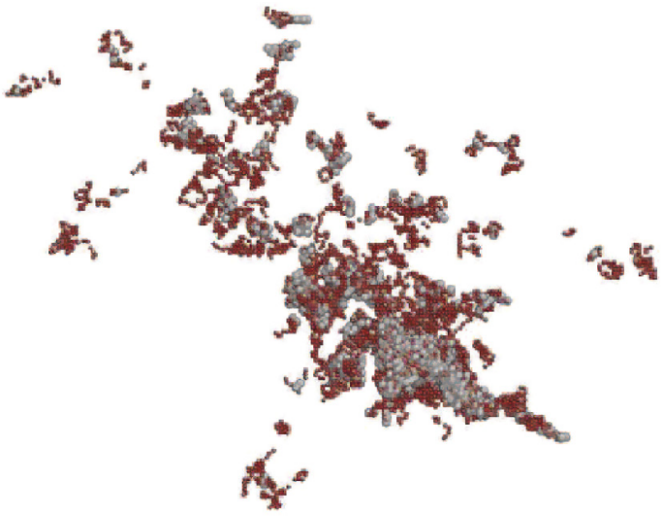

Figure 2.1: Molecular dynamic simulations of radiation damage produced by 100 keV U in TiO_2. Recoil moves from upper left to bottom right corner of the image. The image shows atoms displaced more that on 1 Å [34].

This displacement process appears in the solid up to the moment when the energy transfer to the lattice atoms surpasses the critical displacement energy. Below this threshold creation of

defects is not possible. Propagating through solid, swift heavy ion slows down because of energy transfer to surrounding material and in most cases the formation of disordered, continuous region along the ion trajectory could be observed. To describe the amount of kinetic energy that ions lose per unit of ion path length, the energy loss could be written as:

$$S(E) = -\frac{\partial E}{\partial x} \tag{2.1}$$

The typical unit for the energy loss is [keV/nm]. To be able to compare kinetic energies of different atoms usually the specific energy is used which is the ratio of the total ion energy to the amount of nuclei it has (MeV per nucleon, MeV/u). At specific energies lower than ∼100 keV/u, the interaction of ions is similar to the situation with neutrons and the energy transfer appears due to direct collisions of the incoming particle with lattice atoms and subsequent collision cascades. This is the so-called regime of nuclear energy loss $S_n(E)$ or nuclear stopping power. Simulations with the SRIM code show that maximum nuclear stopping power reaches a value as high as 5 keV/nm when irradiating $LaPO_4$ with Au ions.

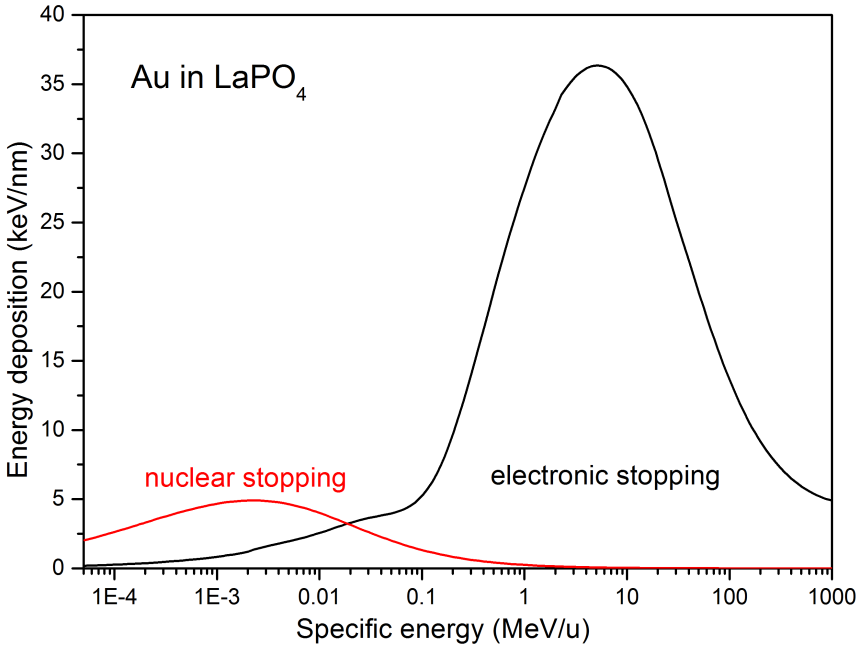

Figure 2.2: Electronic and nuclear energy loss contributions as a function of specific energies of Au ions slowing down in $LaPO_4$. Simulations performed in SRIM-2010 code [35].

In contrast to neutrons, where the energy transfer appears due to elastic interaction with lattice atoms, radiation damage done by swift heavy ions at higher energies (>100keV/u) is more complicated and includes the following processes:

- Excitation and ionization of target atoms so called electronic stopping dominating in the MeV - GeV energy range;
- Nuclear reactions appear above the Coulomb barrier;

- Generation of photons (Bremsstrahlung, Cherenkov radiation) that appear at relativistic velocities and energies above GeV.

Dominant process during swift heavy ion irradiation at high energies is excitation in electronic stopping regime. That gives interaction times in order of 10^{-17} s that are too short to interact with the lattice ions (typical phonon propagation will give 10^{-13} to 10^{-14} s). Thus energy loss from projectile to the material initially is done due to ionization of lattice atoms and energy transfer to electron subsystem. To describe interaction of charged particle with the electron subsystem in the material, we can use Bethe formula:

$$-\frac{\mathrm{d}E}{\mathrm{d}x} = \frac{4\pi}{m_e c^2} \cdot \frac{nz^2}{\beta^2} \cdot (\frac{e^2}{4\pi\varepsilon_0})^2 \cdot [ln\frac{2m_e c^2\beta^2}{I \cdot (1-\beta^2)} - \beta^2] \tag{2.2}$$

$$\beta = \frac{v}{c} \tag{2.3}$$

with:

- v the speed of particle,
- n - electron density of the material,
- z - projectile charge,
- E - kinetic energy,
- c - speed of light,
- e and m_e - electron charge and mass,
- ε_0 - vacuum permittivity.

Here the electron density of sample material could be calculated using formula [36]:

$$n = \frac{N_a \cdot Z \cdot \rho}{A \cdot M_u} \tag{2.4}$$

with:

- ρ - density of target material,
- Z - atomic number,
- A and M_u - relative atomic mass of material and its molar mass constant,
- N_A - Avogadro number.

The electronic energy loss of charged particle is proportional to the electron concentration, some function $\varphi(v) \sim \frac{1}{v^2}$, scales with the square of particle effective charge (z^2) and is independent of particle mass M.

The total energy deposition of swift heavy ions can be written as the sum of nuclear and electronic energy losses: $S_{tot} = S_e + S_n$. At different specific energies interaction is done suing different mechanisms and formation of resulted damage to the material will depend on the ratio of electronic and nuclear stopping power.

2.1.2 Formation of ion tracks

In many solids the passage of energetic charged particle creates the continuous damaged zone along the ion trajectory. In regime of nuclear energy loss, the incoming ion (together with the knocked-on atoms due to direct collisions with atoms of material), perform scattering on large angles. As a result, the collision cascades with large longitudinal straggling are formed. Material modification is done via the accumulation of such damage cascades.

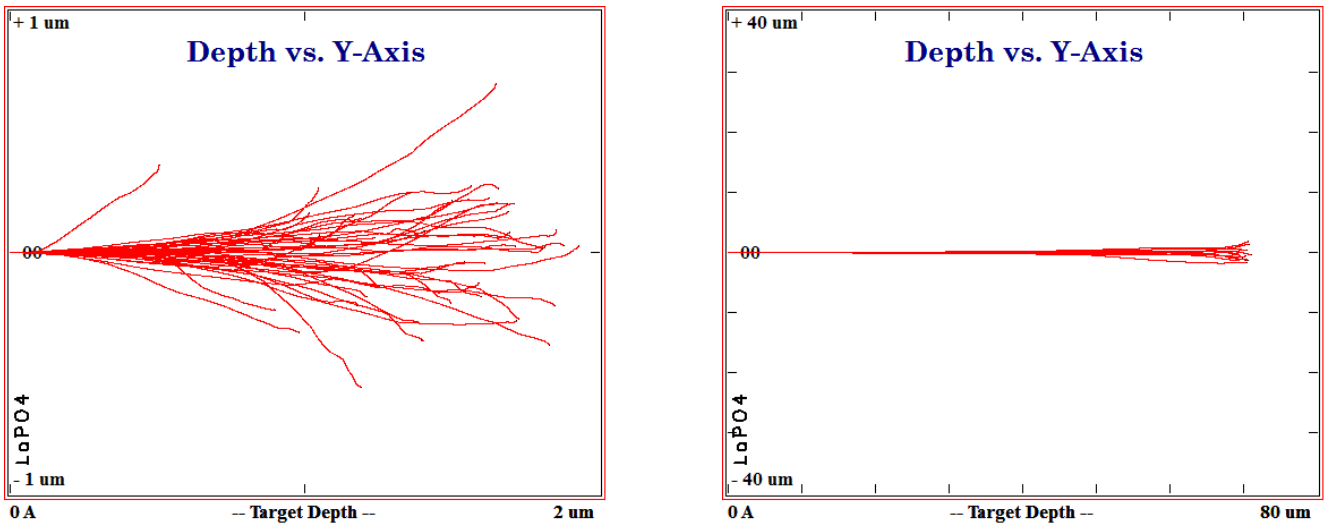

Figure 2.3: SRIM simulation of damage cascades done by 100 keV/u and 0.5 MeV/u Au ions in $LaPO_4$.

At higher specific energies (above 1 MeV/u), a different mechanism plays role in the energy transfer from the projectile to the solid. Incoming particle interacts with the electron subsystem creating the ionization cascades. The electrons resulting from the primary ionization travel in the radial direction from the track core creating secondary ionization cascades [37]. Interaction of incoming particle with the electrons leads to the ion trajectory being a straight line. Only at the very end of the ion path, the formation of collision cascades results in the ion scattering and large longitudinal straggling. If material cannot maintain / regain its structure in the region affected by the passing energetic ion, the damaged region, so called ion track, is formed along the ion trajectory. Ion tracks have a typical radius of several nanometers [38] and length of

few tenth of nanometers depending on the impacting ion energy and target material (details of ion-matter interaction were discussed in previous section).

Despite the fact that ion tracks are known and studied for already several decades, there is still no universal theoretical model providing a comprehensive description of track formation in solids. One of the models applied is the Coulomb explosion. Excitation of valence-band electrons along the impacting ion trajectory creates an array of charged ions of a sample material. A large electrostatic repulsion of the formed ion cloud acts as driving force to displace atoms from their lattice positions [39, 40]. Repulsed atoms traveling in radial directions away from the ion trajectory induce atom rearrangements and formation of large stresses in the material [41].

Another model that is widely used for the description of ion track formation in solids is the inelastic thermal spike model. Initial stage of ion-solid interaction results in the heating up of the electronic subsystem of sample material. On later stages the energy is transferred to the atoms heating them up. Temperature increase high enough for the material reaching its melting point accompanied by the rapid quenching form an ion track. According to the inelastic thermal spike, the target material is considered as two-component system: atomic lattice and electrons with respective temperatures T_a and T_e [42]. Projectiles deposit their energy initially to the electron subsystem which is in a later process transferred to the atom. To describe energy transfer from "hot" electrons to the lattice, a set of coupled time-dependent thermal diffusion equations is used (eqs. (2.5) and (2.6)). The thermal spike creates defects via thermal activation and they remain as "frozen defects" along the ion path due to rapid quenching of the temperature after energy diffuses away from ion trajectory [40, 43].

$$\rho C_e \frac{\partial T_e}{\partial t} = \nabla[K_e \nabla T_e] - g(T_e - T_l) + E(r,t) \tag{2.5}$$

$$\rho C_l(T_l) \frac{\partial T_l}{\partial t} = \nabla[K_l(T_l) \nabla T_l] + g(T_e - T_l) \tag{2.6}$$

with:

- ρ material density,
- C_e and C_l respective electronic and lattice specific heat,
- K_e and K_l electronic and lattice heat conductivity,
- g is coupling constant,
- $E(r,t)$ energy excitation profile.

Within a thermal spike model, the electronic $T_e(r,t)$ and lattice $T_l(r,t)$ temperatures are calculated as a function of the radius and a time for given energy excitation profile $E(r,t)$. The

coupling coefficient g depends on T_e and hence on the electron energy spectrum and processes of electron-phonon coupling. The main parameters of this model are the mean thermal diffusion of electrons (λ) and the mean electron-phonon relaxation time (τ):

$$\lambda = \sqrt{D_e \tau} = \sqrt{\frac{K_e \tau}{\rho C_e}} \qquad \text{and} \qquad \tau = \frac{\rho C_e}{g} \tag{2.7}$$

where D_e is the thermal diffusivity of the hot electrons. Due to electron-phonon collisions, energy in the electron subsystem is transferred to the lattice. The atom system heats up and may surpass melting point of the material. Subsequent rapid cooling results in quenching of the melting region [42].

Despite the legitimate criticism [44], this model well describes track radii observed in many different materials after the irradiation. Although within last years we can observe a constant development in theories of ion track formation, a variety of processes and effects still cannot be described. It leaves an open space for future modification and development of our knowledge and understanding of complicated processes appearing during ion track formation.

2.2 Raman spectroscopy

Inelastic scattering of light was predicted by the Austrian physicist Adolf Smekal in 1923 and was observed experimentally by the Indian physicist Chandrasekhara Venkata Raman in 1928. For that observation Raman was awarded the Nobel Prize in physics in 1930. During the scattering of light, predominantly elastic scattering occurs, denoted as Rayleigh scattering (appears with the conservation of energy). At a much lower probability, also inelastic light scattering is observed, so-called Raman scattering, due to dissipation or gain of energy to / from various excitations. These excitations can be vibrations in molecules (vibrons), lattice vibrations in crystalline solids (phonons) or spin excitations in systems with magnet-order transitions (magnons). Raman spectroscopy has the advantage that no special sample preparation is required. It allows the analysis of small sample volumes ($< 1\mu$m in diameter) and examination and characterization of a large variety of materials (minerals, polymers, ceramics, organic materials).

During the Raman spectroscopy measurements the sample is typically irradiated with monochromatic laser light. Scattered light contains Rayleigh scattering at the incident beam wavelength and Raman scattering, with the wavelength shifted to the frequencies $\nu_0 \pm \nu_{ex}$, where ν_{ex} corresponds to the vibrational frequency of excitation: vibrons, phonons etc.

The Raman intensity is only 10^{-5} - 10^{-8} of incident beam, while Rayleigh scattering is several orders of magnitude stronger. That is why the broad development and boost of sensitivity of the Raman technique was obtained only after the invention of lasers in 1960s. Raman effect can be described with the help of fig. 2.4.

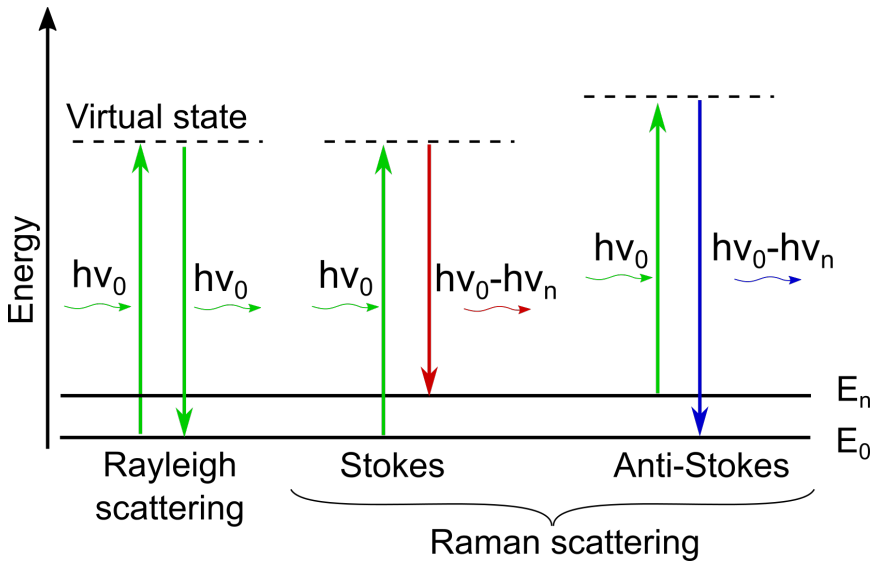

Figure 2.4: Quantum mechanical representation of Rayleigh and Raman scattering.

According to the Boltzmann distribution ($N \sim e^{-\frac{E}{kT}}$) at room temperature most of molecules are in the lowest energy state. When exposed to laser light, incoming electromagnetic wave interacts with the electrons and causes ion polarization. This is described as excitation of the molecules to the virtual state. Energy levels of this virtual states are determined by the wavelength of incoming laser light. During elastic Rayleigh scattering molecules return to their initial energy state what causes emission of light with the frequency equal to excitation one. However molecule could make transition from virtual state to the higher energy vibrational state and thus emit light with the energy smaller than the excitation wavelength (Stokes scattering). At room temperature some molecules appear already in the excited vibrational state and the same sequence will lead to emitting of light with larger energy (anti-Stokes scattering). The amount of molecules at ground state is always much larger, that is why most Raman spectroscopy measurements are based on the more intense, Stokes lines (fig. 2.5).

Alternatively to Raman spectroscopy, we can simply tune the excitation wavelength of laser until the energy difference between ground and vibrational states of a molecule (fig. 2.4), and light is absorbed at this particular energy. This method is called Infrared spectroscopy (excitation light wavelength lies in the infrared region of the electromagnetic spectrum) and gives similar and complementary information to Raman spectroscopy. Classically the Raman scattering is described by the time-dependent polarization of molecules. Excitation of a molecule with the electric filed $E = E_0 cos(\omega t)$ of electromagnetic radiation, leads to the following dipole moment p:

$$p = \mu_0 + \alpha E \tag{2.8}$$

where μ_0 is the permanent and αE the induced dipole moment.

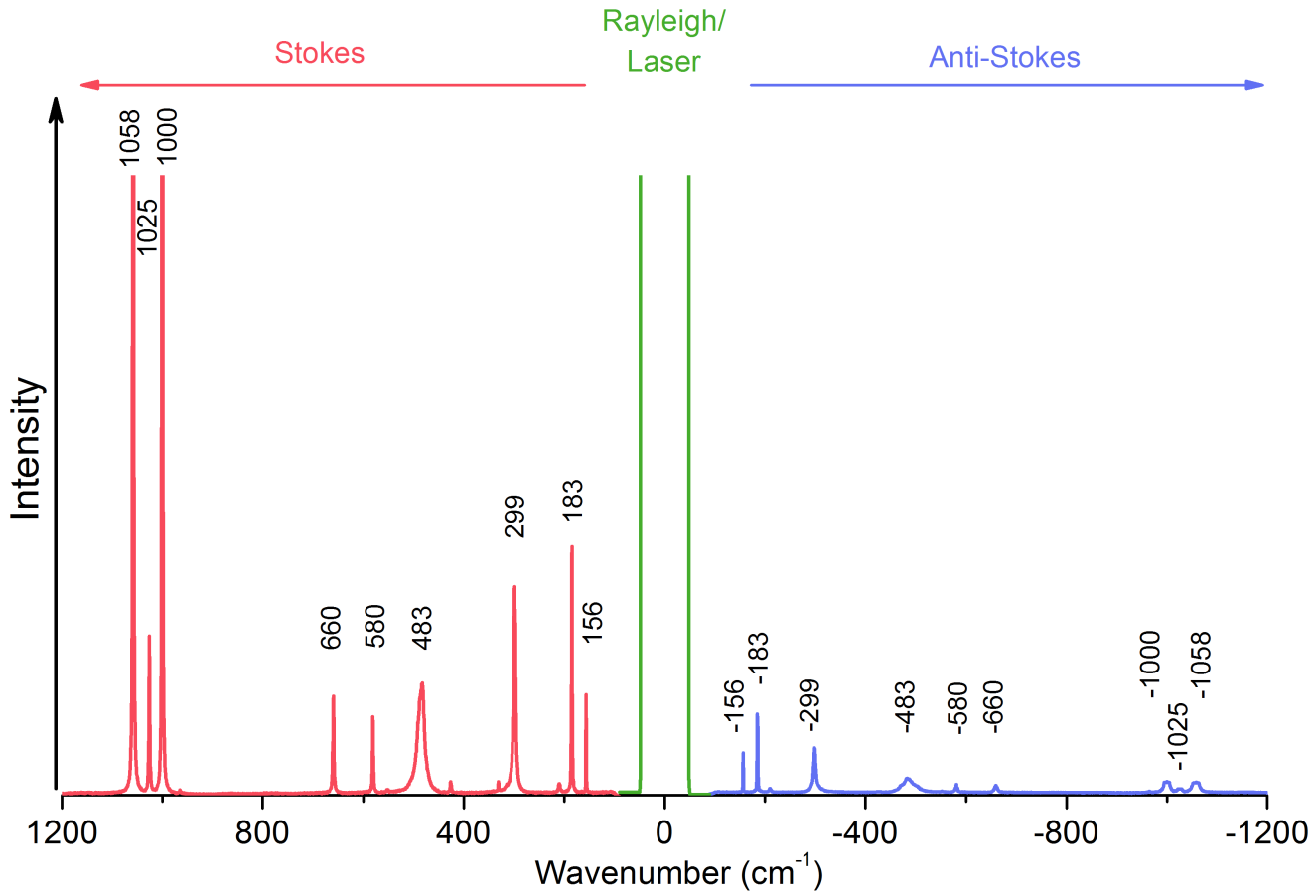

Figure 2.5: Schematic representation of Stokes and anti-Stokes scattering.

The polarizability (α) of a molecule is represented by a second order tensor with components α_{ij} and depends on the symmetry of the molecule. Small vibrations are assumed to be harmonic and then the normal coordinates $q_n(t)$ of vibrating molecules are approximated as $q_n(t) = cos(\omega_n t)$, where q_n is the amplitude and ω_n the frequency of the normal mode n. If we include it in eq. (2.8) and make the power series expansion of q_n, μ and α, the total dipolar moment (leaving only first order terms) we can described as:

$$\begin{aligned} p = &\mu_0 + \underbrace{\alpha(0)E_0 cos(\omega t)}_{\text{Rayleigh}} + \underbrace{\sum_{i=1}^{Q}\left(\frac{\partial \mu}{\partial q_n}\right) q_{n0} cos(\omega_n t)}_{\text{IR}} \\ &+ \underbrace{\frac{1}{2}E_0 \sum_{i=1}^{Q}\left(\frac{\partial \alpha}{\partial q_n}\right) q_{n0}[cos(\omega + \omega_n)t) + cos(\omega - \omega_n)t)]}_{\text{Raman scattering}} \end{aligned} \tag{2.9}$$

Rayleigh together with infrared, Stokes and anti-Stokes Raman scattering, respectively, are represented on eq. (2.9). If the change of polarizability from the incoming electric field excitation equals zero ($\frac{\partial \alpha}{\partial q}|_{q=0} = 0$), the molecular vibration is not Raman active and no Raman

band appears in the spectrum. From eq. (2.9) we also can see that during Raman spectroscopy we measure the energy shift of scattered light compare to the excitation wavelength (that is called as Raman shift). The Raman shift of a particular vibration yields directly the energy of this vibration. This value is independent of the excitation wavelength and is most commonly reported in wavenumbers, units of inverse length. To convert spectral wavelength to Raman shift the following formula can be applied:

$$\Delta\omega(\mathrm{cm}^{-1}) = \left(\frac{1}{\lambda_0(\mathrm{nm})} - \frac{1}{\lambda_1(\mathrm{nm})}\right) \times \frac{10^7 \mathrm{nm}}{\mathrm{cm}} \tag{2.10}$$

Where $\Delta\omega$ is the Raman shift, and λ_0 and λ_1 are respectively wavelength of laser excitation and observed Raman band. Conversion to cm^{-1} is used to have more suitable values of Raman shift (hundreds and thousands).

3 Materials

3.1 Description of virgin crystals

Figure 3.1: Photo of different lanthanide phosphates. Flat elongated crystals belong to the tetragonal group ($ErPO_4$ (pink), $HoPO_4$ (dark red), YPO_4 (yellow)) and asymmetric round-shaped crystals belong to the monoclinic group ($LaPO_4$ (white), $CePO_4$ (black), $SmPO_4$ (yellow), $PrPO_4$ (green)).

Phosphates of rare earth elements draw ongoing attention as possible materials for nuclear waste storage. Phosphates are found in nature as monazite ([Ce,La]PO_4) and xenotime ([Y,Er]PO_4) minerals. Monazite has a monoclinic crystal structure and xenotime crystallizes into a tetragonal structure. Natural monazite together with zircon (zircon silicate, $ZnSiO_4$ that is isomorphous with the xenotime) were intensively studied as potential waste forms [11, 13, 45–47].

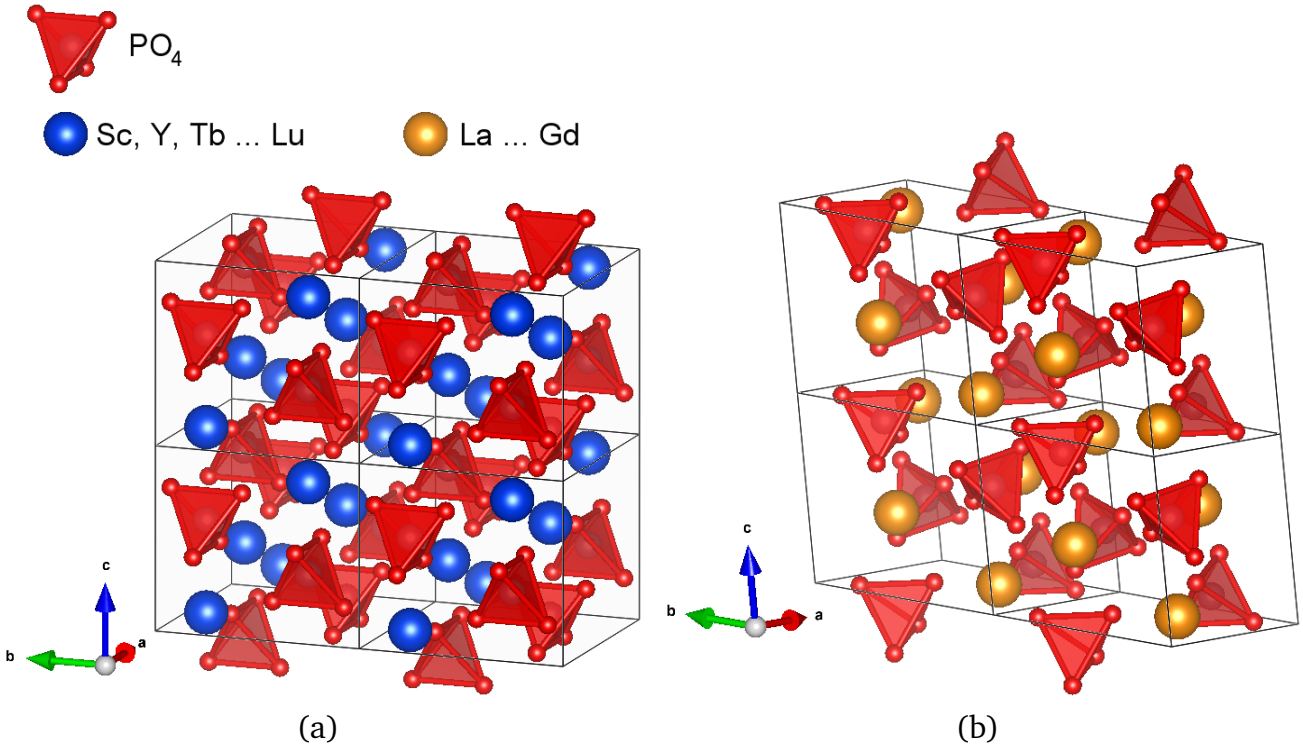

Figure 3.2: Crystal structures of two groups of $LnPO_4$ (made using Vesta software [48] and data from [49]): a) tetragonal $HoPO_4$ (space group $I4_1/amd$); b) monoclinic $NdPO_4$ (space group $P2_1/n$).

For the purpose of better understanding of physical processes that lie behind radiation hardness it is important to study single-element lanthanide phosphates. Single crystals of rare earth phosphates were produced by the lead flux method described in [50–52] at the Oak Ridge National Laboratory. Phosphates of the first subgroup (La to Gd) crystallize into the monoclinic monazite structure, whereas phosphates of the second subgroup (Tb to Lu and Y, Sc) form the tetragonal xenotime structure [50]. A detailed X-Ray study of all lanthanide phosphates was performed by Ni et al. providing crystal data together with structure refinements [49].

Both crystal structures are closely related: monazite ($P2_1/n$) as well as xenotime ($I4_1/amd$) contain isolated PO_4 tetrahedra together with LnO_x polyhedra (fig. 3.2). The monazite structure could be formed from the tetragonal structure by a slight rotation of the PO_4 tetrahedra, thus reducing the symmetry from tetragonal to monoclinic. Within the series of lanthanide elements, the atomic radius decreases with increasing atomic number, known as lanthanide contraction. Elements of the second part of the lanthanide series having smaller ionic radii can be easily incorporated into the symmetric tetragonal crystal structure whereas the increase of the ionic

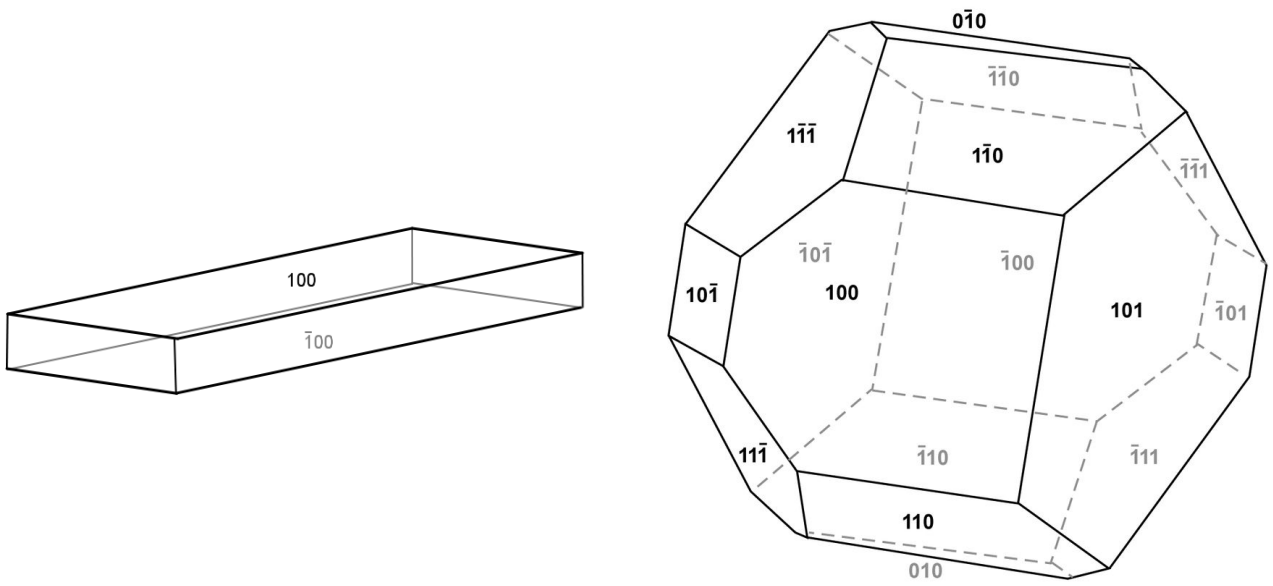

(a) (b)

Figure 3.3: Schematic of macroscopic $LnPO_4$ crystals; plane [100] was irradiated in case of tetragonal crystals and [$\bar{1}$01] for monoclinic structure; a) tetragonal $LnPO_4$; b) monoclinic $LnPO_4$ [53]. ©(2017) reprinted with permission from Mineralogical Society of America.

radius starting from Gd and up to La, requires PO_4 tetrahedra rearrangement [49]. As result of such a rearrangement in the monoclinic monazite structure, lanthanide ions form polyhedrons with oxygen LnO_9 and LnO_8 polyhedrons for the tetragonal xenotime structure.

The difference in lattice symmetry is directly reflected in the macroscopic shape of the $LnPO_4$ crystals (fig. 3.1). In the case of the tetragonal xenotime structure ($I4_1/amd$), macroscopic crystals have a shape of flat elongated bars. Length and width of the crystals are 5-15 mm and 1-3 mm, respectively. A typical thickness of the investigated tetragonal-shaped crystals is around 0.2 to 0.5 mm (figs. 3.1 and 3.3(a)). Crystals with a monazite structure are usually more bulky and round (figs. 3.1 and 3.3(b)). Typical thickness of monoclinic crystals is 3-5 mm, while length and width are in the order of 3-8 mm each. Samples that belong to both crystal structures usually have a dominant plane. Single crystal XRD measurements showed that the dominant plane of tetragonal crystals is [100] and for monoclinic phosphates it is the [$\bar{1}$01] orientation.

The different crystal structure of the two groups affects their mechanical properties. The surfaces of the crystals had defects that were created during sample production (fig. 3.4). Virgin samples belonging to the monazite subgroup possess high mechanical stability without showing initial cracks (sometimes surface scratches). When trying to cleave them, the crystals fragmented into numerous small chunks. In contrast, virgin samples of tetragonal xenotime structure were extremely brittle, had lots of cracks in the virgin state and could easily be cleaved/cracked into several larger pieces. Optical images on fig. 3.5 clearly show this differ-

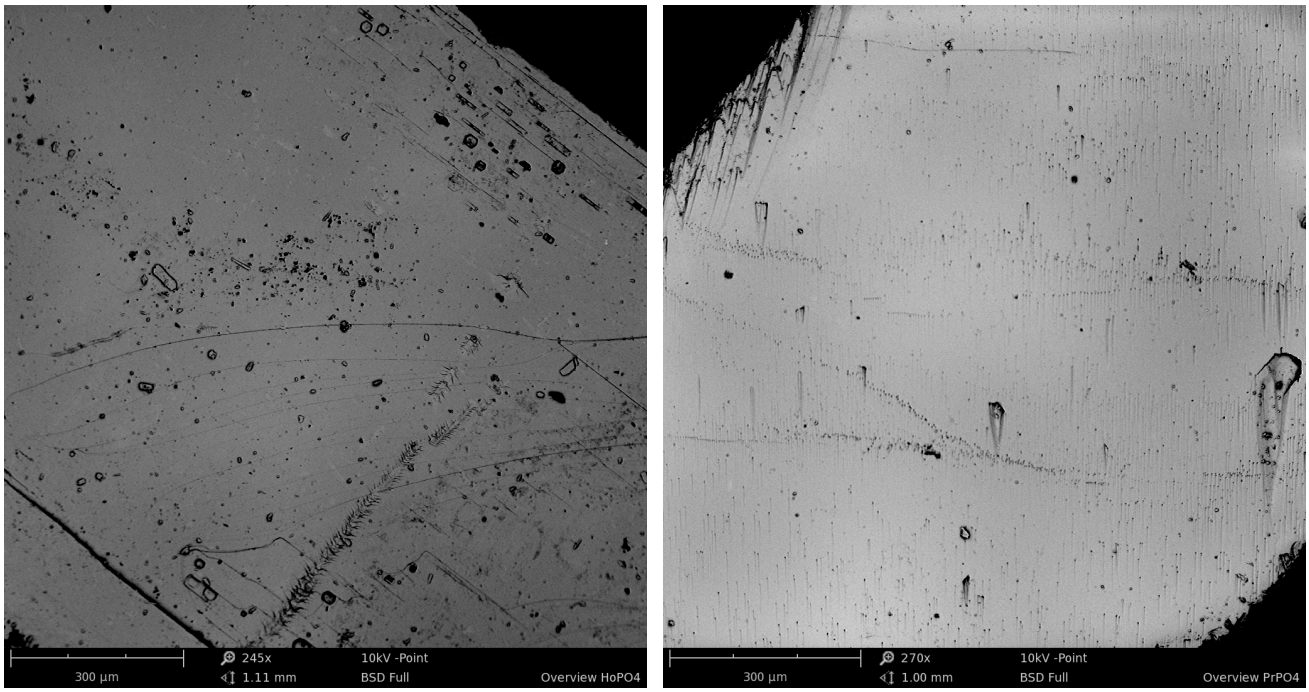

(a) (b)

Figure 3.4: SEM images showing the surface of virgin single crystals of a) tetragonal holmium phosphate ($HoPO_4$) and b) monoclinic praseodymium phosphate ($PrPO_4$).

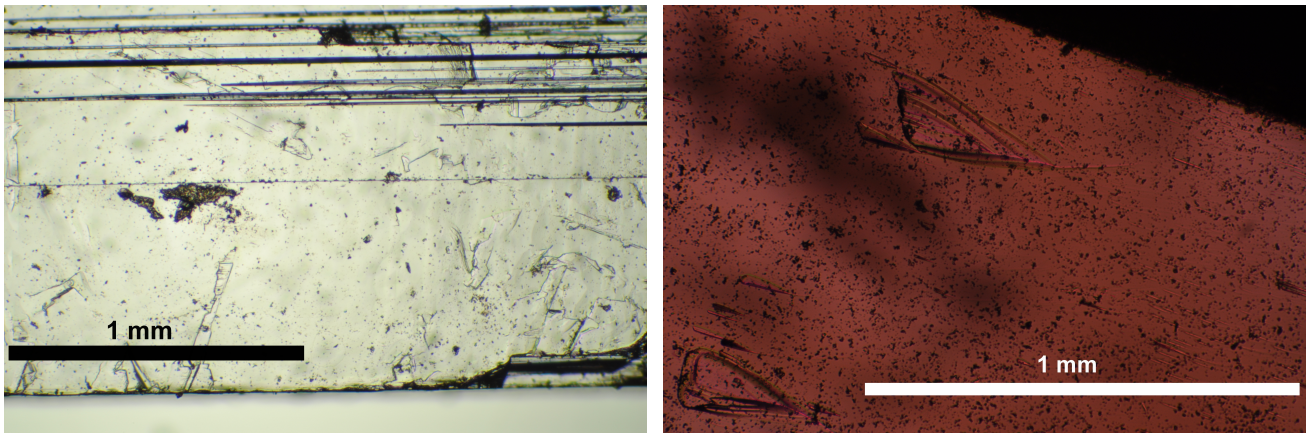

(a) (b)

Figure 3.5: Optical images of virgin single crystals of a) tetragonal thulium phosphate ($TmPO_4$) and b) monoclinic neodymium phosphate ($NdPO_4$).

ence. Differences in mechanical properties will turn out to be important with respect to the sample response to irradiation, in particular regarding cracking due to accumulation of internal radiation-induced mechanical stresses. The main method used in this work for quantification of radiation damage in single crystals of rare earth phosphates is Raman spectroscopy. Raman spectra of virgin crystals of $LnPO_4$ have previously been reported in literature, first by Begun et al. [54] and more recently, by Silva et al. [55] analysing the monazite structure in detail. Factor group analysis suggested 12 Raman active vibrational modes for tetragonal $LnPO_4$. For

the monoclinic structure, the number of modes is higher due to reduced symmetry: 36 modes according to both Poloznikova [56] and Begun et al. [54] and 18 A_g/B_g vibrations as suggested by Silva et al. [55].

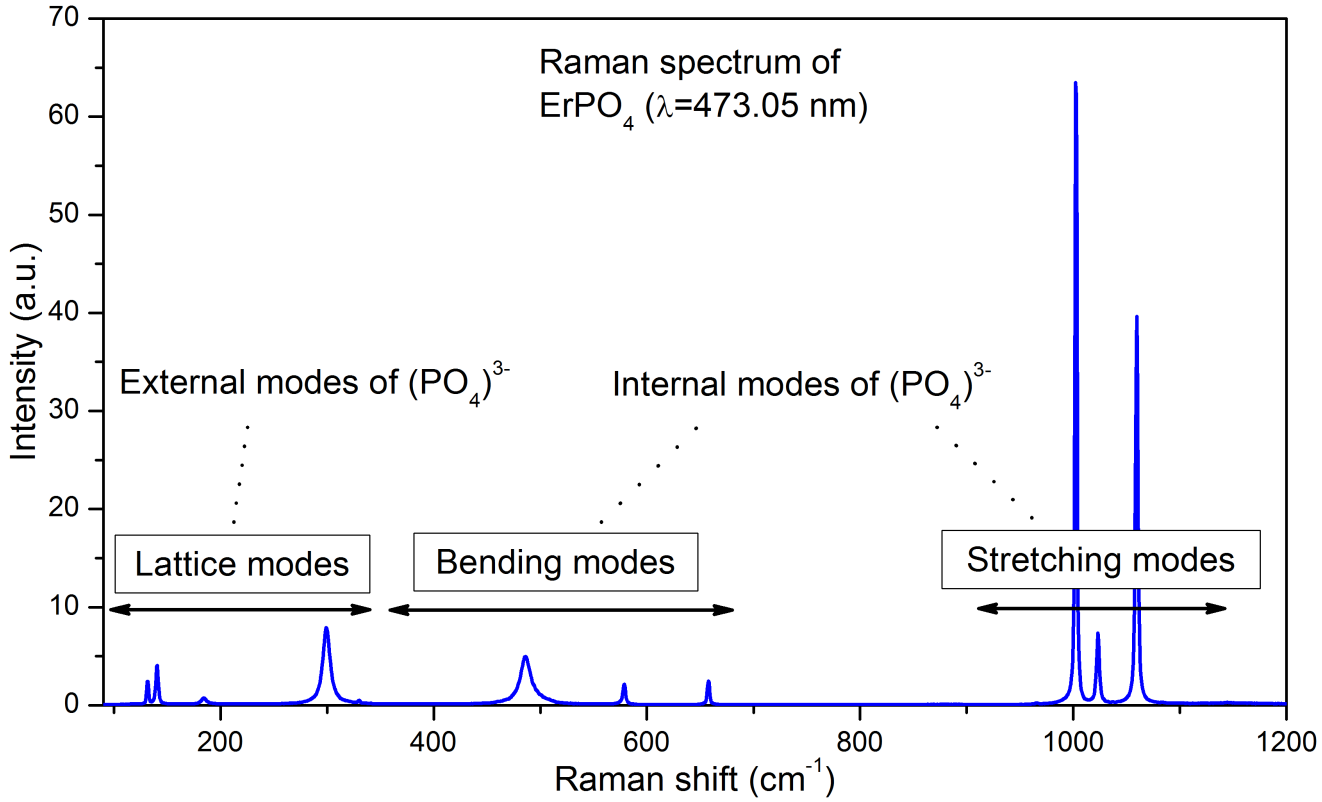

Figure 3.6: Different Raman modes in the spectrum of $ErPO_4$ measured using blue laser (λ = 473.05 nm).

The structure of lanthanide phosphates can be approximated quite well by two sub-lattices, one of them containing only rare earth elements (REE^{+3}) and the other one having $(PO_4)^{3-}$ units. Modes with Raman shifts above 350 cm^{-1} are the so-called internal modes of PO_4 structural element. Raman peaks in this region are formed by different vibrations of the P-O bond. The region below 350 cm^{-1} contains external modes (in relation to the PO_4 structural unit).

For both phosphate structures, the Raman spectra can be grouped into the following three regions (see also fig. 3.6):

- Stretching modes, in spectral range between 950 and 1150 cm^{-1} containing symmetric and asymmetric stretching modes of the $(PO_4)^{3-}$ tetrahedron.
- Bending modes, in spectral range between 350 and 700 cm^{-1} containing different bending modes of the $(PO_4)^{3-}$ tetrahedron.
- Lattice vibrations below 350 cm^{-1}.

Within the series of lanthanide phosphates Begun et al. [54] reported a systematic Raman frequency shift to higher wavenumbers with increasing of atomic number and decreasing crys-

tal radii (REE^{+3} (pm)). For both tetragonal and monoclinic crystal structures, this trend was demonstrated for stretching and bending modes. Yttrium orthophosphate (YPO_4) does not follow peak shift versus atomic number, however matches the dependence perfectly when crystal radii are considered. The authors concluded that the decrease of the crystal radii within the lanthanide series results in a closer packing of the $(PO_4)^{3-}$ ion groups and shortening of the P-O distance. The reduced distance between phosphor and oxygen ions in the phosphate tetrahedron increases the bonding energy and reflects in the shifts the Raman band towards the higher values. For the lattice vibrations trend found to be not so strong and generally more complicated. Assignments were provided for all the lattice vibrations following Boatner et al. [54] and Poloznikova [56]. However in the case of the monazite crystal structure, not all vibrations are identified unequivocally. More recently Silva et al. [55] have broadened the understanding of Raman spectra of monazite type lanthanide phosphates. Compared to Raman bands suggested by factor group analysis, they have shown that peaks in Raman spectra above 450 cm^{-1} in monazite type $LnPO_4$ could result from defects inducing a lowering of the local symmetry. In the regions of lattice modes, they observed that modes in the region of 120-140 cm^{-1} do not follow well the polarization rules, that excludes the interpretation of these bands as fundamental [55].

Another important feature of Raman spectroscopy measurements in lanthanide phosphates is luminescence. Laser light can excite electron transitions between the energy levels in lanthanide ions and induce strong luminescent contributions to the Raman spectra. Luminescence may serve as a perfect spectroscopic “fingerprint” of a particular compound. However, luminescence can also be very problematic due to addition of a huge background to the Raman spectra. Luminescent contributions strongly depend on the energy of excitation and can be avoided by changing the laser excitation wavelength. Figures 3.7 to 3.10 provide the Raman spectra of all pristine $LnPO_4$ compounds measured using 473.05 nm and 632.82 nm laser excitation wavelengths. All spectra are provided in original intensity (figs. 3.7(a), 3.8(a), 3.9(a) and 3.10(a)) and scaled (figs. 3.7(b), 3.8(b), 3.9(b) and 3.10(b)) to better identify less intense Raman bands. Different lasers were used, while all the other settings were kept the same; measurement time was 20 sec for most of the measurements (exceptions are listed below).

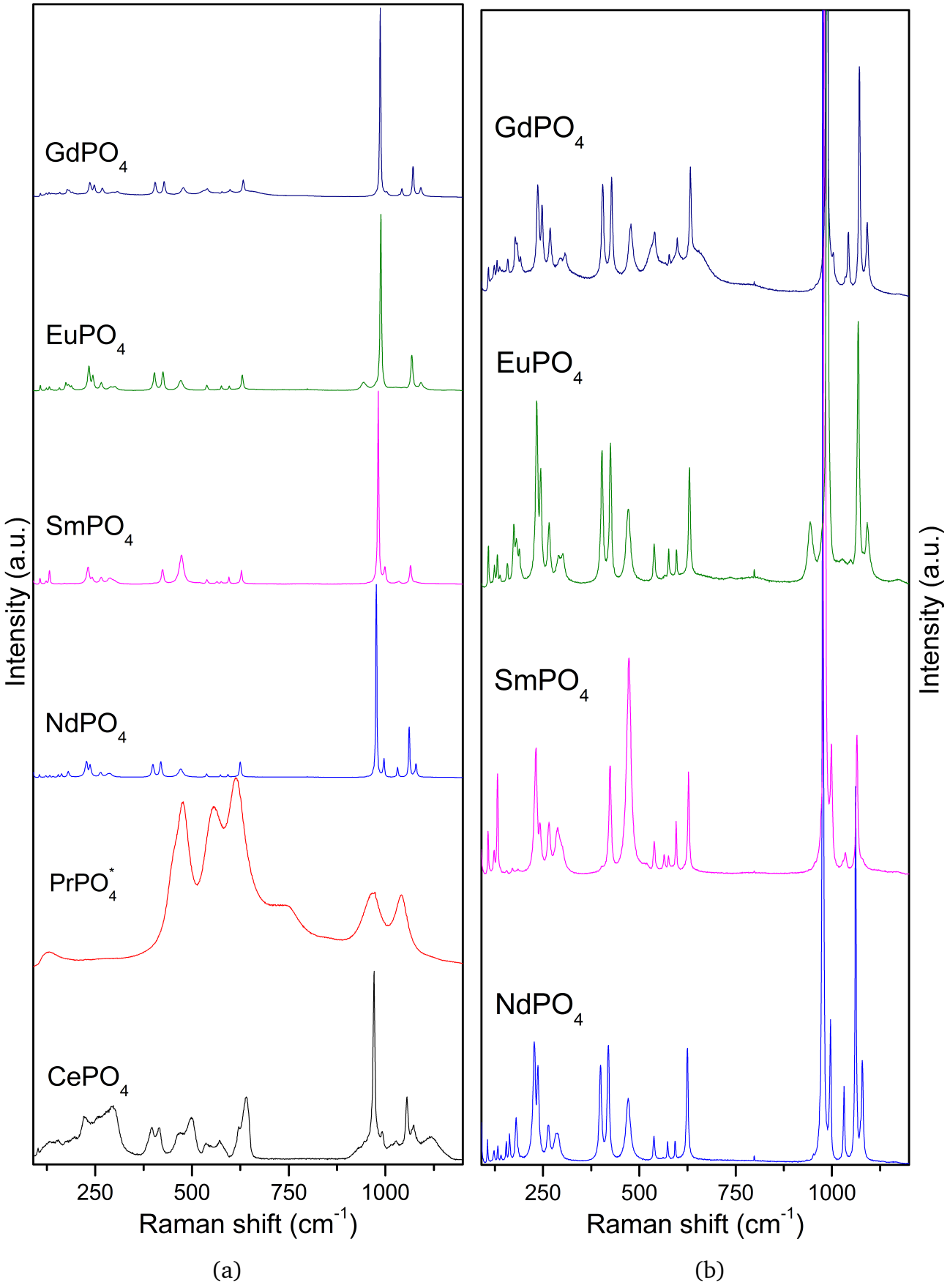

Figure 3.7: Raman spectra of pristine monazite-type (monoclinic) $LnPO_4$ obtained with 473.05 nm laser wavelength excitation: a) Full intensity; b) Enlarged for small peaks. *Spectrum of $PrPO_4$ contains only fluorescent contribution.

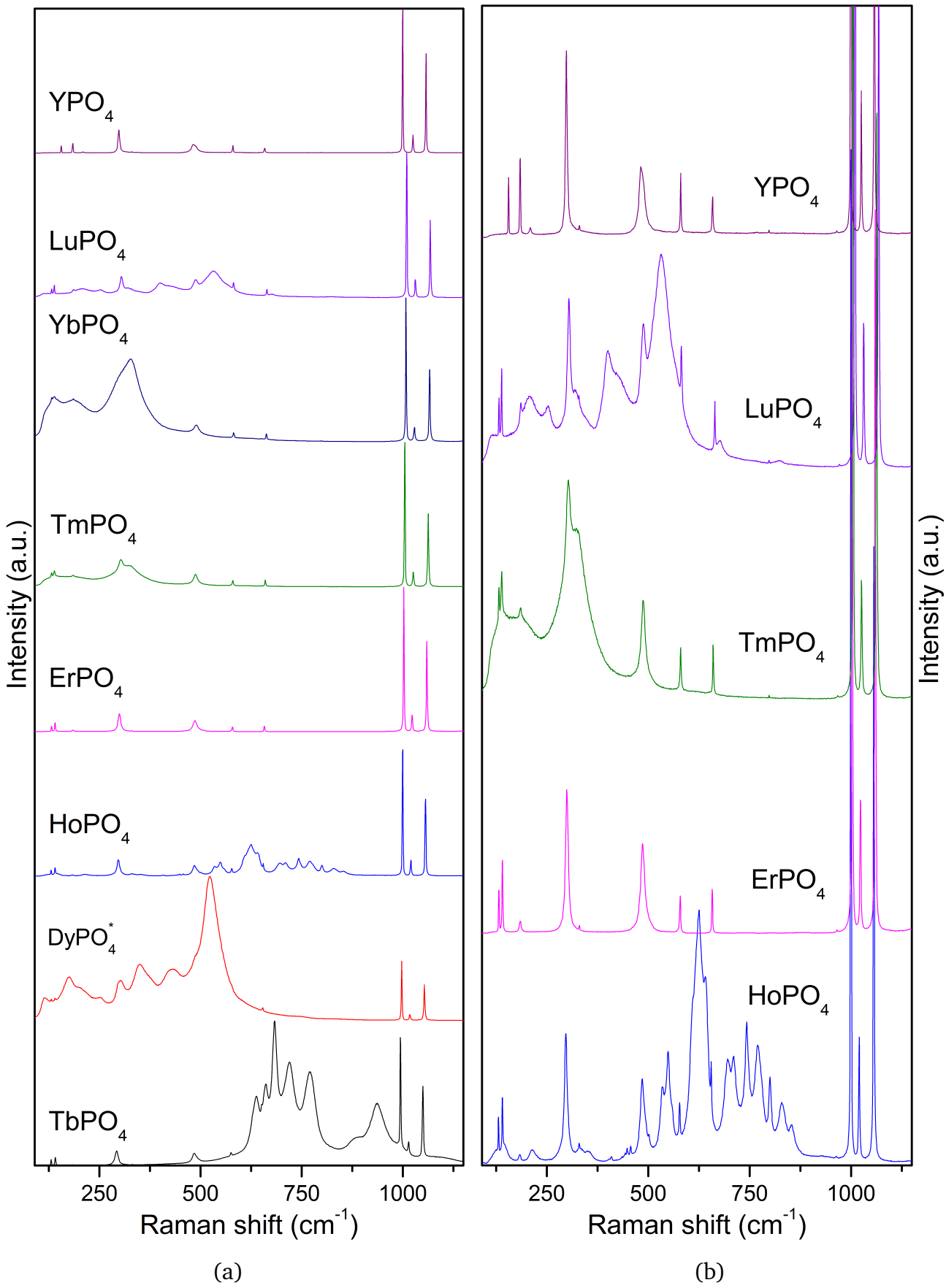

Figure 3.8: Raman spectra of pristine zircon-type (tetragonal) $LnPO_4$ obtained with 473.05 nm laser wavelength excitation: a) Full intensity; b) Enlarged for small peaks. *Spectrum of $DyPO_4$ contains significant luminescent contribution; the measurement time was 1/3 compare to the rest of compounds.

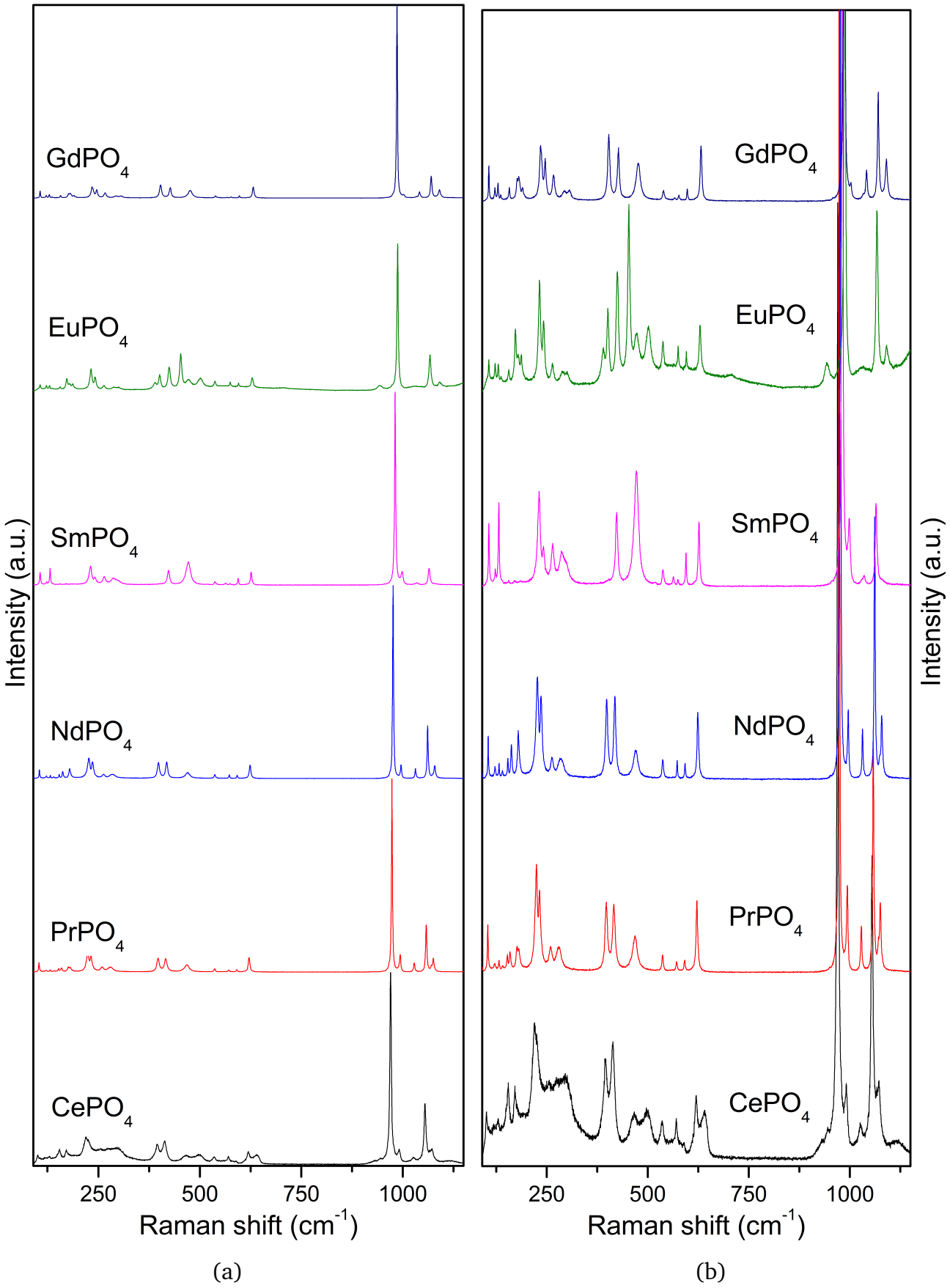

Figure 3.9: Raman spectra of pristine monazite-type (monoclinic) $LnPO_4$ obtained with 632.82 nm laser wavelength excitation: a) Full intensity; b) Enlarged for small peaks.

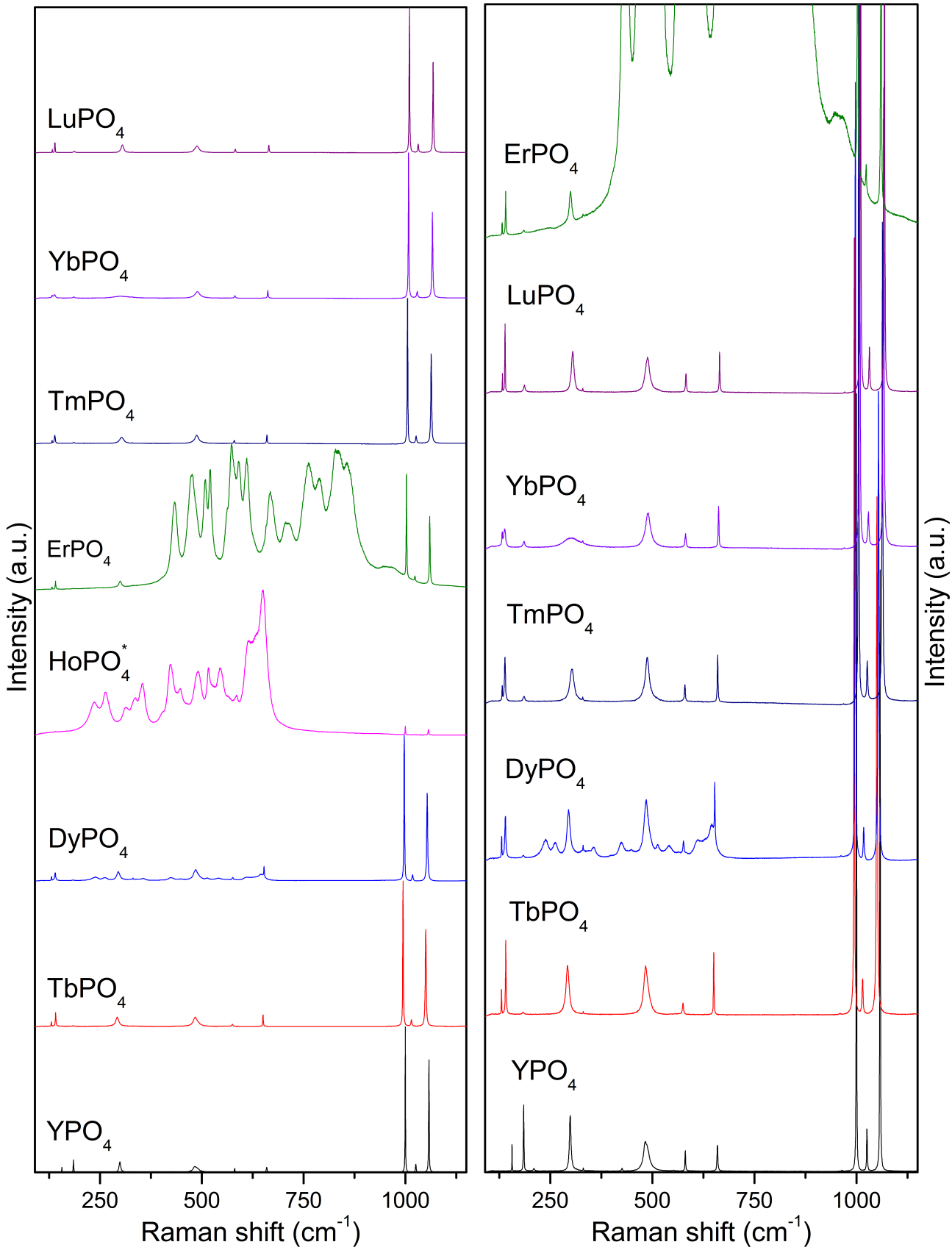

Figure 3.10: Raman spectra of pristine zircon-type (tetragonal) $LnPO_4$ obtained with 632.82 nm laser wavelength excitation: a) Full intensity; b) Enlarged for small peaks. *Raman spectrum of $HoPO_4$ contains tiny traces of Raman signal and strongly overwhelmed by fluorescence.

In the following few cases, the luminescence was too strong to provide measurement of the Raman bands simply because the detector saturated within a fraction of a second:

- praseodymium phosphate ($PrPO_4$) fig. 3.7 measured using $\lambda = 473.05$ nm and measurement time of 0.5 sec - no Raman peak could be observed,
- dysprosium phosphate ($DyPO_4$) fig. 3.8 measured using $\lambda = 473.05$ nm and measurement time of 7 sec: the only peaks in the region of stretching modes could be distinguished,
- holmium phosphate ($HoPO_4$) fig. 3.9 measured using $\lambda = 632.82$ nm and measurement time of 2 sec - no significant Raman peak could be observed (small signal of symmetric and antisymmetric stretching modes could be allocated around 1000 cm^{-1}).

Apart from dominant luminescence effects listed above, luminescence can also be present as less intense contribution to the Raman spectrum

- either in the form of an overall broad background ($EuPO_4$ and $CePO_4$ (both on fig. 3.10(b)), $GdPO_4$ (fig. 3.7(b)));
- or having band-like structure of single or series of relatively sharp peaks as for $HoPO_4$, $TmPO_4$ and $LuPO_4$ (fig. 3.8(b)), $DyPO_4$ (fig. 3.10(b)).

3.2 Response of $LnPO_4$ to the irradiation

Irradiated phosphates of rare earth elements in their natural forms of monoclinic- (monazite) and tetragonal-structured (xenotime) minerals are repeatedly reported in literature. Both being abundant minerals that incorporate naturally occurring actinides, they provide extensive mineralogical evidence for the material response to the self-irradiation and long-term effects of radioactive decay. In nature both minerals were rarely found in metamict state. This can be explained by the low activation energy for the damage recovery process and low temperatures of recrystallization [7]. Vance and Pillay [57] performed systematic study of phosphates (both monazite and xenotime) doped with depleted or enriched uranium to study the structural effects of fission-fragment irradiations. Both minerals are reported to completely amorphize due to fission fragment irradiations. However, a discrepancy of material sensitivity to the irradiation by fission fragments and α-particles was noticed. Annealing of completely amorphous xenotime and monazite phosphates was observed at temperatures as low as 200-300°C.

Several investigations of radiation damage in synthetic lanthanide orthophosphates are reported in literature. Meldrum et al. [15] performed irradiations of both monazite and zircon-type orthophosphates with 800 keV Kr^{2+} ions. Analysis of radiation damage using in situ electron microscopy was performed for different doses at temperatures varying from 20 to 600 K. Material amorphization was observed by the loss of electron-diffraction maxima. Within an experimental uncertainties the authors could not distinguish the critical amorphization dose for different materials at the room temperature. Comparison of irradiations at elevated temperatures showed that tetragonal phosphates can be amorphized at higher temperatures than the monoclinic ones. Thus, the critical amorphization temperature (T_c) for monazite-type phosphates is lower than that of the zircon-type group. Within the group, T_c increases with increase of atomic number. The authors were also trying to take into account combined effects of nuclear $(dE/dx)_n$ and electronic $(dE/dx)_e$ energy losses, because in some materials the resulting damage can be influenced by the ionizing radiation i.e. by triggering the defect recombination [15]. Introducing the ratio of electronic-to-nuclear stropping power (ENSP), a decrease of T_c with increasing of ENSP was shown for both structures. Moreover, tetragonal phosphates have a higher T_c than the monoclinic ones for the same ENSP. Meldrum et al. [12] studied $LaPO_4$ and $ScPO_4$ irradiated by 1.5 MeV Kr^+ ions using the technique described above. In addition to ion beam induced amorphization, recrystallization was observed under electron irradiation [12]. Together with natural monazite and zircon, La and Sc phosphates as respective representative of the monazite and zircon-type group were compared. Both $LaPO_4$ and $ScPO_4$ could be recrystallized by the electron beam with the monazite-structure phosphate being more easily recrystallized. Authors have linked this effect to the displacement cascades being smaller in the monoclinic structure than in tetragonal phosphate due to lower channeling and absence of linear collision sequences. A comparison of irradiations by 1.5 MeV and 800 keV Kr ions

showed that a decrease of the impacting ion energy is accompanied by an increase of the critical amorphization dose and a decrease of both critical temperature (T_c) and activation energy for irradiation-induced annealing (E_a). Analysis of natural monazite and zircon brought the conclusion that chemical impurities increase the barrier for recrystallization.

More recently Picot et al. [58] studied $LaPO_4$ and $La_{0.73}Ce_{0.27}PO_4$ monazite compounds after irradiation by Au (1, 3.5 and 7 MeV) and He (1.7 MeV) ions. According to Nasdala et al. [59] Picot's Raman measurements were unfortunately performed incorrectly (see discussions in section 4.2, fig. 4.6) and thus conclusions related to Raman spectroscopy measurements are invalid. However, several more measurements performed on irradiated monazite materials revealed $LaPO_4$ matrix swelling of about 0.8% for irradiation fluences higher than 10^{14} at./cm^2 (units are kept according to the reference). Also, the hardness reduced by about 59% compared to the initial value for $LaPO_4$ irradiated with Au ions up to 2.3×10^{15} at./cm^2. Nasdala et al. [59] performed Raman spectroscopy investigations of radiation damage in $CePO_4$ irradiated with 1, 3.5 and 7 MeV Au ions. They have found significant broadening of the symmetric stretching mode of the PO_4 tetrahedron that increases of ion fluence and is accompanied by a gradual shift towards lower wavenumbers. At the highest irradiation fluence of 5.1×10^{14} ions/cm^2, the remain Raman signal of crystalline $CePO_4$ disappeared and the only feature was a broad "amorphous" hump around 960 cm^{-1}.

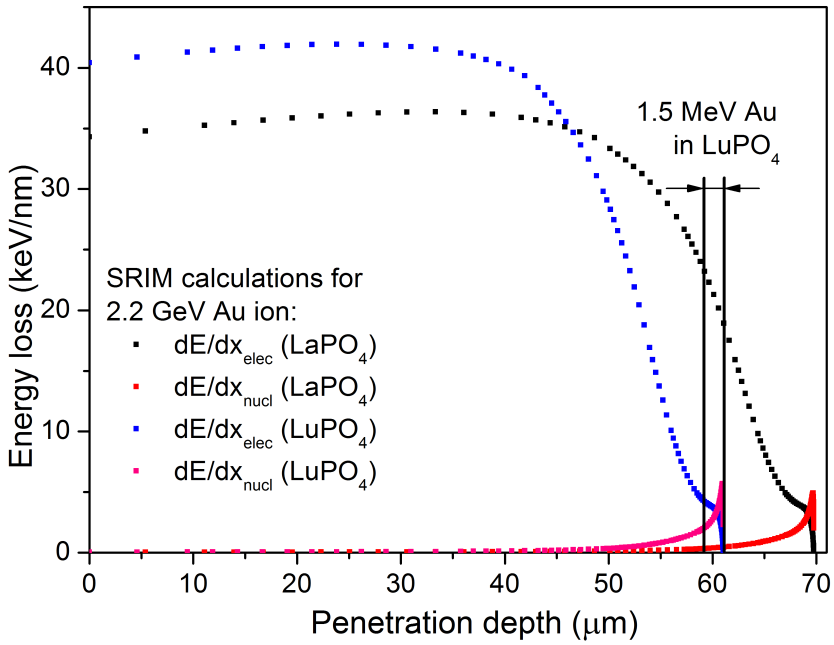

Figure 3.11: Electronic and nuclear energy loss for $LaPO_4$ and $LuPO_4$ irradiated by 2.2 GeV ^{197}Au ions. The calculations were performed with the SRIM-2010 code. According to table 3.1, $LaPO_4$ have the lowest and $LuPO_4$ have the highest density of the lanthanide phosphate series.

Table 3.1: $LnPO_4$ densities (based on single-crystal XRD measurements).

Phosphate	Density (g/cm^3)
$LaPO_4$	5.08
$CePO_4$	5.20
$PrPO_4$	5.35
$NdPO_4$	5.45
$SmPO_4$	5.73
$EuPO_4$	5.80
$GdPO_4$	6.00
$TbPO_4$	5.79
$DyPO_4$	5.94
$HoPO_4$	6.06
$ErPO_4$	6.19
$TmPO_4$	6.28
$YbPO_4$	6.44
$LuPO_4$	6.55
YPO_4	4.26
$ScPO_4$	3.70

In several other studies [12, 15, 58, 59] irradiations were performed with ion energies ranging from 800 keV to several MeV. In this regime, the energy transfer from the impacting ion to the material is a combination of the electronic $(dE/dx)_e$ and nuclear $(dE/dx)_n$ energy loss. On fig. 3.11 we can see, that for the 1.5 MeV Au ion implanted in $LuPO_4$, the penetration depth is around 2.2 μm. The last micrometer of the ion path is dominated by nuclear stopping, whereas during the first micrometer the ratio of electronic to nuclear energy loss is roughly 50/50. The material response to irradiation by ions in the mixed nuclear and electronic stopping regime is not straight-forward.

In contrast, irradiations with swift heavy ions are dominated by electronic stopping (fig. 3.11). In this care we can analyze radiation effects purely based on the electronic energy loss. According to eqs. (2.2) and (2.4) the electronic energy loss depends on material density, velocity and charge of an impacting ion. Calculations for $LaPO_4$ and $LuPO_4$ irradiated by 2.2 GeV Au ions using the SRIM-2010 code and material densities tables (table 3.1) are present on fig. 3.11.

4 Experimental

4.1 Irradiations

Irradiations with swift heavy ions were performed at the accelerator facility of GSI Helmholtz Center for Heavy Ion Research [60] consisting of two units: the UNIversal Linear ACcelerator (UNILAC) and the heavy ion synchrotron (SIS18). The UNILAC provides ions with energies up to 11.4 MeV/u, whereas subsequent acceleration using the synchrotron allows ion energies up to 1000 MeV/u. Ions that can be accelerated range from proton ($^{1}H^{+}$) to uranium ($^{238}U^{29+}$). The operation modes of different ion sources (see [61]) provide different beam conditions including high pulse length (5 ms and repetition rate of 50 Hz) or low duty cycle (pulse length of 0.2 ms and repetition rate of 2 Hz). Several experimental beamlines are situated at the end of the UNILAC accelerator, among them the X0-beamline and the M-Branch provide experimental stations dedicated for material science irradiation experiments.

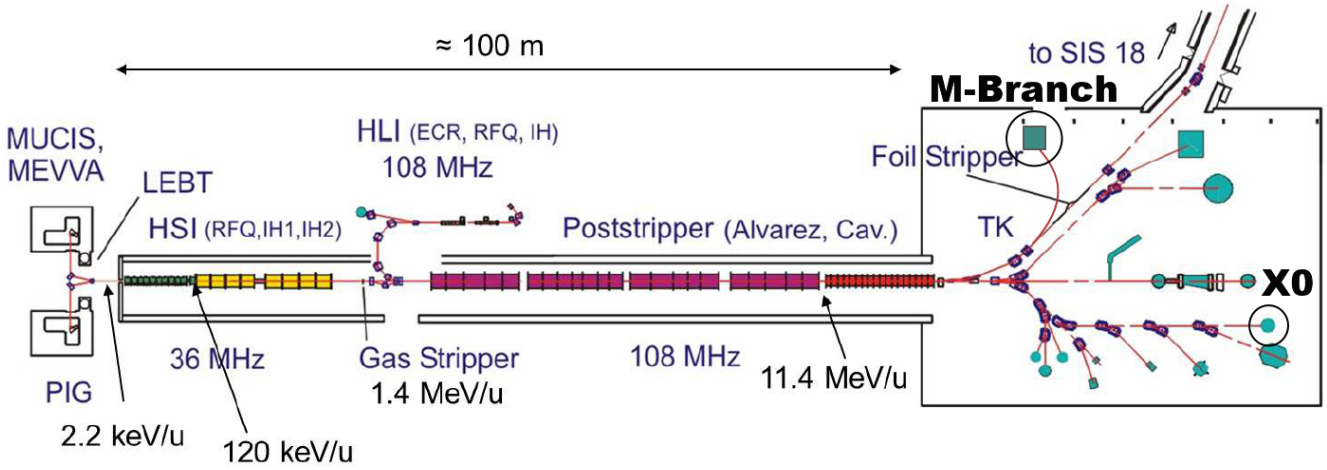

Figure 4.1: Scheme of UNILAC section of GSI accelerator facility (adopted from [62]); M-Branch and cave X0 for material science experiments are indicated.

At both beamlines irradiations were performed at the room temperature and in vacuum. The beam incidence is perpendicular to the sample surface. Crystals of different $LnPO_4$ samples were mounted on aluminum plates (1×1 cm^2) using a graphite tape (fig. 4.2). In some cases the sample was covered by an 10-μm thick aluminum foil to prevent sample detachment and falling of sample fragments into the irradiation chamber. This 1 cm^2 package was placed on a holder beside other samples that require same irradiation conditions.

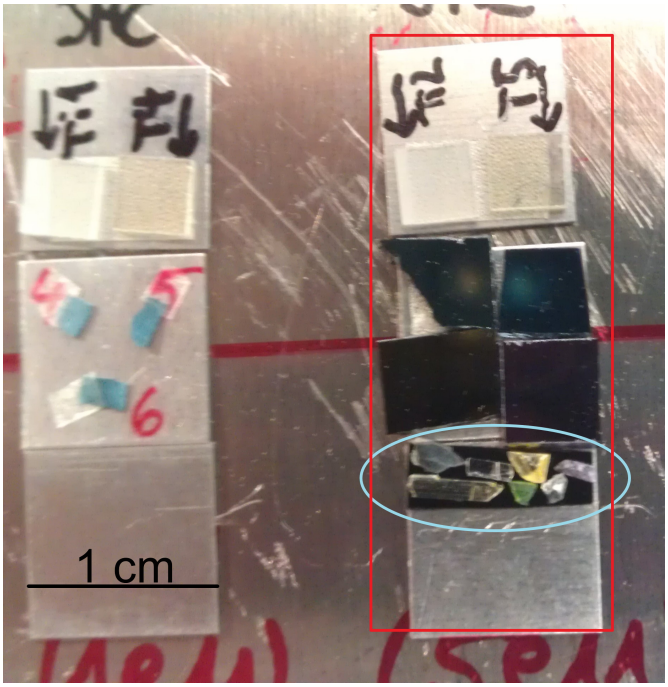

Figure 4.2: Photo of sample mounting at the M3 beamline of the M-Branch of the UNILAC.

At the **X0 beamline** samples are mounted onto 5×5 cm^2 aluminum holder. With the help of quadrupole magnets the beam is adjusted defocused such that the entire area is exposed homogeneously to the ion beam. Monitoring of ion fluence and flux was done with the help of a secondary electron transmission monitor (SETRAM) consisting of three 1 μm thick aluminum foils with applied voltage. When passing through these foils, charged ions produce electrons that are converted to an electrical current. Before sample irradiation the SETRAM is calibrated using ion current recorded in a Faraday cup. The flux was kept in between 1×10^8 and 5×10^8 ions/cm^2·s and fluences were up to 1×10^{13} ions/cm^2). Before impacting the sample, incoming ions passed through the SETRAM reducing their energies from 11.4 to 11.1 MeV/u and providing equilibrium charge state.

The beamlines at the **M-Branch** are used for the irradiation experiments combined with online experimental techniques such as Raman and IR spectroscopies, X-Ray diffraction, SEM, AFM etc. [63–66]. The samples are mounted on a aluminum plate that is fixed on a moving stage. The beam is defocused to homogeneously cover the sample area. Excessed beam is cut by four slits. The current that is generated by the ion beam on the slits is used for beam monitoring. Before each irradiation the slit current is calibrated by beam current measurement in a Faraday cup. Details about beam structure could be found in table 4.1.

Series of $LnPO_4$ samples were irradiated under various beam conditions at both X0 and M3 beamlines. The list of samples together with irradiation parameters are presented in Table 4.1. Additional ion energy reduction occurs due to sample being covered by aluminum foil. Since beam parameters (frequency and pulse length) play significant role in materials response to the irradiation they are always stated in the sample description.

Table 4.1: List of irradiated samples and irradiation conditions. "Energy" denotes ion energy at the sample surface.

Sample ([X]PO_4)	Ion	Energy (MeV/n)	Fluence (ions/cm^2)	Flux (ions/cm^2·s)	Beam parameters
[Y,Tm,Ho,Lu]	Au	11.1	5×10^{12}, 10^{13}, 5×10^{13}	10^9	50 Hz, 5 ms, M3
[Y,Tm,Ho,Lu]	Au	11.1	5×10^{11}, 10^{12}, 5×10^{12}	10^8	50 Hz, 5 ms, M3
[Pr,Nd,Sm,Eu]	Au	11.1	5×10^{11}, 10^{12}, 5×10^{12}, 10^{13}	3×10^8	45 Hz, 5 ms, X0
[Y,Tm],[Pr,Sm]	Xe	11.4	10^{12}	1.8×10^8	2 Hz, 0.2 ms, M3
[Y,Tm],[Pr,Sm]	Xe	11.4	10^{12}	3.2×10^8	5 Hz, 1 ms, M3
All $LnPO_4$	Au	11.4	2×10^{12}	$>1.3\times10^8$	49 Hz, 5 ms, X0
[Y,Tm,Er]	Au	4.8	5×10^{12}	1×10^9	sweeping beam, M2

Swift heavy ion beam provided by the GSI accelerator facility has different pulse structures. Depending on the frequency and the pulse length, the ion beam used in the irradiation experiments could be divided into three categories:

- The low pulse intensity high repetition rate gold ion beam with a repetition rate equal to 50 Hz and with the pulse length of 5 ms. Such a beam provides the most homogeneous (over the time) irradiation. Within each second of irradiation time sample accumulates ion fluence within approximately 250 milliseconds.
- The low repetition rate low pulse intensity xenon ion beam with a repetition rate of 5 Hz and a pulse length of 1 ms. This beam has more intense pulses in order to provide the same ion flux (calculated as amount of ions per second) and requires providing of an increased amount of ions within a single pulse.
- The high pulse intensity low repetition rate xenon ion beam with the repetition rate of 2 Hz and pulse length of 0.2 ms. This beam has short intense pulses all the flux is compacted into the two short pulses within every single second of irradiation.

A schematic representation of all three beam types is shown on fig. 4.3. The evaluation of the amount of ions per single pulse could be easily done by taking into account a total flux and a repetition rate for the particular irradiation. All the necessary data is provided in table 4.1.

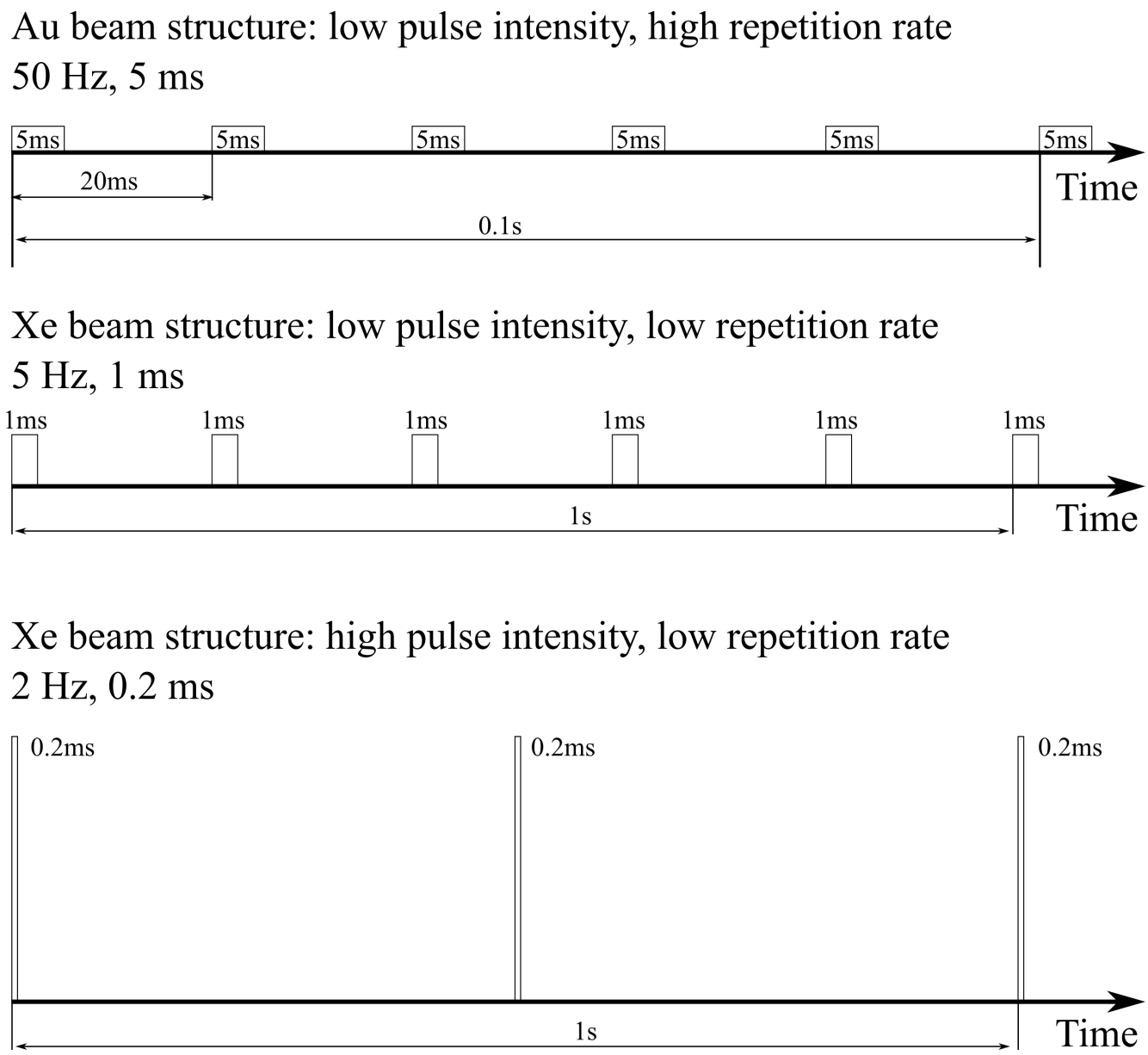

Figure 4.3: Different beam structures used in irradiations.

4.2 Raman spectroscopy measurements

Raman spectroscopy measurements were performed using a commercial Raman spectrometer from HORIBA Jobin Yvon (LabRAM HR800). The system has access to two lasers: He-Ne gas laser with the excitation wavelength of 632.82 nm and Cobalt solid state laser with the wavelength of 473.05 nm. Both lasers have less than 8 mW power measured on a sample surface what allows to avoid any possible sample heating or annealing by the laser beam.

The Raman system operates in backscattering (180°) geometry (see fig. 4.4). Edge filter is used in the system to cut out Rayleigh scattering. This allows measurements up to Raman shifts below 100 cm^{-1}. A confocal hole is installed in Raman system to provide good depth resolution and cut off the Raman signal too close or too far in z-direction from objective focusing point.

Set of objectives available for Raman measurement ranges from x5 magnification up to x100. A special long-working-distance x50LWD objective is used to measure samples where access to the sample surface is difficult or when the sample can only be measured inside of sample holder. The later problem was often the case for extremely brittle samples with high accumulated fluences. The theoretical laser beam spot on a surface is calculated using:

$$D = \frac{1.22\lambda}{NA}, \tag{4.1}$$

where D denotes spot diameter, λ is light wavelength and NA is numerical aperture of particular objective.

For 473.05 nm laser light that gives a spot size of 0.6 μm for the x100 objective (NA=0.9). In reality, the real laser spot size on a sample surface is larger due to slight system misalignment and nonideal focusing conditions. A grating with 1800 grooves/mm^2 was used at all measurements in this work. Peltier colling is used for the charge-coupled device (CCD) detector installed in Raman system providing detector operating temperature of -70°C. A silicon wafer was used as calibration standard.

Raman measurements of $LnPO_4$ single crystals were challenging due to appearance of large radiation-induced stresses. All irradiated samples contained cracks, many of them fragmented into smaller pieces. Cracked samples fragments allowed to measure Raman scattering perpendicular to the direction of the ion trajectories (fig. 4.5(a)). In the following, this measurement geometry will be referred as measurement *from the side* in contrast to the measurement *from the*

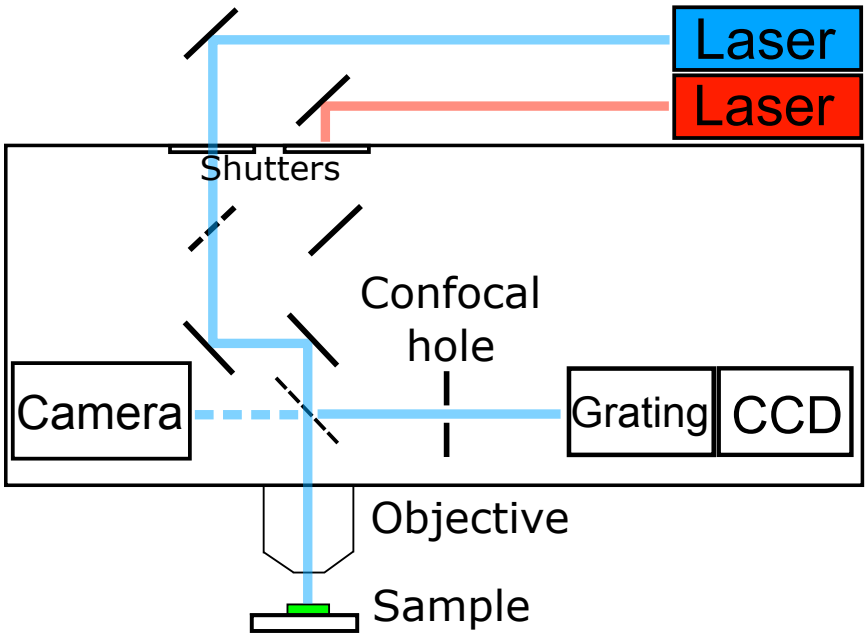

Figure 4.4: Schematic representation of Raman spectrometer. Two lasers are available: Cobalt solid state (λ=473.05 nm) and He-Ne gas (λ=632.82 nm) lasers. Measurements were performed in back-scattering geometry.

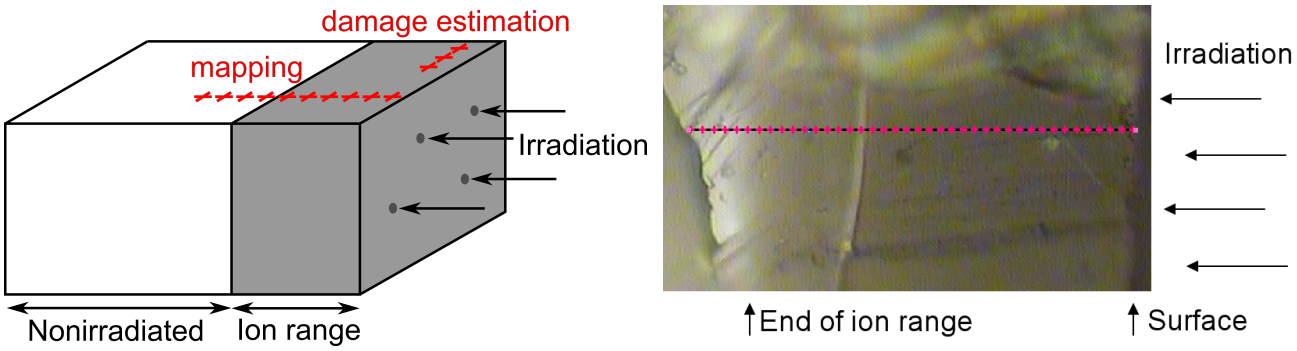

Figure 4.5: Raman spectroscopy measurement of $NdPO_4$ sample irradiated by Au ions up to 10^{13} ions/cm^2 (50 Hz, 5 ms); grey part indicates irradiated volume of material; end of ion range can easily be identified by the radiation induced change of sample color: a) schematic view; b) optical micrograph (x50 LWD objective); dotted line here is setting of line mapping to measure Raman spectra along the ion trajectory.

top, where the direction of laser light coincides with the direction of the ion irradiation. Due to the effect of different energy losses for the ions at a different penetration depth (fig. 3.11), it was important to develop consistency in Raman measurements for the series of samples. For systematic analysis Raman spectra were taken on a distance of 7 μm from sample surface. Closer to the sample surface a decrease of the Raman signal intensity was observed. Having the full Raman

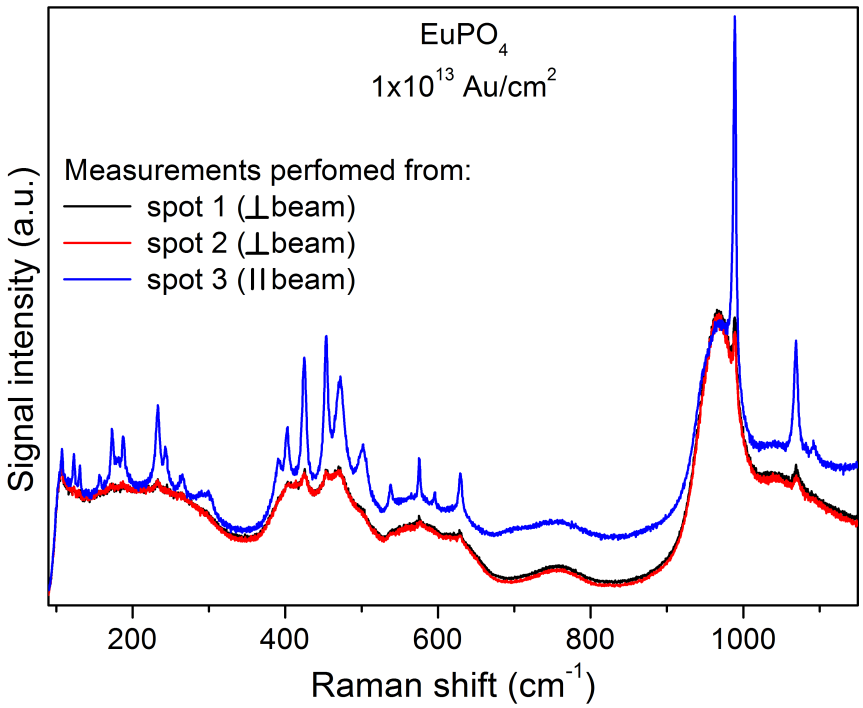

Figure 4.6: Raman spectra of $EuPO_4$ irradiated by 2.1 GeV Au ions at 10^{13} ions/cm^2 (50 Hz, 5 ms); Measurement of spot 1 and 2 were recorded from the sample edge perpendicular to the ion beam; data from spot 3 originates from the sample surface and combines Raman signal from the irradiated layer and a virgin sample beyond the ion penetration depth.

signal is crucial in particular for small samples and tiny fractured parts of the crystals. For the statistics Raman spectra were recorded from 10 different spots. This also provided information about homogeneity of the ion-beam-induced modification.

In order to test the effect of energy loss, Raman measurements were performed along the ion trajectory (fig. 4.5(a)). Linear mapping was used on a sample in the *side* orientation starting at the sample surface and exceeding into the nonirradiated crystal part beyond the ion penetration depth (fig. 4.5(b)). All the samples showed radiation-induced changes of color within the irradiated layer. This effect was helpful for a rough estimation of the mapping length.

It is important to mention, that it was not possible for any of the crystals to obtain Raman signal only from irradiated layer in the *from the top* geometry (fig. 4.6). Ion penetration depth for all the lanthanide phosphates ranges between 60 and 70 μm (fig. 3.11). With the adjustment of the confocal hole, the theoretical depth resolution should be way below the range value.

However even after setting of the smallest possible confocal hole size, the received signal was a mixture from irradiated and nonirradiated samples. Transparency of all $LnPO_4$ crystals combined with unusual optical properties [67] is possibly the reason for the effect.

4.3 Additional experimental techniques

4.3.1 In situ X-ray diffraction

On-line X-Ray diffraction experiments were performed at the M2 beamline. The system is equipped with a Seifert 4-circle X-Ray diffractometer and a Cu-K_α source (Cu-$K_{\alpha 1}$: $\lambda = 0.154056$ nm, Cu-$K_{\alpha 2}$: $\lambda = 0.15418$ nm) [68]. Samples are mounted normal to the direction of beam incidence. System is mounted inside of vacuum chamber. Both irradiations and X-Ray diffraction measurements are done under a vacuum of 10^{-10} bar.

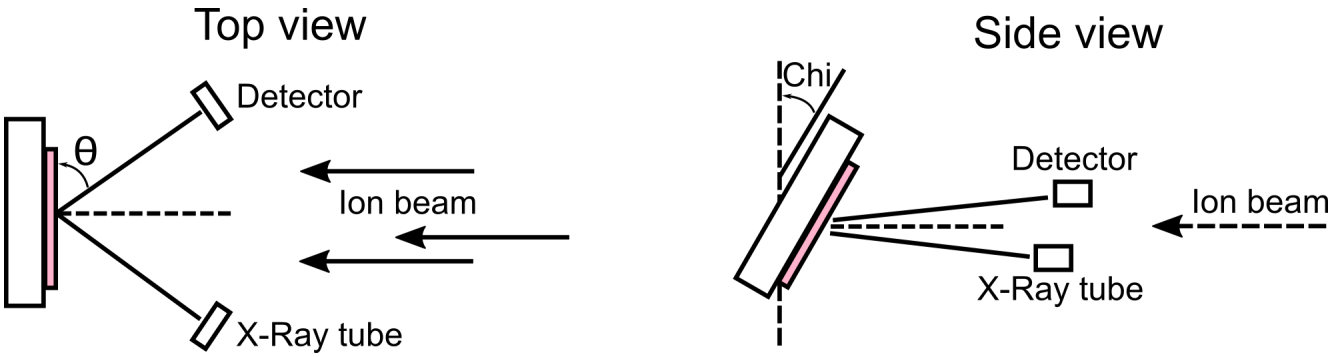

Figure 4.7: Scheme of on-line XRD measurement system at M2 beamline.

Samples were glued with epoxy on a silicon wafer with silicon wafers (fig. 4.8) being subsequently glued on a copper holder plate. Series of 4 samples (YPO_4, $TmPO_4$ and $ErPO_4$ crystals for XRD measurement and luminescence target) were mounted on a moving stage. For all the samples, positions of ideal diffraction conditions (sample orientation where desired diffraction peak has maximal intensity) were noted and applied with each sample change. Irradiation was done with ion beam sweeping over the selected sample until the specified fluence was accumulated. Fluence (re)calculation was done automatically before and after each fluence step.

Analysis of samples by the X-Ray diffraction measurements was done using:

- θ-2θ scans for determination of behavior of main reflexes. Parameters of measurements:
  - 2θ angle: 15° ... 110°,
  - 2θ step: 0.02°,
  - number of accumulations: 10.
- measurements varying Chi angle (fig. 4.7) with θ set on the particular reflex for additional information on behavior of single crystal under the irradiation. Parameters of measurements:
  - stepscan 5.0 sec,

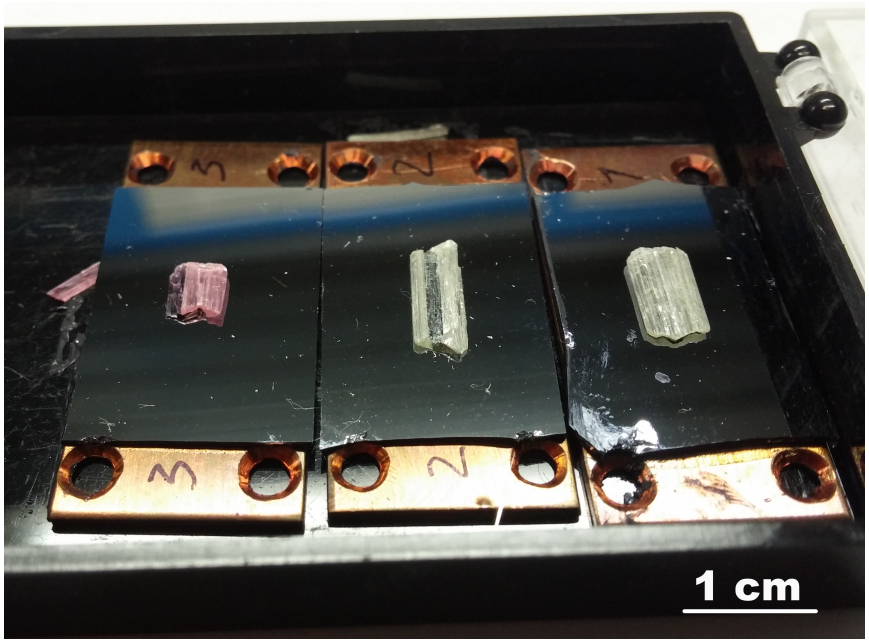

Figure 4.8: Photo of samples used for online XRD measurements.

- 2θ angle: -10° ... 10°,
- 2θ step: 0.2°,
- number of accumulations: 10.

System doesn't give an opportunity to vary Omega angle, so measurement geometry was restricted to theta and Chi angles.

4.3.2 Small-angle X-ray scattering (SAXS)

For the TEM and SAXS measurements, monazite samples were irradiated with swift heavy ions (2.2 GeV ^{197}Au) up to the fluence of 5×10^{10} ions/cm^2. Afterwards samples were mechanically polished up to the thickness below 50 μm. After the polishing $NdPO_4$ sample was broken into two parts. One of the parts was used for SAXS measurements and another one was studied by transmission electron microscopy (TEM). Both TEM and SAXS measurements were done on the $NdPO_4$ crystal irradiated by 2.2 GeV Au ions, whereas $NdPO_4$ samples exposed to the high fluences (and subsequently measured by Raman spectroscopy) were irradiated by 2.1 GeV Au ions. Difference in 0.1 GeV of ion energy between crystals used for TEM/SAXS and Raman spectroscopy measurements appears due to coverage of high fluence $NdPO_4$ samples by aluminum foil for the additional mechanical fixation. Difference of impacting ion energy of 0.1 GeV considered to be negligible for macroscopic properties change.

Small-angle X-ray scattering (SAXS) measurements were performed at the Australian Synchrotron in Melbourne. The energy of X-rays was 11 keV (λ = 1.127 Å). The measurements were performed using Pilatus 1M detector for a q-range of $0.01 < q < 0.3$ Å^{-1}. The samples

were placed under the X-ray beam in the way where tracks are oriented having angle of 0 to 10 degrees between the tracks and X-ray directions. The distance from sample to the detector was 1.48 m. Data obtained from X-ray scattering was fit by the model that assumes hard edge cylindrical tracks of constant density. Variation or track radii within the sample thickness was also taken into account and is represent as "polydispersity" parameter.

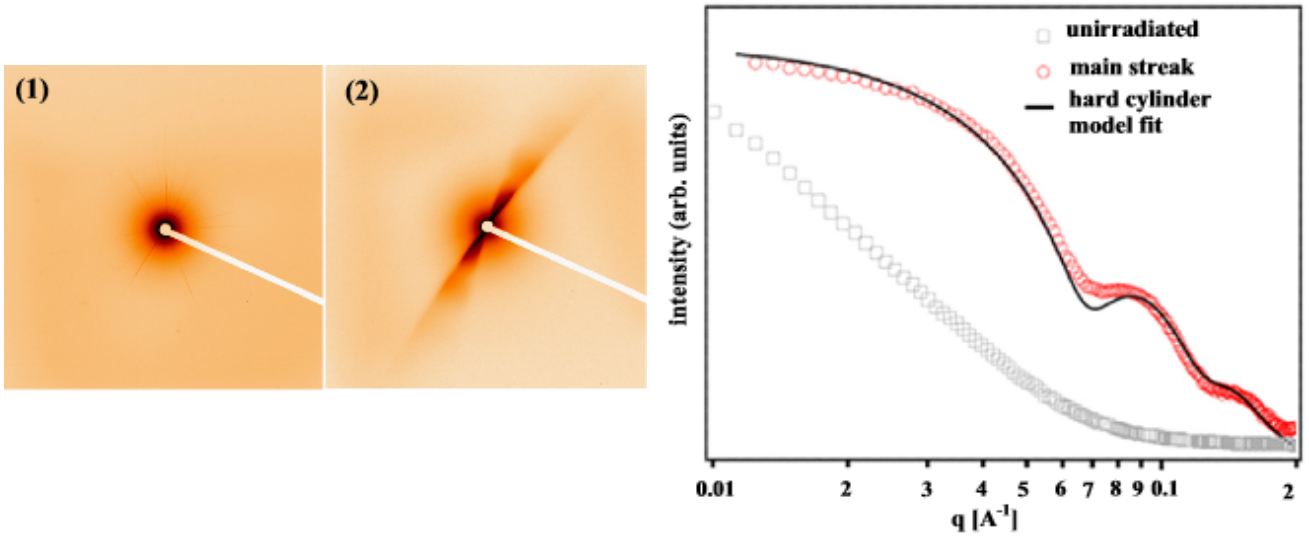

(a) (b)

Figure 4.9: SAXS measurements of zircon irradiated with 2.0 GeV ^{181}Ta ions to a fluence of 10^{11} ions/cm^2 [69]; a) detector image; b) derived intensities as a function of scattering vector q for the case of nonirradiated (gray) and irradiated (red) crystal. ©(2017) reprinted with permission from Elsevier.

Reflexes of nonirradiated samples during SAXS measurements doesn't have any features. In the case of irradiated crystals, reflexes on the detector image will be accompanied by the additional intensities that are induced by the X-ray scattering on the extended objects of cylindrical shape (ion tracks). Modeling of possible scattering profiles for the case of various cylinders was made to determine the best agreement between scattering data and computational model. Radius of cylinder that provides best fit to the SAXS is represent as track radius for particular ion in certain material. Figure 4.9 represent SAXS measurement of zircon irradiated with 2.0 GeV ^{181}Ta ions to a fluence of 10^{11} ions/cm^2 [69]. Detector image is shown on fig. 4.9(a) and derived intensities of small-angle X-ray scattering together with the fit are shown on fig. 4.9(b).

4.3.3 Transmission electron microscopy (TEM)

Sample preparation for TEM measurements of neodymium phosphate ($NdPO_4$) is described in section 4.3.2. The sample was mechanically polished below 50 μm and subsequently further thinned down by the ion milling. The sample was placed on the carbon grid and measured by a JEOL TEM. Bright-field images were taken for the $NdPO_4$ sample irradiated by 2.2 GeV Au ions

up to the fluence of 5×10^{10} ions/cm^2. Due to the sample annealing under the focused electron beam it was not possible to obtain high resolution TEM images.

4.3.4 Atomic force microscopy (AFM)

The holmium phosphate ($HoPO_4$) sample irradiated up to 5×10^{10} ions/cm^2 was measured by Dimension FastScan AFM spectrometer from Brucker [70]. No sample treatment was done before the measurement. Natural surface of a crystal provided sufficient flatness to obtain AFM measurements. Images were taken in the deflection mode to obtain better quality of surface imaging and using height sensor - to have absolute scale for size of defects present at the sample surface.

4.3.5 Scanning electron microscopy (SEM)

The SEM imaging of samples was performed at the LOT-Quantum Design in Darmstadt using a Phenom XL desktop scanning electron microscope (SEM). Phenom XL desktop SEM is equipped with a back scatter detector (BSD) and CeB_6 (cerium hexaboride) source. Accelerated voltages available for the system lie in the range of 4.8 - 15 kV. Samples were measured in the vacuum of 10^{-1} mbar. No special sample preparation was done. Irradiated and virgin crystals were placed on a holder and subsequently transfered to the measurement chamber.

5 Results and Discussion

5.1 Ion beam induced changes of macroscopic properties of $LnPO_4$

The irradiation of $LnPO_4$ single crystals with swift heavy ions significantly influences the macroscopic properties and drastically affects the mechanical stability of samples. A feature that could be observed throughout the whole series of irradiated lanthanide phosphates is a change of sample color within the irradiated layer. Many of the $LnPO_4$ single crystals have extraordinary colors (fig. 3.1), thus revealing an obvious difference between the bright noble clarity of a virgin crystal and the dull opaque layer of the irradiated material. The thickness of the modified layer based on the optical observation is $\sim 15-20\%$ lower than the range calculated with the SRIM-2010 code. The discrepancy could be related to the inaccuracy of ion range calculation in SRIM code or might appear due to lack of precision in optical measurements in semi-transparent crystals (fig. 3.11).

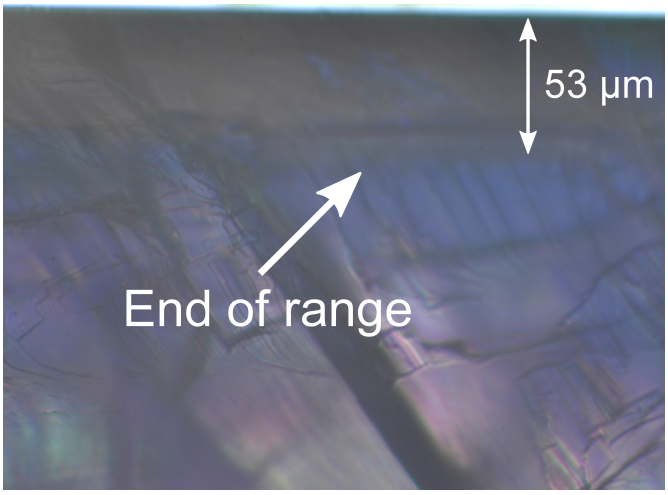

Figure 5.1: Optical image of $NdPO_4$ single crystal irradiated with 2.1 GeV Au ions at 5×10^{11} ions/cm^2. The photo displays the cross section of the sample.

Figure 5.1 shows the optical image of a $NdPO_4$ single crystal irradiated with 2.1 GeV Au ions up to a fluence of 5×10^{11} ions/cm^2. The change of color and opaqueness of the irradiated layer is easily identified. The SRIM-2010 code gives a range of 65 μm for 2.1 GeV Au ions in $NdPO_4$, whereas the analysis of the optical image suggest value of about 53 μm. The same trend is observed for both monazite and tetragonal $LnPO_4$ crystal structures.

The irradiation with swift heavy ions often results in an increase of the irradiated layer volume (so called swelling) due to accumulation of defects and amorhpization. This leads to the

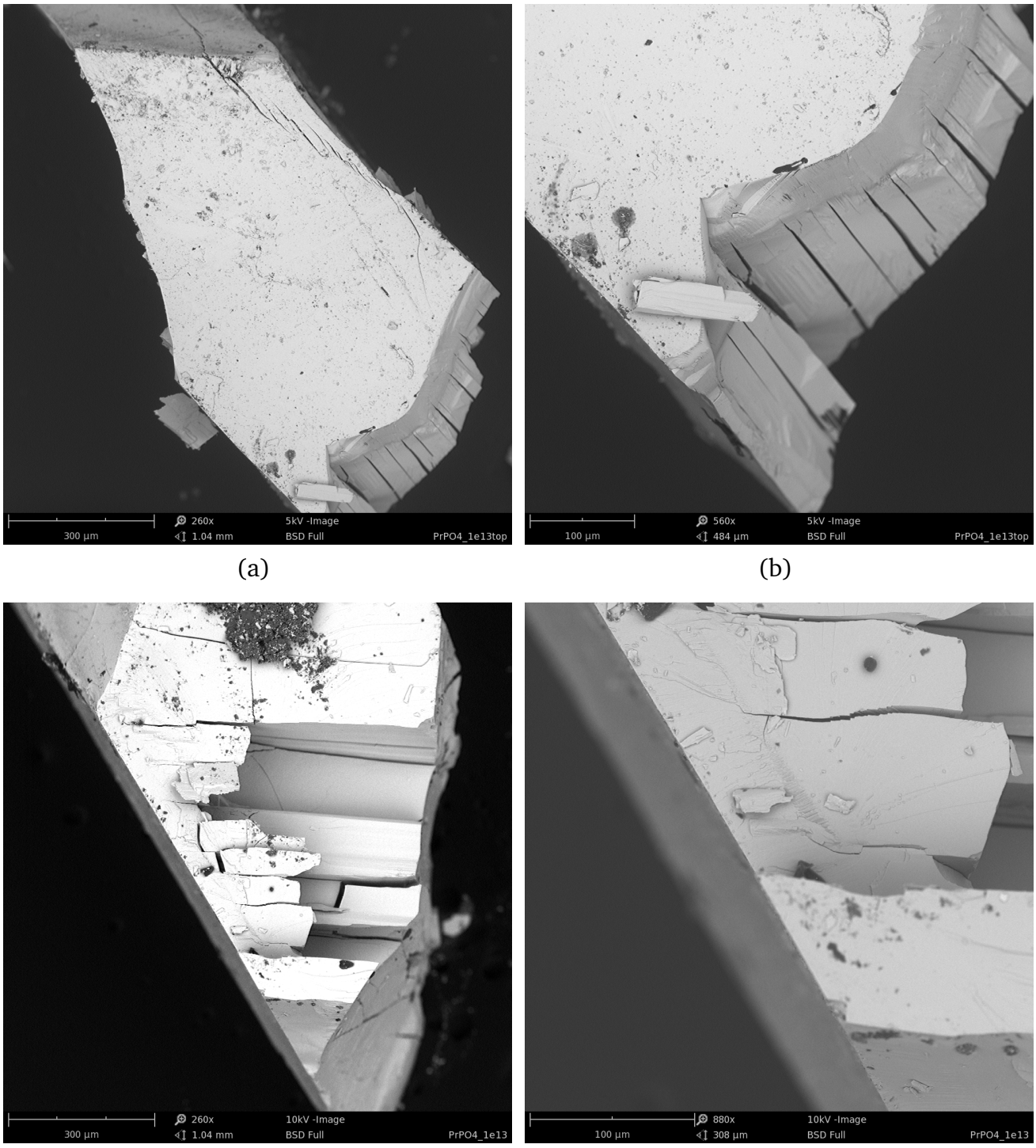

(a) (b)

(c) (d)

Figure 5.2: SEM images of $PrPO_4$ irradiated with 2.1 GeV Au ions at a fluence of 10^{13} ions/cm^2: a,b) view on irradiated sample surface; c,d) cross section view of the crack.

formation of stress in particular at the boundary between irradiated and nonirradiated layer. Already at a fluence of 5×10^{11} ions/cm^2, the samples became mechanically unstable and the crystals handling was very delicate due to their embrittlement.

Figure 5.2(a) shows SEM images of a surface exposed to the ion beam for a single crystalline $PrPO_4$ sample irradiated with 2.1 GeV Au ions up to a fluence of 10^{13} ions/cm^2. The sample is a part of larger crystal that after irradiation-induced embrittlement fractured into several pieces. The only other remaining facet of $PrPO_4$ crystal could be observed at the upper part of fig. 5.2(a). All other sides of the sample are formed due to sample cracking as a result of excessive stress release. Swelling results not only in the increase of thickness of the irradiated layer, but also in lateral expansion. The structure of the cracks on fig. 5.2(b) illustrates this effect by a series of cracks that start at the interface and propagate though the crystal down to the bottom surface. The direction of crack propagation and its orientation relative to the irradiated surface depends on the crystal structure. In the case of monoclinic $LnPO_4$, the cracks are orientated at 45° with respect to the irradiated surface. This can be clearly seen on fig. 5.2(c) when the $PrPO_4$ crystal is inspected sideways. For the tetragonal $LnPO_4$ group, the stress analysis is more difficult because the virgin zircon-type $LnPO_4$ (tetragonal) crystals are brittle and contain many cracks even before the irradiation. It is, thus, problematic to identify further cracks induced by the ion bombardment. However, a closer look on the edge of irradiated $PrPO_4$ sample (fig. 5.2(d)) reveals a difference in morphology of irradiated and virgin material.

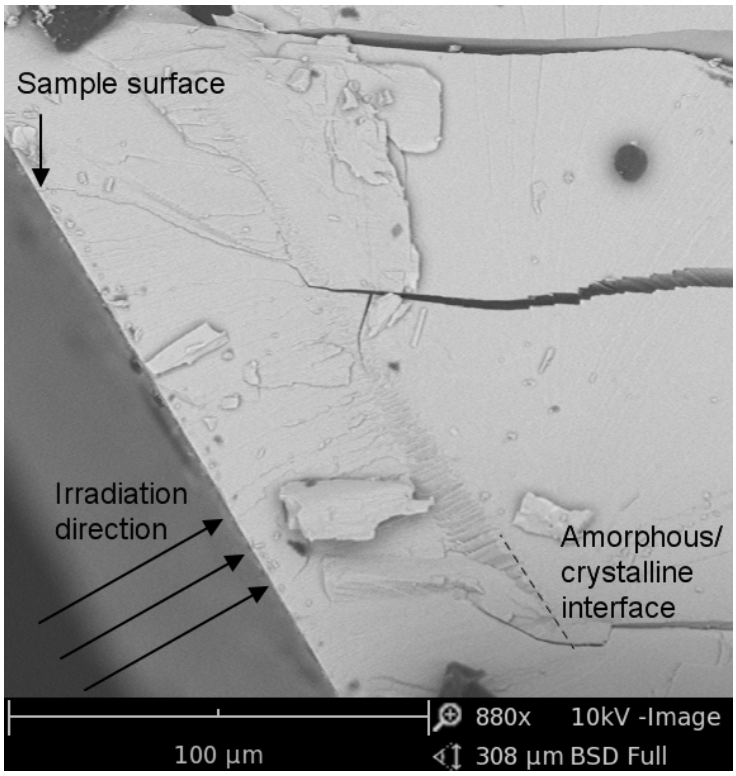

Figure 5.3: SEM image of $PrPO_4$ single crystal irradiated with 2.1 GeV Au ions at 10^{13} ions/cm^2. Direction of irradiation and ion range are indicated.

Stress relaxation and sample fracturing in the region of crystalline material results in the cleavage of atomic plane leaving flat facet. Crack propagation inside of irradiated amorphous layer leaves a series of features that make an obvious distinction between damaged and crystalline part of sample material. Figure 5.3 shows SEM image of $PrPO_4$ sample irradiated by 2.1 GeV Au ions up to the fluence of 10^{13} ions/cm^2 . SRIM code gives a value of 65 μm for 2.1 GeV ^{197}Au ion range in $PrPO_4$. The ion range deduced from the SEM contrast between the irradiated and virgin zone of the crystal is roughly 50 μm. This value is in a good agreement with optical image analysis provided in the this section.

Apart from the radiation-induced mechanical instability of $LnPO_4$ crystals, a positive effect was observed in tetragonal lanthanide phosphates. Polishing of virgin single crystals of zircon-type $LnPO_4$ is practically unfeasible due to their brittleness. Samples cleave immediately and whole crystals rapidly fragment into small platelets. Providing a low ion fluence of 5×10^{11} ions/cm^2 allows successful polishing of the crystals down to the irradiated-virgin interface and even further. This effect could be explained by the formation of amorphous ion tracks and will be discussed in more details in the following sections.

5.2 Analysis of radiation damage in Nd and Ho phosphates

5.2.1 Insight into measurements of radiation damage in $NdPO_4$ and $HoPO_4$

Before presenting and discussing the analysis of radiation damage in $NdPO_4$ and $HoPO_4$, I would like to provide some comments on the irradiation conditions and their outcome for the particular measurements of damage inside of the material.

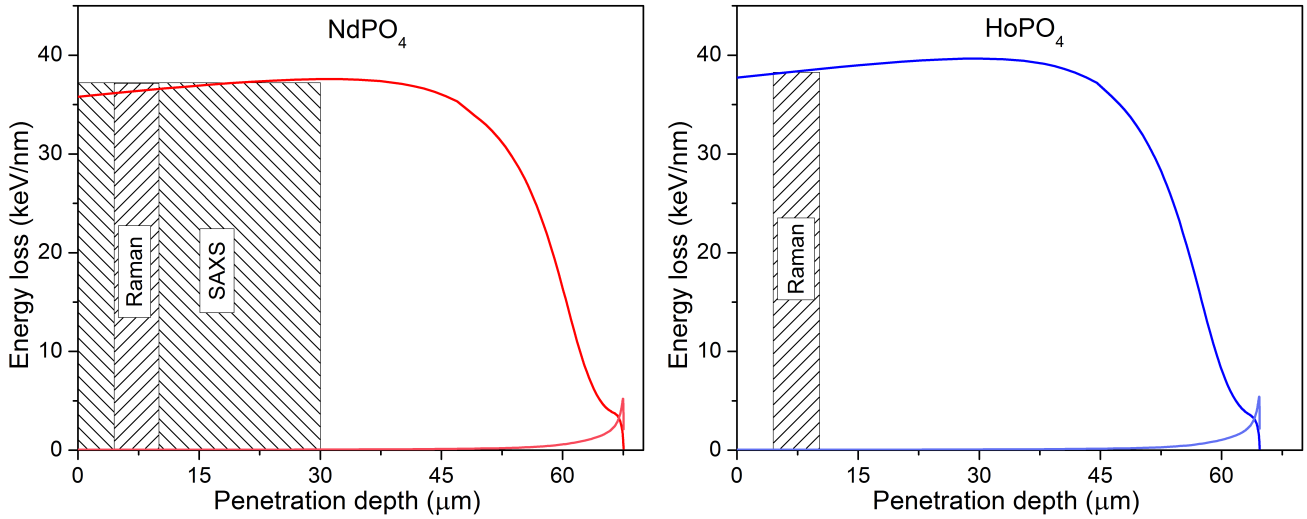

Figure 5.4: Values of stopping powers along the ion range inside of material with the specifications of the sample volume that was analyzed using particular technique. Figures are done based on SRIM code [35] calculations of electronic and nuclear energy loss of 2.1 GeV Au ion in: a) $NdPO_4$; b) $HoPO_4$.

Figure 5.4 represents the nuclear $(\frac{dE}{dx})_n$ and electronic $(\frac{dE}{dx})_e$ energy loss of 2.1 GeV ^{197}Au ion in $NdPO_4$ and $HoPO_4$. The solid lines correspond to SRIM calculations with the Bragg maximum close to 38 keV/nm for $NdPO_4$ and 40 keV/nm for $HoPO_4$. Raman spectroscopy measurements were done at a distance of 7 μm from the surface (details in section 4.2), so the electronic stopping power in the measured region is ∼36.5 keV/nm for $NdPO_4$ and ∼38.5 keV/nm for $HoPO_4$. The different shaded areas indicate the energy loss regime of samples analyzed by SAXS (35.7 - 37.7 keV/nm) and Raman spectroscopy (36.5 keV/nm - $NdPO_4$, 38.5 keV/nm - $HoPO_4$). For SAXS analysis the irradiated $NdPO_4$ sample was thinned down to ∼30 μm. SAXS yields information about track radii throughout the complete sample thickness. Within the 30 μm thin sample the energy loss varies by 2 keV/nm. In the SAXS analysis a change of track radii due to different $(\frac{dE}{dx})_e$ is accounted by polydispersity. The SAXS sample was split and was also used for TEM measurements, where before the TEM it was thinned down by ion milling to the thickness of few micrometers. Lastly, AFM measurements show hillocks, the features of sample surface that are caused by the appearance of damage in the ion tracks when expansion of irradiated volume causes occurrence of bumps on the sample surface. Hillocks are

not necessary directly correlated with the amorphous tracks, but are rather clear visualizations of damage present inside of the sample material.

5.2.2 Radiation damage in monoclinic $NdPO_4$

Crystals of virgin neodymium orthophosphate ($NdPO_4$) produce Raman spectra with a series of sharp intense peaks (detailed information is provided in section 3.1). The evolution of structural changes in $NdPO_4$ with increasing ion irradiation is investigated by analyzing Raman spectra recorded at different ion fluences (fig. 5.5). The irradiation was performed by 2.1 GeV Au ions for fluences between 5×10^{11} and 10^{13} ions/cm^2 in the regime of quasi-continuous irradiation with the pulse length of 5 ms and 50 Hz repetition rate. Ion flux value was kept constantly around 3×10^{8} for all the samples. The irradiation of $NdPO_4$ leads to a decrease of the area and the intensity of all Raman peaks (figs. 5.5(a) and 5.5(b)). Direct impact model [71] was used for quantification of radiation damage in $NdPO_4$ and determination of track radius for Au ion in this material. We assume here first (and that will be proven later in this section) that each Au ion impacting the $NdPO_4$ crystal produces elongated amorphous region along its trajectory, so called ion track. Outside of this ion track, remaining volume of material persists undisturbed unless another ion hits particular spot on the surface producing additional track. Amorphization of material lies in the accumulation of such ion tracks. Sample fully undergoes a crystalline to amorphous transition when the exposed surface is completely covered by the ion tracks.

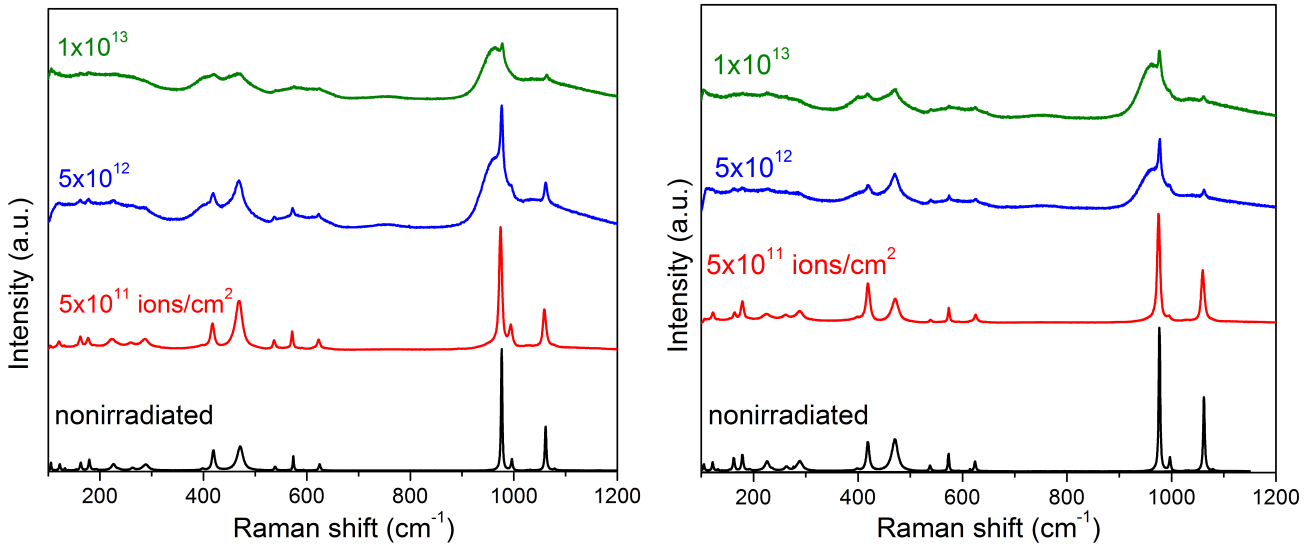

Figure 5.5: Raman spectra of pristine and irradiated (50 Hz, 5 ms, Au ions) monoclinic $NdPO_4$ obtained with different laser excitation wavelength. Results are presented as a function of fluence for: a) blue laser (λ=473.05 nm); b) red laser (λ=632.82 nm).

For the quantitative analysis of radiation damage we will trace the change of certain parameters (analysis of amorphous fraction at a particular fluence, determination of track radius etc.).

The analysis of the Raman spectra of irradiated $NdPO_4$ is not trivial because they contain apart of sharp crystalline peaks a few broad humps that appear and change with irradiation. We can assign amount of crystalline material within the sample to the parameters of sharp peaks in Raman spectrum and the amount of amorphous one to the area and intensity of humps that appear in the spectrum. Figure 5.6 illustrates the complex analysis of Raman spectrum of $NdPO_4$ sample irradiated at 5×10^{12} ions/cm^2 and measured with the blue laser (λ=473.05 nm). Background subtraction and peak fitting was performed using Fityk 0.9.7 software [72]. Analysis was focused on Raman bands corresponding to the stretching and pending modes of the PO_4 tetrahedron (850 to 1250 cm^{-1}), as peaks in this area can be explicitly resolved from the noise even at the highest fluence. There is no ideal universal way for background subtraction and simple linear background fit was used in both area of interest (red lines at the bottom image on fig. 5.6). In the area between 350 and 500 cm^{-1} the best fit is obtained by decomposition into two Raman Lorentzian shaped (for the simplicity I will call them "crystalline") peaks and two Gaussian (referred as "amorphous" later) peaks. Between 500 and 650 cm^{-1} the experimental data is fitted by two Gaussian peaks and three Lorentzian peaks. Finally, in the region of the stretching modes around 1000 cm^{-1}, the deconvolution includes a single broad "amorphous" peak and two sharp "crystalline" peaks. Overall fit quality was judged based on residual curves that are shown for each fit (fig. 5.6).

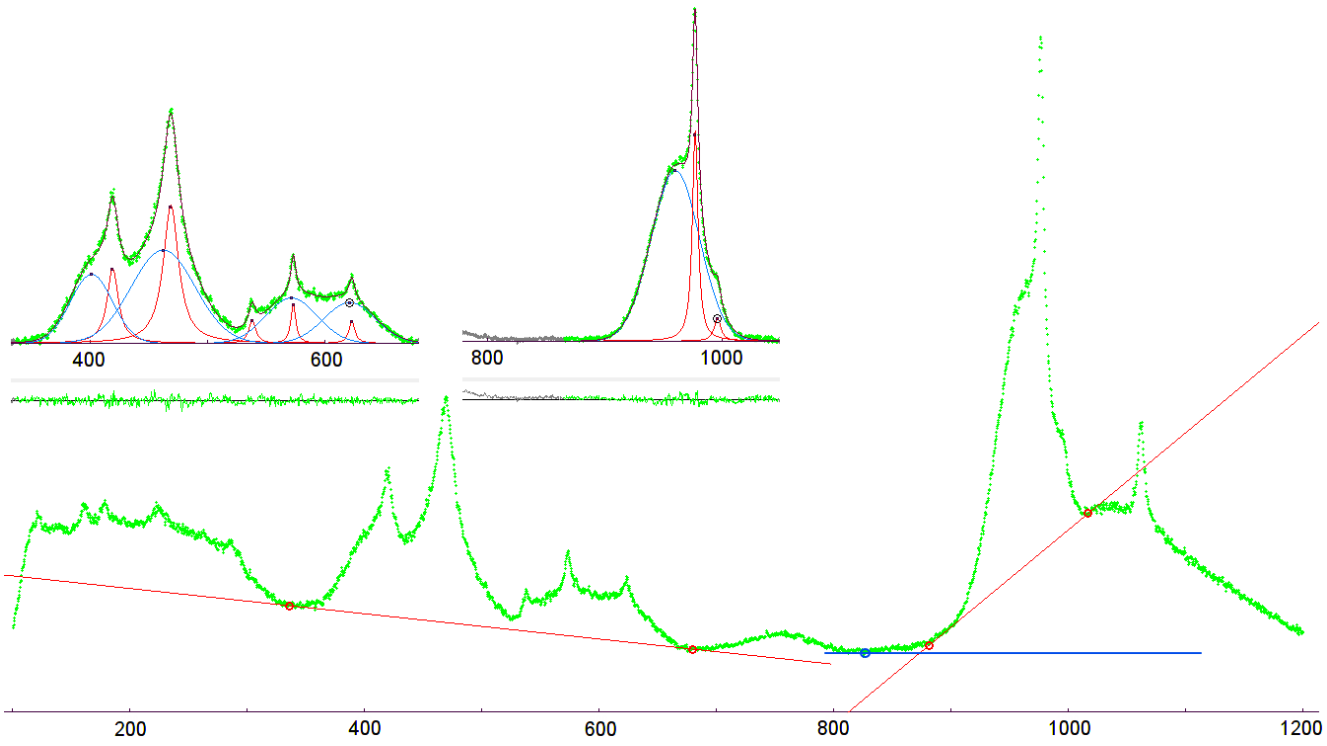

Figure 5.6: Deconvolution procedure of Raman spectrum (blue laser: λ=473.05 nm) of $NdPO_4$ sample irradiared by 2.1 GeV Au ions (50 Hz, 5 ms) at 5×10^{12} ions/cm^2. Straight line was used for background subtraction. Lorentzian shaped peaks (red) were attributed to crystalline and Gaussian shaped peaks (blue) to the amorphous phase.

Area and intensities of peaks derived from the fitting procedure were used to quantify remaining crystallinity according to the formulas:

$$c_a = \frac{A_{\text{cr}}}{A_{\text{cr}} + A_{\text{am}}}, \qquad c_i = \frac{I_{\text{cr}}}{I_{\text{cr}} + I_{\text{am}}}, \tag{5.1}$$

where c_a corresponds to the crystalline fraction calculated based on the ratio of analyzed peak area, c_i denotes the crystalline fraction calculations using peak intensities, and $A_{\text{cr}}(I_{\text{cr}})$ and $A_{\text{am}}(I_{\text{am}})$ are the area (intensity) of the crystalline and amorphous peaks, respectively. Obviously, the remaining amorphous fraction (a_a and a_i) at any given fluence step can be deduced from a_a = 1 - c_a and a_i = 1 - c_i. Cumulative intensity equal to sum of "crystalline" and "amorphous" peak intensities/area in the particular spectral region (350 to 500 cm^{-1}, 500 to 650 cm^{-1} and 850 to 1200 cm^{-1}) was used to evaluate the damage evolution.

According to the direct-impact model, the amorphization cross-section σ_a can be deduced from a fit of the crystalline fractions as a function of the ion fluence using the following exponential law:

$$c_a = \exp(-\sigma_a \cdot \Phi), \tag{5.2}$$

where c_a is the crystalline fraction from the analyzed peak areas, σ_a is the amorphization cross-section and Φ is the ion fluence. Assuming cylindrical track geometry, the track radius (R) for a particular ion can directly be calculated from the damage cross-section using formula:

$$\sigma_a = \pi \cdot R^2. \tag{5.3}$$

On fig. 5.7 the evolution of the crystalline fraction based on peak areas is shown as a function of accumulated fluence for $NdPO_4$ irradiated by 2.1 GeV Au ions. The crystalline fraction at each fluence step was calculated according to eq. (5.1). The data was fit by the exponential law (eq. (5.2)) suggested by the model of direct-impact amorphization. Size of points at the figures represents the error bars deduced from 10 measurements taken at different spots (details in section 4.2). For the measurements using the blue (fig. 5.7(a)) and red (fig. 5.7(b)) lasers, we can see significant deviation and scattering of data points from the expected trend. One of possible sources of this discrepancy could be limitation of Raman spectroscopy data for this particular kind quantitative analysis. However, measurement of the same irradiated sample at many different spots (fig. 4.5(a)) produces sets of very consistent data with the peak intensities varying by a few percents. Another possible source of errors could be our selection of parameters that we use for the quantification of crystalline and amorphous fractions. Calculation of crystalline or amorphous fractions implies that we use parameters (in this case, peak parameters) that **fully**

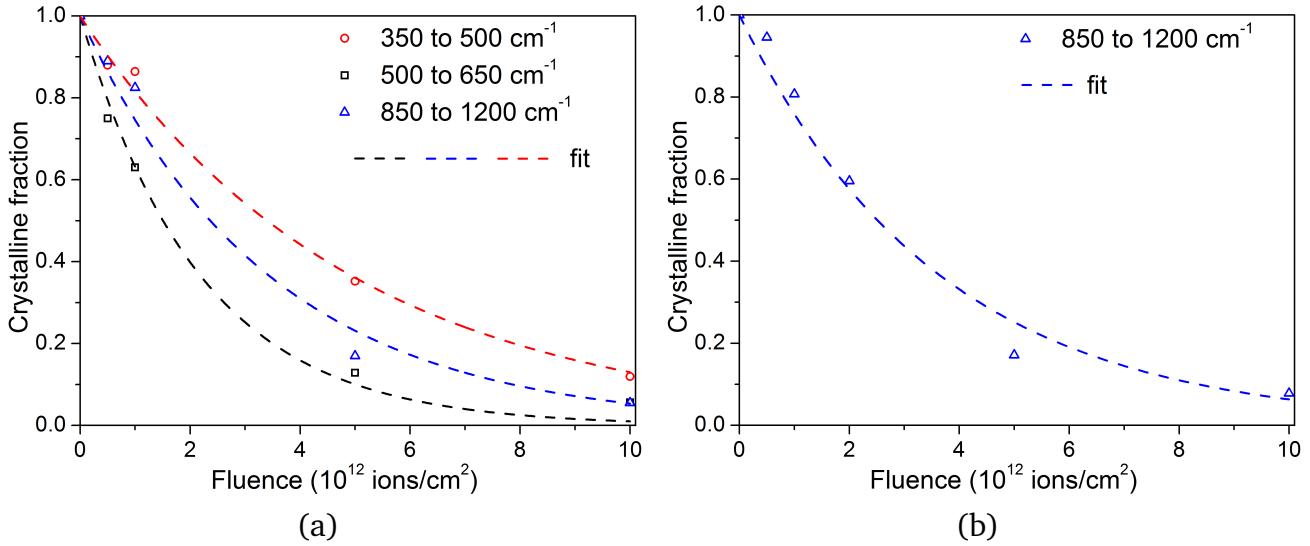

Figure 5.7: Evolution of crystalline fraction in $NdPO_4$ irradiated with 2.1GeV Au ions. Crystalline fractions were calculated based on area of peaks in specified spectral range: a) blue laser (λ=473.05 nm); b) red laser (λ=632.82 nm). Lines are exponential fit to the experimental data (eq. (5.2)).

represent states of material. Strictly speaking, different Raman modes could possibly decay with the irradiation at a different rates (that requires analysis of many Raman bands) what makes some sharp peaks vanish faster that the others. We cannot be sure either, that the broad humps fully represent amorphous phase. We clearly have Raman spectra containing contributions from two phases. The ratio of this contributions follows a change of irradiated sample volume. In addition, the changes in sample transparency (see section 5.1 and fig. 5.1) within the irradiated layer will influence ratio of Raman signal from amorphous and crystalline sample material. For instance, at low fluence steps, laser can penetrate deep inside of material, and measured Raman spectra contain, let's say, 10% of a signal from the irradiated sample volume. At larger fluences, the amorphized sample material scatters laser light, and laser light penetrates much less inside of crystal. Measurement of highly irradiated sample will contain now, for instance, 50% of a signal from the irradiated sample volume. A solution of this problem could be to renormalize the Raman spectra and compare absolute values of Raman peaks that belong to the same phase. A detailed description of the renormalization procedure is represented in section 5.2.3. In the following we focus on the difference in the fitting of Raman spectroscopy data and deduce track radii for $NdPO_4$ after spectra renormalization.

Figure 5.8(a) shows the area of symmetric stretching modes of PO_4 tetrahedra in the Raman spectrum of $NdPO_4$ irradiated by 2.1 GeV Au ions (frequency 50 Hz, pulse length 5 ms) up to a fluence of 5×10^{12} ions/cm^2. The background was subtracted by a horizontal line fitted through the single point serving as local signal minimum closest to the area of interest (blue line at the bottom image on fig. 5.6). The broad band is deconvoluted by three Gaussian peaks for the amorphous contribution: located at 960, 1034 and 1055 cm^{-1}. We will see in section 5.2.3 that

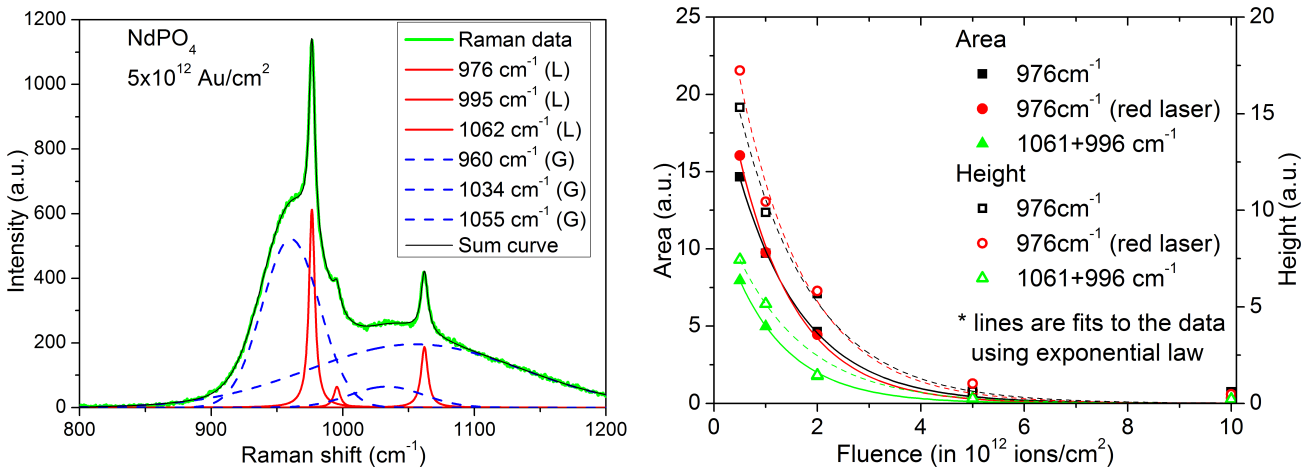

Figure 5.8: a) Raman spectra of $NdPO_4$ irradiated by 2.1 GeV Au ions (frequency 50 Hz, pulse length 5 ms) at 5×10^{12} ions/cm^2; background is subtracted as horizontal line; spectrum deconvolution is performed using Fityk software [72]; peaks attributed to the remaining crystalline part are fit by Lorentzian shaped band and Gaussian fit is used for the amorphous fraction. b) absolute values of peak area and intensities (heights) attributed to crystalline fraction plotted as a function of fluence. Lines are fits to the data using an exponential law.

the appearance of small hump located at 1034 cm^{-1} for $NdPO_4$, shares similarities with Raman spectra of $HOPO_4$.

The fluence dependence of the absolute values of Raman peak parameters assigned to the crystalline fraction were used for quantification of the amorphization rate. Peaks at 976 cm^{-1} (symmetric stretching mode of PO_4 tetrahedron), 995 and 1062 cm^{-1} (both belonging to the antisymmetric stretching mode of PO_4 unit) were fit as Lorentzian. The evolution of these Raman bands as a function of ion fluence is presented on fig. 5.8(b). To fit the data a slightly modified version of the exponential law from eq. (5.2) was used:

$$A = A_0 \cdot \exp(-\sigma_a \cdot \Phi), \qquad \sigma_a = \pi \cdot R^2. \tag{5.4}$$

A and A_0 represent the current and initial value of the peak area or intensity. A_0 is a free parameter for the fit and simply represents intersection point of the exponential curve with the y-axis. In the case of Raman spectra renormalization for $NdPO_4$ we can see good agreement between the experimental data and theoretical mechanism of damage production (model of direct-impact amorphization).

$NdPO_4$ irradiated by swift heavy ions was also analyzed by other experimental techniques, for instance, transmission electron microscopy (TEM). On fig. 5.9 we can see TEM image of $NdPO_4$ crystal irradiated with 2.2 GeV Au ions up to a fluence of 5×10^{10} ions/cm^2. Such a low fluence was chosen to avoid significant track overlapping and visualize damage produced by single Au

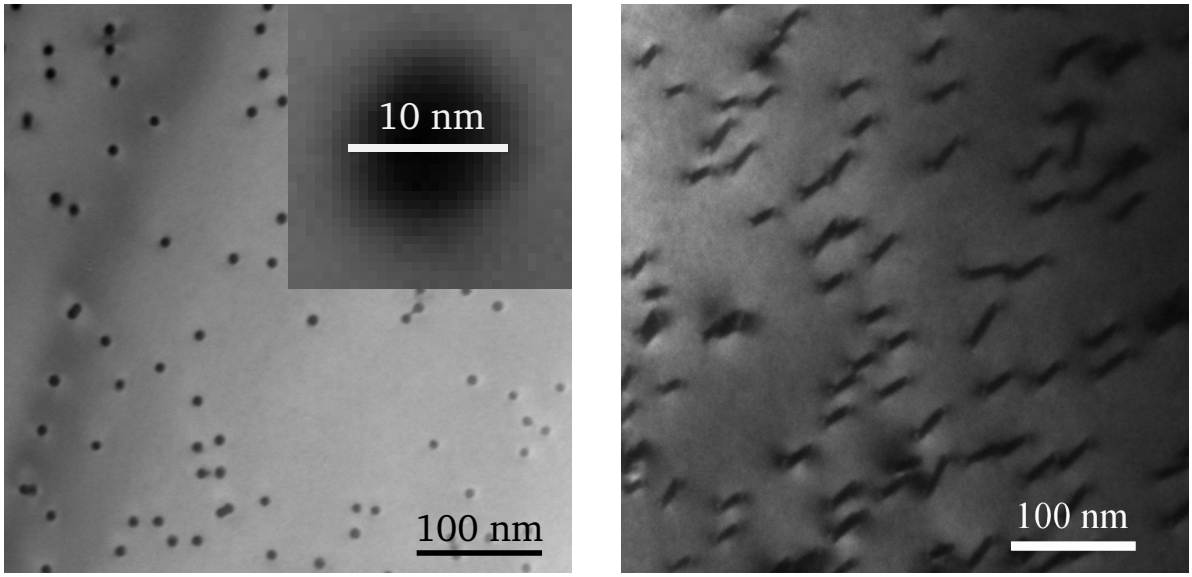

Figure 5.9: TEM bright field image of $NdPO_4$ single crystal irradiated with 2.2 GeV Au ion.

ions hitting the $NdPO_4$ crystal. High resolution TEM was not possible due to annealing of the material under the intense electron beam. However, a rough estimation of the track size was still possible and track radii were obtained by calculating the track diameter in pixels on the enlarged TEM image for 10 different tracks (table 5.1). The example of an enlarged single track is displayed in the inset of fig. 5.9.

Evaluation of effectiveness and reliability of quantitative analysis of Raman spectroscopy data could be performed via comparison of results for amorphization cross-section and track radii calculations with the measurements done using transmission electron microscopy (TEM) and small angle X-Ray scattering (SAXS). Table 5.1 provides a summary for the fit parameters using different approaches for quantitative Raman spectroscopy analysis that was discussed throughout this section. SAXS and TEM measurements were done using a single irradiated sample. The track radii are independent of the irradiation conditions (fluctuations of flux, calibration inaccuracy). Samples used for the Raman measurements were exposed up to significantly larger fluences.

Good agreement between Raman spectroscopy data and TEM/SAXS is achieved after Raman spectra renormalization. Uncertainties based on the evaluation of the amorphous and crystalline peak fractions without renormalization are significantly smaller. Thus, renormalization of Raman spectra at each fluence step is necessary to perform reliable and trustworthy quantitative Raman spectroscopy analysis. A comparison of damage cross-sections and track radii obtained before renormalization suggests track radii close to 2 nm. This value suggests extremely high radiation hardness [73]. The actual response of material to the irradiation, however, suggests, that material behaves as typical insulator. Severe cracks could be observed already at the fluence of 10^{12} ions/cm^2 and almost complete Raman spectra degradation is observed at the fluence of $5{\times}10^{13}$ ions/cm^2. In this case expected values of track radii should be closer to the case of

Table 5.1: Calculated values for amorphization cross-section and track radii for 2.1 GeV Au ion in $NdPO_4$. Analysis concern Raman measurements is done with blue laser (unless specified).

Amorphization cross-section and track radii for 2.1 GeV Au in $NdPO_4$			
Evaluation basis	Mean $(dE/dx)_e$	σ_a ($\times 10^{-14}$cm^2)	R$\pm\Delta$R[a] (nm)
Based on relative peak areas			
350 to 500 cm^{-1}	36.3±0.3	29.3	3.1±0.2
500 to 650 cm^{-1}	36.3±0.3	46.0	3.8±0.3
850 to 1000 cm^{-1}	36.3±0.3	20.4	2.6±0.1
850 to 1200 cm^{-1} (red laser)	36.3±0.3	32.3	3.2±0.2
Based on peak area (A) and height (H) after renormalization			
976 cm^{-1}(A)	36.3±0.3	77.7	5.0±0.3
976 cm^{-1}(A), red laser	36.3±0.3	88.3	5.3±0.4
996+1061 cm^{-1}(A)	36.3±0.3	92.3	5.4±0.4
976 cm^{-1}(H)	36.3±0.3	70.3	4.7±0.4
976 cm^{-1}(H) , red laser	36.3±0.3	73.7	4.8±0.4
996+1061 cm^{-1}(H)	36.3±0.3	77.0	4.8±0.4
Based on other experimental techniques			
TEM	35.7±0.1	58.1[b]	4.3±0.9
SAXS[c]	36.7±1.0	75.4[d]	4.9±0.2[e]

[a] Error for the track radius obtained from Raman spectroscopy data is calculated based on 15% inaccuracy of fluence determination.
[b] Calculated from the track radius measured directly in TEM.
[c] Detailed analysis is provided in section 5.3.1.
[d] Calculated from the track radius obtained from SAXS.
[e] Polydispersity = 0.5 nm (value for track radius change resulted from the difference of energy deposition along the ion path).

apatite (5.1 nm [21]), pyrochlores ($La_2Ti_2O_7$: 5.3 nm [69], $Gd_2Ti_2O_7$: 5.1 nm [28], $Nd_2Zr_2O_7$: 5.1 nm [26]) or zircon (5.0 nm [23]).

5.2.3 Radiation damage in tetragonal $HoPO_4$

Raman spectroscopy measurements of single crystals of holmium orthophosphate ($HoPO_4$) obtained using blue (λ=473.05 nm) and red (λ=632.82 nm) lasers showed strong luminescent contribution to the Raman spectra (fig. 5.11). In the case of measurements done by the red laser, the high intensity of the luminescence completely overwhelmed the spectrum. With the measurements times that were used to avoid detector saturation (t = 0.5 s), practically no Raman signal could be extracted from the spectra. Only the band of the symmetric stretching mode of the PO_4 tetrahedron could be found as a tiny signal around 1000 cm^{-1} (fig. 5.11(b)). Measurements with the red laser cannot be analyzed, thus all Raman data reported further in this section were obtained with the blue laser. However even with 473.05 nm excitation wavelength, the spectra contain a significant luminescent contribution, but the Raman bands

can be successfully identified. Figure 5.10 provides Raman spectra of holmium and erbium orthophosphates. Both compounds have the same crystalline structure and similar ionic radii of the lanthanide cations. The measurement conditions and sample orientation were kept identical, so Raman spectra of both crystals should contain a similar sequence of peaks. On fig. 5.10 the Raman peaks are marked with an asterix and all additional signal in the spectrum of $HoPO_4$ is attributed to luminescence.

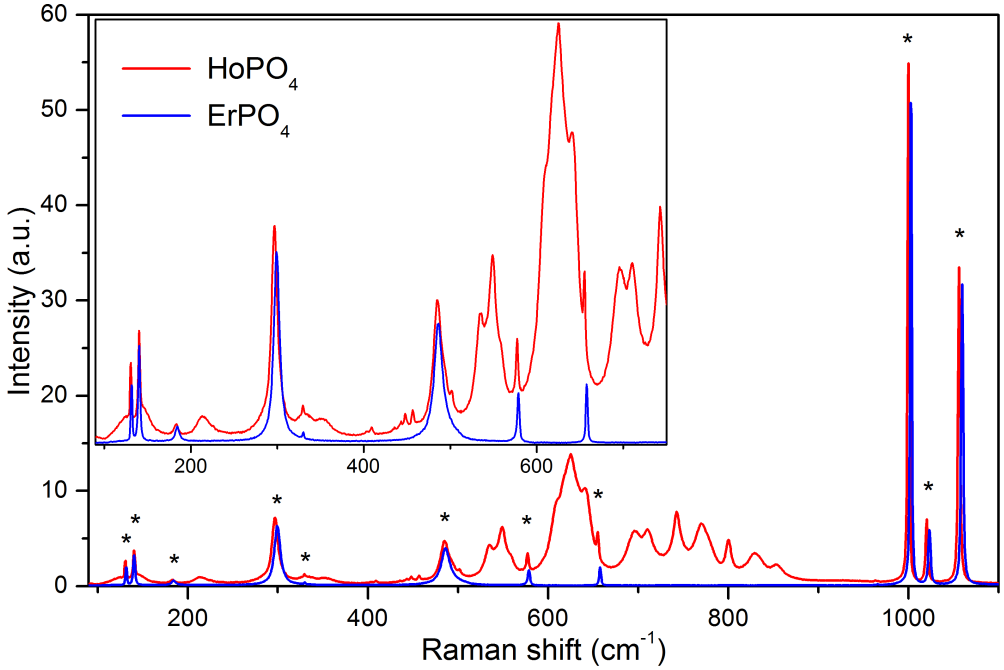

Figure 5.10: Comparison of Raman spectra of virgin $HoPO_4$ and $ErPO_4$ measured with blue laser.

The analysis of the radiation damage in $HoPO_4$ was done by tracking changes in the Raman spectra. It is important to notice, that the luminescence initially present in $HoPO_4$ spectra is also strongly affected by the irradiation. On fig. 5.11 we can see pronounced changes in the luminescent contribution to the Raman spectrum before and after the irradiation. A series of relatively sharp luminescent peaks smears out and severely decrease in intensity with the accumulation of ion fluence.

Raman spectra of $HoPO_4$ single crystals irradiated at different fluences are shown on fig. 5.12. The irradiations were performed with the 2.1 GeV Au ions (50 Hz, 5 ms) up to a fluences of 5×10^{13} ions/cm^2. For low fluence steps between 5×10^{11} and 5×10^{12} ions/cm^2 the ion flux was 10^8 ions/cm^2·s. For the high fluence irradiations between 5×10^{12} and 5×10^{13} ions/cm^2, the beam flux was increased to 10^9 ions/cm^2·s. Two samples were irradiated to the same fluence of 5×10^{12} ions/cm^2 using different flux values to test possible flux effects regarding radiation damage.

A series of Raman spectra of different irradiated $HoPO_4$ single crystals shown on fig. 5.12(a) illustrate the decrease of all band intensities with increasing fluence at 2×10^{12} ions/cm^2 around 970 cm^{-1} a new broad peak appears and further grows with increasing fluence. Similar to the

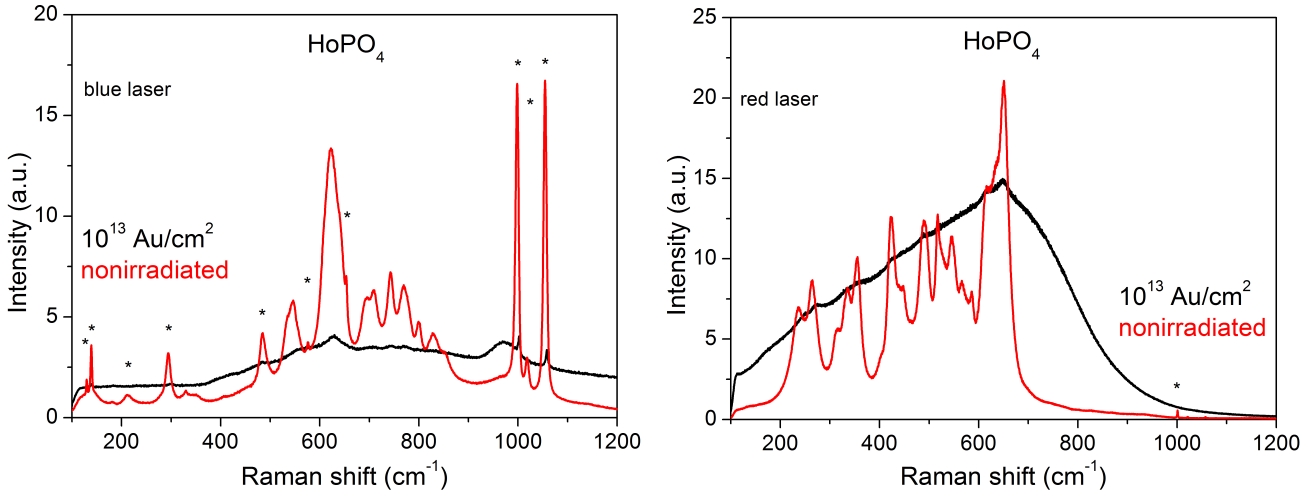

(a) (b)

Figure 5.11: Raman spectra of pristine and irradiated (50 Hz, 5 ms, Au ions, fluence of 10^{13} ions/cm^2) tetragonal $HoPO_4$ obtained with different laser excitation wavelength: a) blue laser (λ=473.05 nm), measurement time is 15 s; b) red laser (λ=632.82 nm), measurement time is 0.5s. In both cases fluorescent bands are present in the spectrum. In the case of blue laser, Raman bands are distinguishable and marked as *. In the case of the red laser, strong fluorescence overwhelms spectrum and detector saturation is observed already after 1s of measurement.

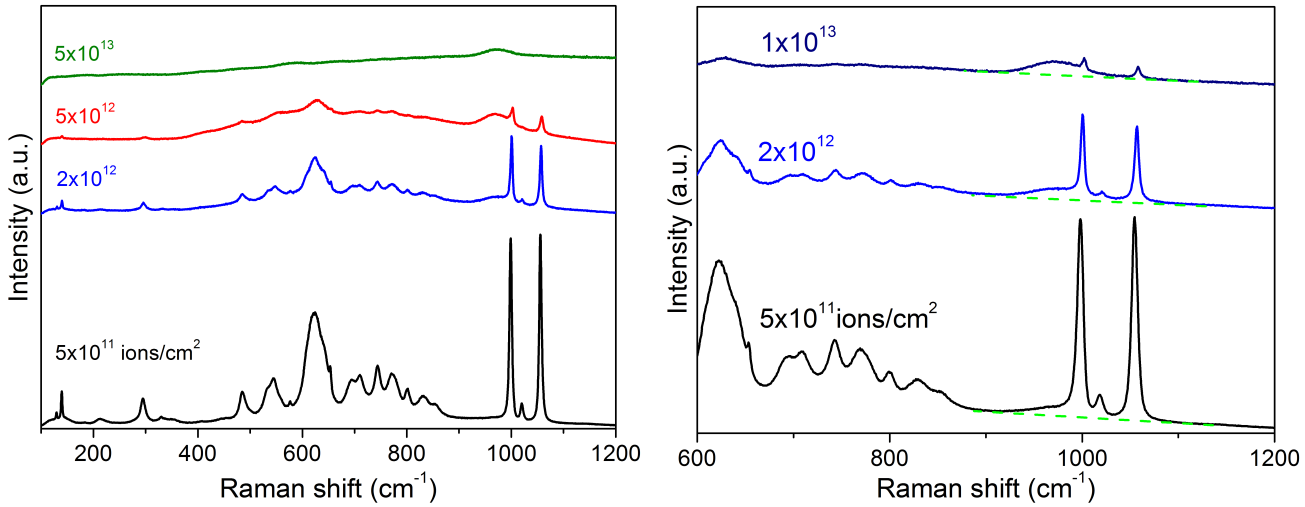

(a) (b)

Figure 5.12: Raman spectra of $HoPO_4$ crystals irradiated by 2.1 GeV Au ions (50 Hz, 5 ms) for various applied fluences: a) full spectra; b) illustration of background fit (dashed line).

case of irradiated $NdPO_4$ (fig. 5.5), this peak is assigned to the contribution from the amorphous part of $HoPO_4$. In contrast to $NdPO_4$, the irradiations of $HoPO_4$ were performed up to higher fluences and we can see that at the fluence of 5×10^{13} ions/cm^2 none of the sharp Raman peaks that were present in the spectra of the virgin material can be observed. The broad hump at around 970 cm^{-1} remains the only feature at the highest applied fluence.

The quantification of the amorphized material fraction was performed based on the intensities of sharp "crystalline" peaks and broad "amorphous" humps. The analysis of peaks in the region of the stretching modes (between 450 and 700 cm^{-1}) is particularly complicated due to the overlap of Raman and luminescent bands. The deconvolution of the amorphous fraction in the region of the bending modes is thus impossible. Whereas in the region of the stretching modes (between 850 and 1100 cm^{-1}) contains no significant luminescent contribution. In this region background subtraction was performed by a linear fit (fig. 5.5(b)).

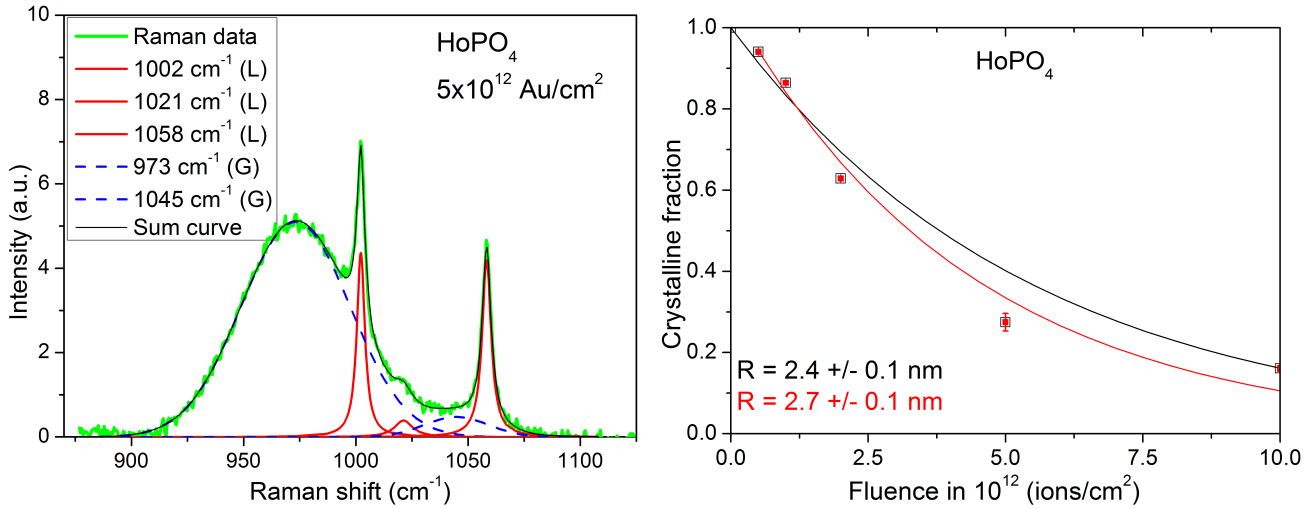

Figure 5.13: a) Deconvolution of Raman spectra of $HoPO_4$ irradiated by 2.1GeV Au ions (50 Hz, 5 ms) up to 5×10^{12} ions/cm^2; Lorentzian shaped peaks (L) are attributed to crystalline fraction (solid line) and broad Gaussian shaped (G) for the amorphous part (dashed line). b) Track radius calculation according to the exponential fit to the data that represents remained crystalline material. Crystalline fraction was estimated by the ratio of L-shaped and G-shaped peak area. Fitting function was used with and without inclusion of [0,1] data point.

The Raman bands were fit using Lorentzian shaped peaks for Raman bands assigned to the crystalline material fraction, and broad Gaussian peaks for the amorphous signals. Also here we assume a direct-impact amorphization mechanism. Each 2.1 GeV Au ion projectile produces a cylindrical track of amorphized material along its trajectory. The accumulation of such ion tracks gradually transforms the irradiated sample from the crystalline to the amorphous state. Raman spectra of irradiated $HoPO_4$ thus contain contributions from the nonirradiated part of the sample and cumulative contributions of amorphized material inside of all ion tracks.

On fig. 5.13(a) the deconvolution is shown for $HoPO_4$ irradiated up to 1×10^{13} ions/cm^2. Sharp peaks at 1002, 1021 and 1058 cm^{-1} are assigned to the crystalline fraction, while broad bands at 973 and 1045 cm^{-1} belong to the signal induced by the amorphized part. From the peak area the crystalline fraction in the sample was extracted according to eq. (5.1).

The band area as a function of ion fluence is fit with an exponential functions according to eq. (5.2) and eq. (5.4). The modified version of exponential dependence fits data better than the standard one, yielding a track radius of R = 2.7 nm (eq. (5.4)) compared to a slightly lower value of R = 2.4 nm using standard function (eq. (5.2)).

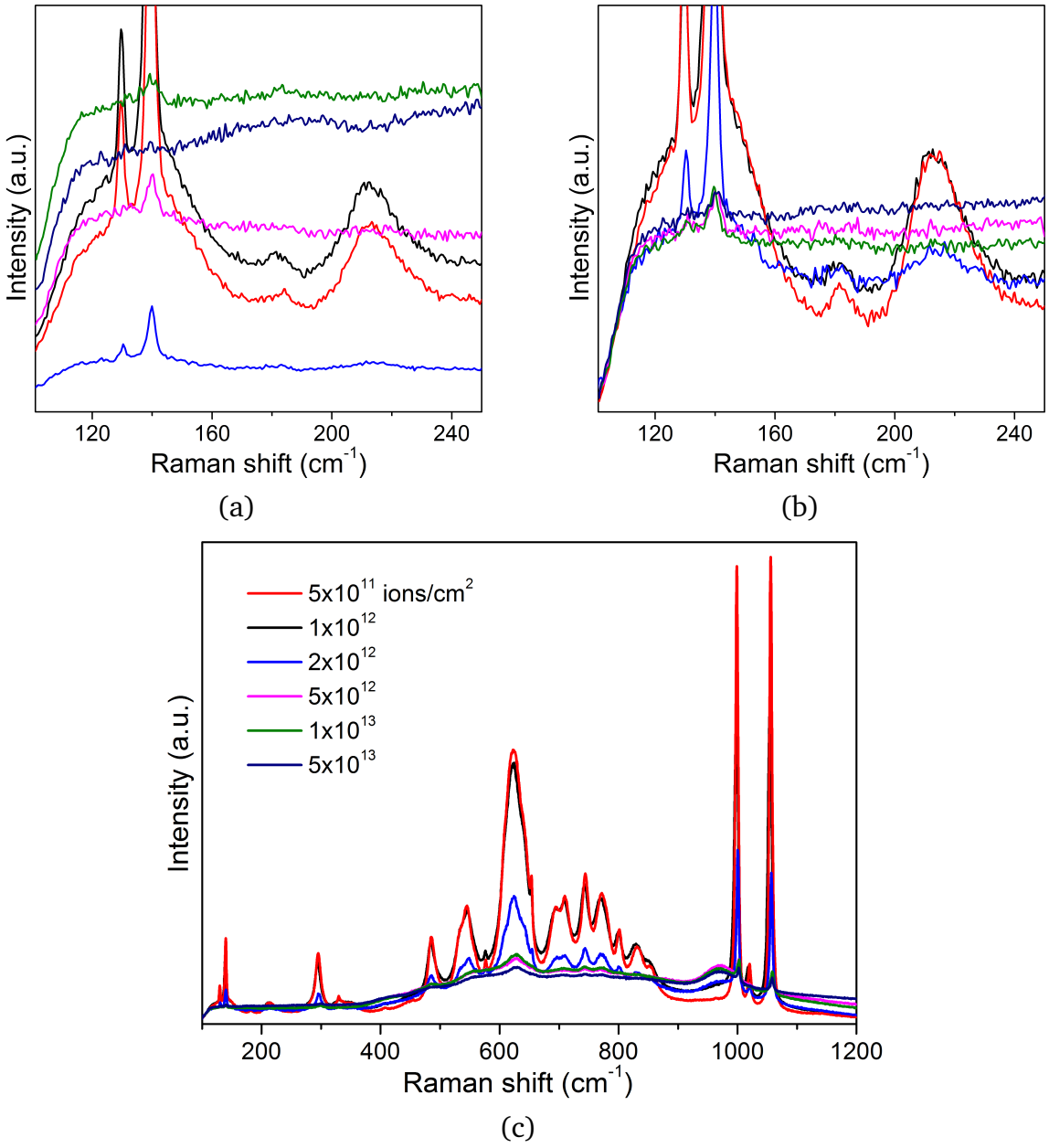

Figure 5.14: Raman spectra of $HoPO_4$ irradiated by 2.2 GeV Au ions at different fluences: a) before; b) after rescaling; c) complete Raman spectra after rescaling.

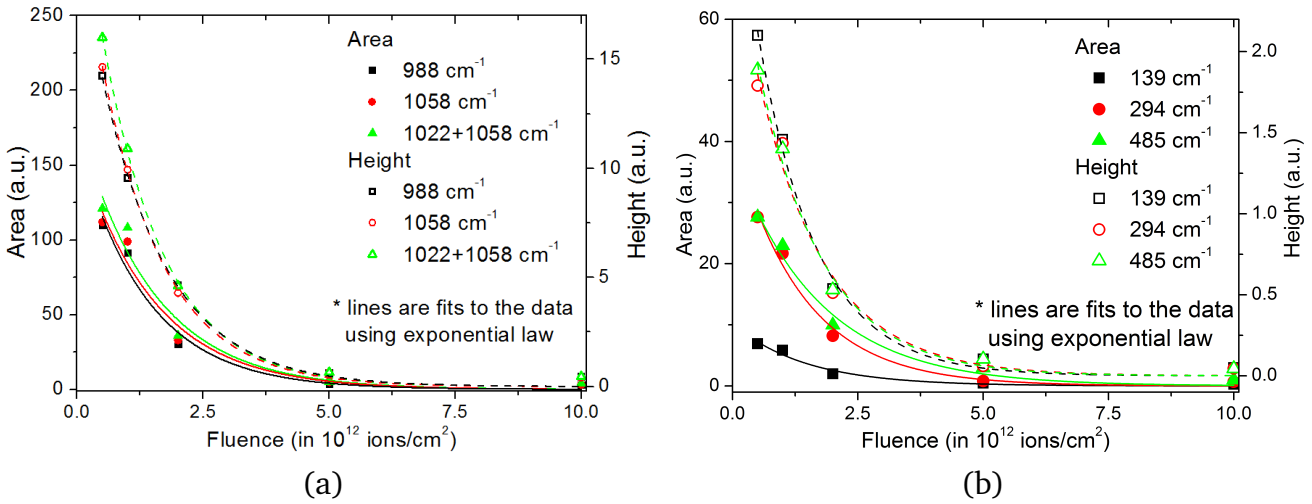

Figure 5.15: Intensities (heights) and area of specified Raman bands as a function of fluence for $HoPO_4$ irradiated by 2.1 GeV Au ions after spectra renormalization. Error bars are smaller or equal to the size of data points. Lines are exponential fit to the data. a) Analysis of peaks in the region of symmetric and antisymmetric stretching modes. b) Analysis of peaks in the region of bending and lattice modes.

The calculation of track radius derived from the crystalline fraction based on the relative amorphous and crystalline peak areas does not match well the predictions of the direct-impact amorphization model. Possible sources of such discrepancy are similar to the case of $NdPO_4$ described in previous section. Firstly, calculations of crystalline fraction based on the relative peak area or intensity, require two peaks that unambiguously and fully represent the crystalline and amorphous fractions. Secondly, the intensity of the Raman signal depends on many parameters (sample volume, measurement settings, focusing, luminescent contribution) and not all of them could be controlled. Finally, alteration of Raman signal in irradiated $HoPO_4$ resulting from changes at the amorphous and crystalline fractions will be convoluted with the influence of optical properties variation (decrease of transparency, sample coloration). Taking into account these different features, a different approach was tested.

To improve the quantitative analysis of Raman data, an alternative renormalization of spectra was used. All Raman spectra of $HoPO_4$ contain significant luminescent contribution in the whole spectral area. The signal is present even at small wavenumbers in the region that is cut off by the edge filter of the spectrometer. The renormalization was done by adjusting the slope of all Raman spectra in the region of 90...120 cm^{-1} to the same value. In this regime the data rather correlate with the properties of spectrometer itself, than with the signal from the samples. Figure 5.14(a) shows the stack of raw Raman spectra of a series of $HoPO_4$ samples irradiated by 2.1 GeV Au ions. Intensities of signal vary a lot and depend, for instance, on the sample size in case of 2×10^{12} ions/cm^2 (blue line), or on the measurement conditions for the other samples (focusing on the sample surface, et cetera). The data analysis and renormalization of the Raman spectra were done using LabSpec 5 software. The spectra were brought by shifting in y-axis direction to have the same starting point at 90 cm^{-1}. Afterwards spectra were scaled

(multiplied by a constant) until the initial slope of spectra around 90...120 cm^{-1} became as close as possible (fig. 5.14(a)).

The renormalized Raman spectra reveal the same radiation-induced changes in characteristics, i.e. with increasing fluence:

- the intensity of the Raman bands at 131, 141 and 183 cm^{-1} decrease;
- the fluorescent contribution present initially in the spectra of nonirradiated material decreases (for example, intensity under the Raman peaks at 131 and 141 cm^{-1}, decrease of band at 215 cm^{-1});
- the overall background increases steadily.

The absolute intensities of the Raman peaks in the region of PO_4 stretching (988, 1022, 1058 cm^{-1}), bending (485 cm^{-1}) and lattice modes (139, 294 cm^{-1}) were analyzed as a function of ion fluence (fig. 5.15). The data are in a good agreement with the exponential function suggested by the direct-impact amorphization model. Both for the stretching modes shown on fig. 5.15(a) and for the bending/lattice modes represented on fig. 5.15(b), the peak intensities (heights) agree with the fit function slightly better than the peak area. That could be related to the inaccuracy of the peak shape determination.

Table 5.2 reports amorphization cross sections and track radii for 2.1 GeV Au ions in $HoPO_4$ deduced from the fit function according to eq. (5.4). Raman spectroscopy measurements demonstrate macroscopic change of the sample, thus the uncertainty of the track radius is mainly ascribed to ion fluence inaccuracy (∼15%). Details are discussed in section 4.2.

Similar to the case of $NdPO_4$ reported in section 5.2.2, the values of the track radii and damage cross-sections of 2.1 GeV Au ion in $HoPO_4$ obtained from Raman data without spectra renormalization are too low to be considered realistic. Values of track radii close to 5 nm correspond to materials with a similar structure as $HoPO_4$. The situation will be discussed in more details in section 5.2.6.

Visualization of ion tracks in holmium phosphate is represented on the AFM image of $HoPO_4$ crystal irradiated with 2.2 GeV Au ions up to the fluence of 5×10^{10} ions/cm^2. Picture taken using height sensor gives a good resolution of height of the structures, but better visual representation of sample surface was performed in the regime of deflection error (fig. 5.16(b)). Hillocks here could be observed as scattered point-like features among some larger surface defects (scratches and indents). As known for many other materials, swift heavy ions can produce nano-sized hillocks at each impact of the ion projectile [74–76]. Figure 5.16 presents AFM image of the single crystal irradiated to the fluence of 5×10^{10} ions/cm^2. The hillocks shown in fig. 5.16(a) typically have a height around 2 nm. The amount of hillocks corresponds under the experimental uncertainty to the accumulated ion fluence.

Table 5.2: Calculated values for amorphization cross-section and track radii for 2.1 GeV Au ion in $HoPO_4$. Raman measurements were performed with blue laser.

Amorphization cross-section and track radii for 2.1 GeV Au in $HoPO_4$		
Evaluation basis	σ_a ($\times 10^{-14}$cm^2)	R$\pm\Delta$R[a] (nm)
Based on relative peak areas		
Exponential fit[b]	18.1	2.4±0.2
Modified exponential fit[c]	22.9	2.7±0.2
Based specified on peak area after renormalization		
988 cm^{-1}	73.9	4.9±0.3
1058 cm^{-1}	68.4	4.7±0.3
1022+1058 cm^{-1}	68.0	4.7±0.3
485 cm^{-1}	59.4	4.4±0.3
294 cm^{-1}	73.5	4.8±0.4
139 cm^{-1}	69.5	4.7±0.3
Based on specified peak height (intensity) after renormalization		
988 cm^{-1}	75.2	4.9±0.4
1058 cm^{-1}	79.8	5.0±0.4
1022+1058 cm^{-1}	80.6	5.1±0.4
485 cm^{-1}	76.8	4.9±0.4
294 cm^{-1}	73.8	4.9±0.3
139 cm^{-1}	84.4	5.2±0.4

[a] Error for the track radius obtained from Raman spectroscopy data is calculated based on 15% inaccuracy of fluence determination.

[b] Fit function for crystalline fraction: $f_{cr} = \exp(-\pi R^2 \Phi)$ according to eq. (5.2).

[c] Fit function for crystalline fraction: $f_{cr} = f_0 \cdot \exp(-\pi R^2 \Phi)$ according to eq. (5.4).

5.2.4 Broadening and shift of Raman peaks as a function of ion fluence

This section is devoted to the analysis of radiation-induced changes in the shifts and width of Raman peaks for $NdPO_4$ and $HoPO_4$. On table 5.3 the positions of different Raman peaks are reported for both $NdPO_4$ and $HoPO_4$ with the measurements performed using a He-Ne laser with excitation wavelength of 632.82 nm. Results are reported for virgin crystals and samples irradiated with 2.1 GeV Au ions at the lowest and highest fluences available for both materials, namely 5×10^{11} and 10^{13} ions/cm^2. In some cases peaks disappear at high fluences. Broad amorphous humps that appear due to beam-induced amorphization (figs. 5.8(a) and 5.13(a)) are denoted as "Am." in table 5.3. We can see that for both materials the position of some of the Raman bands change with irradiation. The sign of this change, however, is sometimes different at 5×10^{11} ions/cm^2 compared to 1×10^{13} ions/cm^2. Peaks in the regions of stretching, bending and lattice modes show slightly different trends.

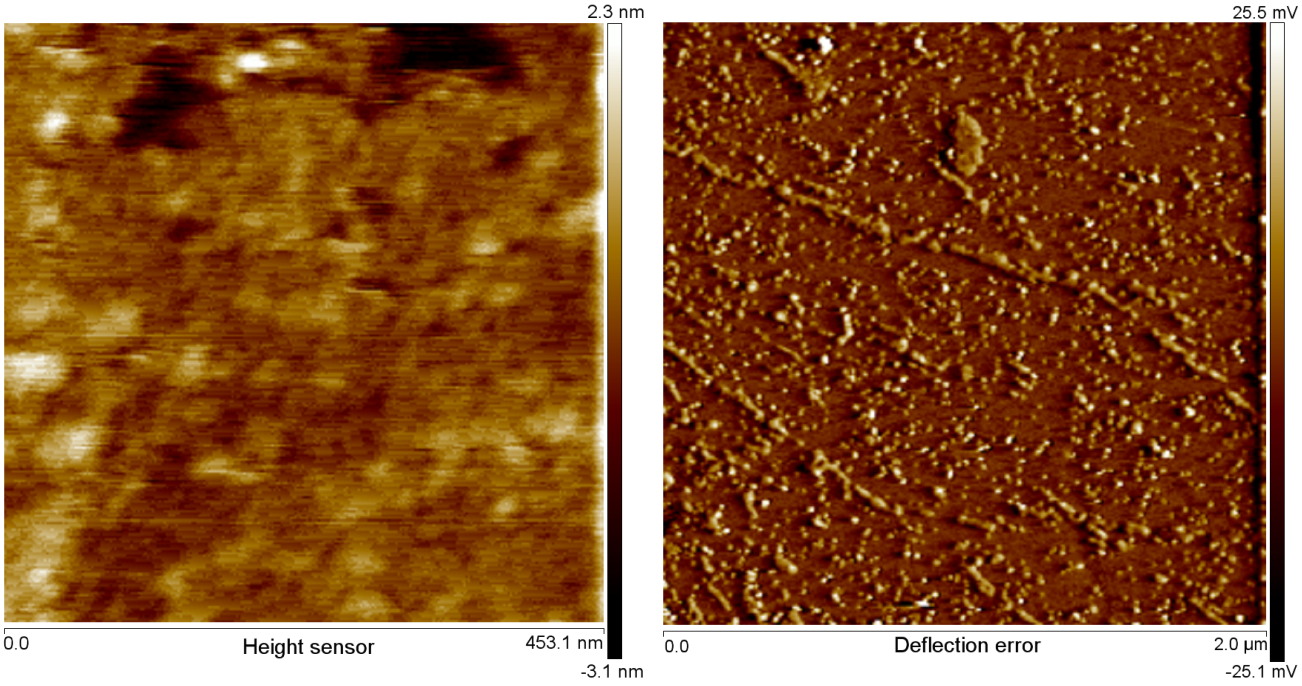

(a) (b)

Figure 5.16: AFM image of hillocks in $HoPO_4$ produced by the irradiation with 2.2 GeV Au ions in regime of: a) Height sensor (height determination of different surface features); b) Deflection error (better visualization of surface feature shape).

Figure 5.17 represents the shift of various Raman peaks as a function of fluence for $NdPO_4$ single crystal irradiated with 2.1 GeV Au ions. The results are reported for bands in the region of stretching, bending and lattice modes:

- At the first fluence step of 5×10^{11} ions/cm^2 all peaks in the region of stretching modes (fig. 5.17(a)) shift by 1.5-2 cm^{-1} towards lower wavenumbers. For higher fluences the peaks start to shift consistently to larger wavenumbers, pass the initial Raman peak position at the fluence of 5×10^{12} ions/cm^2 and shift even further at the last fluence step of 10^{13} ions/cm^2. Due to limited number of sample crystals it was not possible to perform irradiations at fluences below 5×10^{11} ions/cm^2 to test behavior of peak shift at low fluences.

- Peaks at the region of the bending modes of PO_4 tetrahedron do not have any consistent tendency within the fluence series. The peaks initially slightly shift to lower wavenumbers (fig. 5.17(b)), reaching minimum at 5×10^{12} ions/cm^2 and then inverse shift direction.

- Peaks in the region of lattice modes (fig. 5.17(c)) possess a similar trend as the symmetric stretching modes. The peaks (except of peak at 163 cm^{-1} that holds its position) shift to the lower wavenumbers at the first fluence step and consistently shift in the other direction at higher fluences.

Table 5.3: Raman shift of different bands in $NdPO_4$ and $HoPO_4$ irradiated by 2.1 GeV Au ions (frequency 50 Hz, pulse length 5 ms). Radiation induced broad (Gaussian shape) peaks are labeled as "Am.". Raman shift positions are provided for nonirradiated crystals and for the fluences of 5×10^{11} and 1×10^{13} ions/cm^2. The measurements were done using red laser for $NdPO_4$ and blue laser for $HoPO_4$.

$NdPO_4$				$HoPO_4$			
Assignment	Virgin	5×10^{11} ions/cm^2	1×10^{13} ions/cm^2	Assignment	Virgin	5×10^{11} ions/cm^2	1×10^{13} ions/cm^2
B_g	1079			B_{1g}	1056	1054	1055
A_g	1061	1059	1062	Am.			1040
Am.			1055	E_g	1020	1018	1021
Am.			1034	A_{1g}	1000	998	1001
B_g	1031	1027		Am.			970
A_g	996	994	995	B_{1g}	655	653	
A_g	976	974	976	E_g	577	576	
Am.			960	A_{1g}	485	485	486
A_g,B_g	625	623	622	B_{2g}	330		300
B_g	593			E_g(R)	297	294	
A_g	574	572	573	B_{1g}(T)	183		
A_g	538	537	538	E_g(T)	141	139	140
A_g	470	469	469	B_{1g}(T)	131	130	
A_g	420	418	418				
B_g	399						
A_g	289	287					
A_g	263	259					
B_g	237						
B_g	226	224	225				
B_g,A_g	180	177					
B_g,A_g	163	162	162				
B_g	154						
A_g,B_g	133	131	131				
A_g	122	121	121				
B_g	105	104					

Figure 5.18 reports the shift of several Raman bands of $HoPO_4$ single crystal irradiated with 2.1 GeV Au ions. The results are reported for the stretching modes due to difficulties of reliable peak position determination for the peaks at the lower wavenumbers where they severely interfere with the luminescence. The results show a very similar behavior to $NdPO_4$, but the shift of peak positions changes the sign at the fluence step of 10^{12} ions/cm^2.

Such a behavior of Raman peak shifts is unusual. Manny cases reported in literature when Raman peak shift being successfully used for analysis of metamictization (disorder) in naturally irradiated minerals. In that case the Raman peaks consistently shift to lower wavenumbers and the experimental data (shifts vs fluence/dose) fits an exponential law. For $NdPO_4$ and $HoPO_4$ the shift to lower values was obtained only at very first fluence step(s) and for subsequent higher

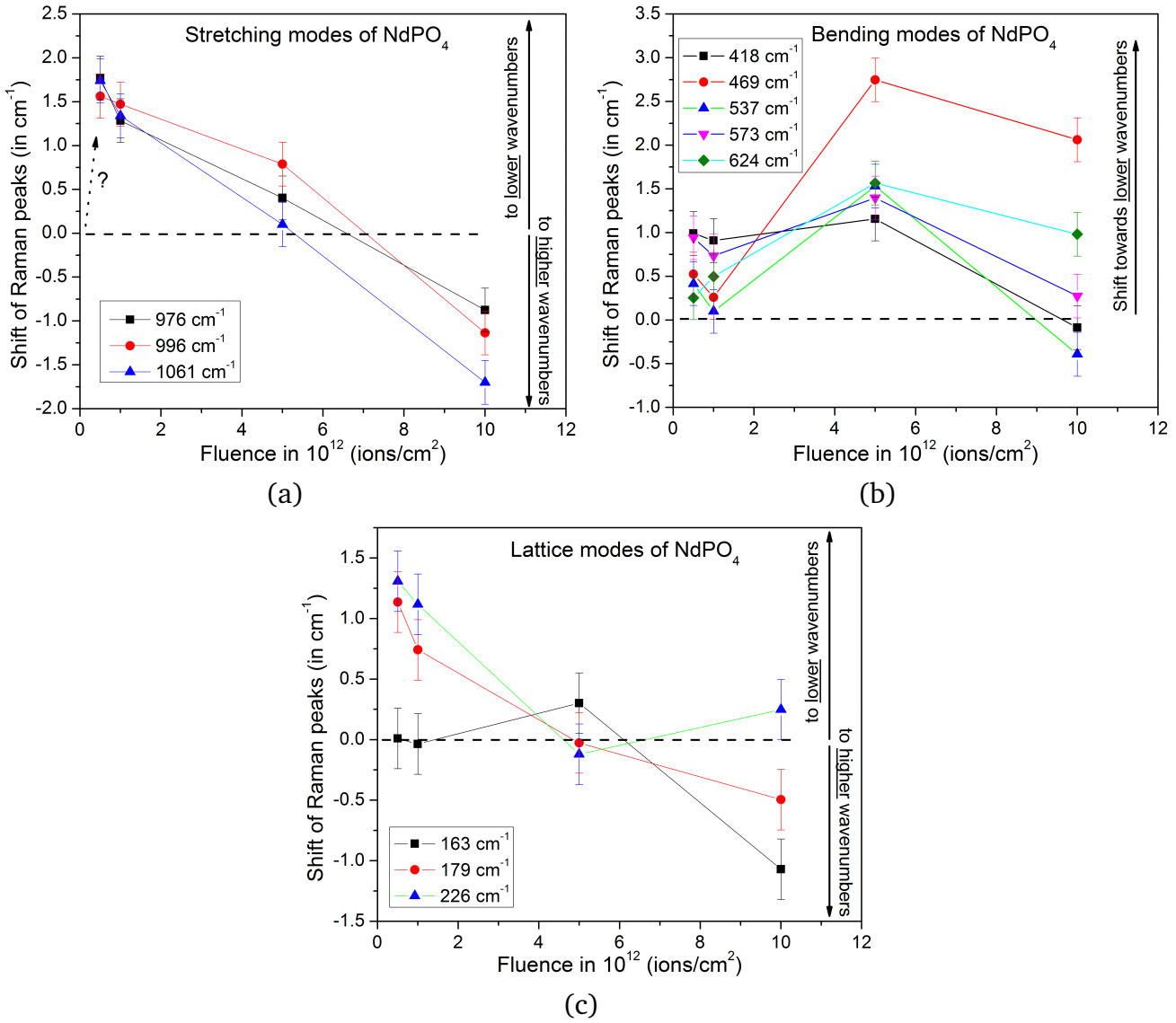

Figure 5.17: Shift of Raman peaks as a function of fluence for virgin and irradiated $NdPO_4$ for: a) stretching; b) bending; c) lattice modes. The dashed line indicates the band position in the virgin crystal. A positive (negative) shift denotes a shift to lower (higher) wavenumbers. Irradiation was done by 2.1 GeV Au ions. Raman spectra were measured using He-Ne laser with λ=632.82 nm.

fluences we clearly see the reverse trend (for the $NdPO_4$ on fig. 5.17 , for $HoPO_4$ on fig. 5.18). The position of Raman bands corresponds to the average vibration energy of a particular structural unit (here $(PO_4)^{3-}$ tetrahedron) and a band shift reflects changes in the P-O distance. A shift to lower wavenumbers corresponds to a decrease in energy of a particular vibration and an increase in distance between the phosphorus and oxygen atoms (reverse argument applies for a peak shift towards higher wavenumbers). The initial shift of Raman bands at 5×10^{11} ions/cm^2 to lower wavenumbers could be caused by swelling or due to the production of point defects (e.g. vacancies, increasing the mean distances between the phosphorus and oxygen). Last argument is often made in the literature and such behavior of Raman peaks is well studied in zircon [77–79] and reported for Ce-monazite [59]. The shift to higher wavenumbers at larger fluences

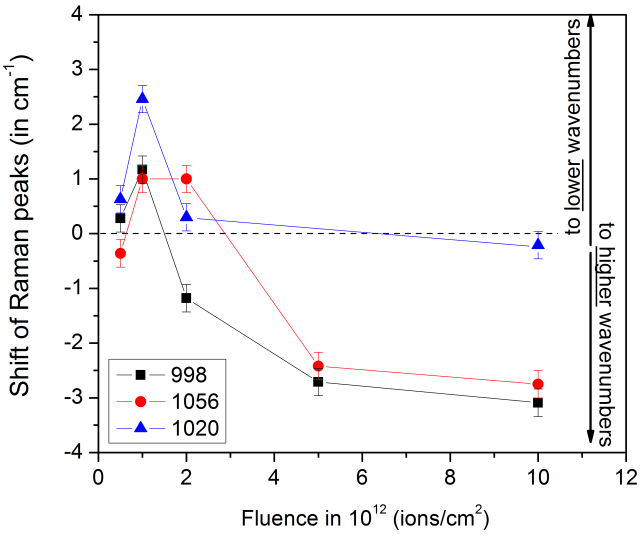

Figure 5.18: Shift of Raman peaks as a function of fluence for virgin and irradiated $HoPO_4$ for $(PO_4)^{3-}$ stretching modes. The dashed line indicates the band position in the virgin crystal. A positive (negative) shift denotes a shift to lower (higher) wavenumbers. Irradiation was done by 2.1 GeV Au ions. Raman spectra were measured using Cobalt laser with λ=473.05 nm.

could be an indication that the remaining crystalline fraction of the sample experiences stress from expanded amorphous material and with the increase of the ion fluence the amorphous fraction rises affecting remaining crystalline part to a larger extend.

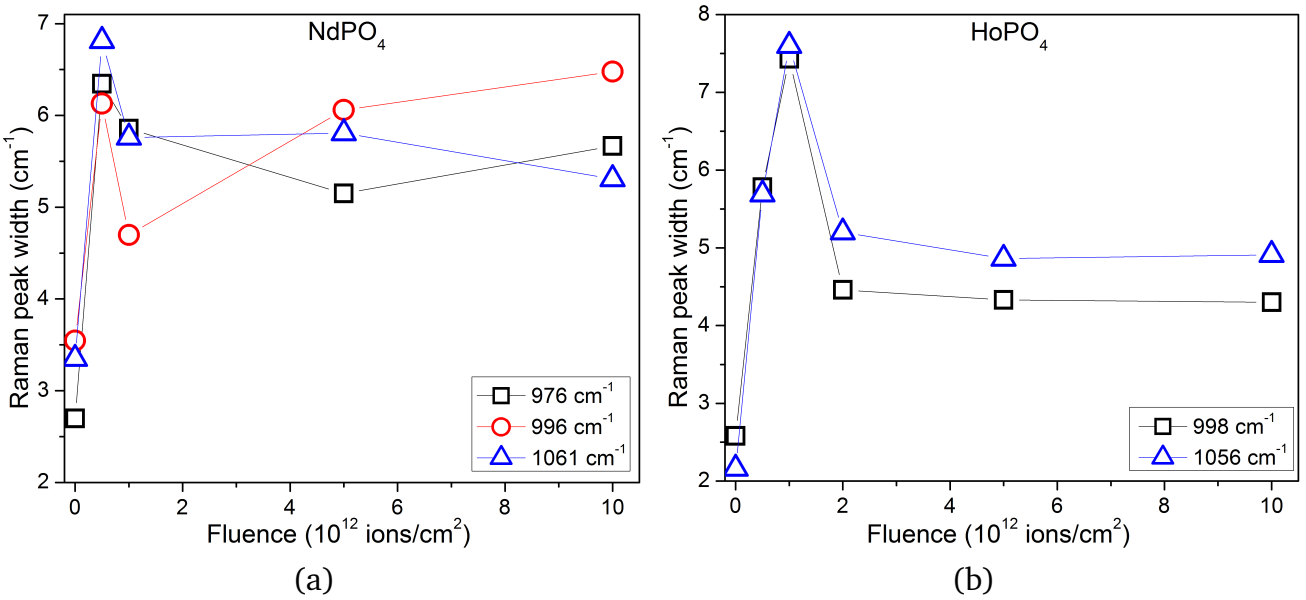

Figure 5.19: Raman peak width of symmetric and antisymmetric $(PO_4)^{3-}$ stretching modes as a function of 2.1 GeV Au ion fluence for the crystals of: a) $NdPO_4$; b) $HoPO_4$. Error bars are smaller or equal to the data point size.

The width of different Raman peaks from the stretching modes of virgin and irradiated $NdPO_4$ are shown on fig. 5.19(a). Similar to the case of peak shifts, no consistent trend depending on the ion fluence could be observed. At the very first irradiation step of 5×10^{11} ions/cm^2, a signifi-

cant jump in width appears, while at higher fluence the tendency changes direction and is somewhat chaotic. The width of the peak at 996 cm^{-1} increases after the fluence of 10^{12} ions/cm^2. It is attributed to the very small intensity of this band and quickly vanishes in the background or starts to be harder distinguishable from it. For the peaks of 976 cm^{-1} and 1061 cm^{-1} (symmetric and antisymmetric stretching modes of $(PO_4)^{3-}$ tetrahedron, respectively) after 10^{12} ions/cm^2 values go down with increasing fluence.

A swing in the trend of fluence dependence for the Raman peak width and shifts could be explained assuming the existence of defects or a stress halo around the amorphous tracks. A few examples of the material being affected within a larger area apart of the ion track region are reported in the literature. Partial or imperfect recrystallization of the region around the ion track can lead to the appearance of a defect area at the border between the amorphous ion track and surrounding crystalline matrix. In the $Gd_2Ti_2O_7$ pyrochlore, a disordered defect-fluorite shell, is observed around the amorphous ion track [27, 28, 43]. In α-quartz a crystalline defected halo is shown to be present around the amorphous track core [80]. Furthermore, the density variations that appear in the ion track region could lead to the creation of significant stresses in the material. As an example, the core-shell structure with a lower density core and high density shell regions of the ion tracks has been reported for the swift heavy ion tracks in the silicon oxynitride films [81]. A similar radial variation of the density and associated stress distribution was reported for the Al_2O_3 [82]. The appearance of defected region around the amorphous ion track in $NdPO_4$ and $HoPO_4$ can be explained by observations of the Raman peak shift and position dependences reported in this section.

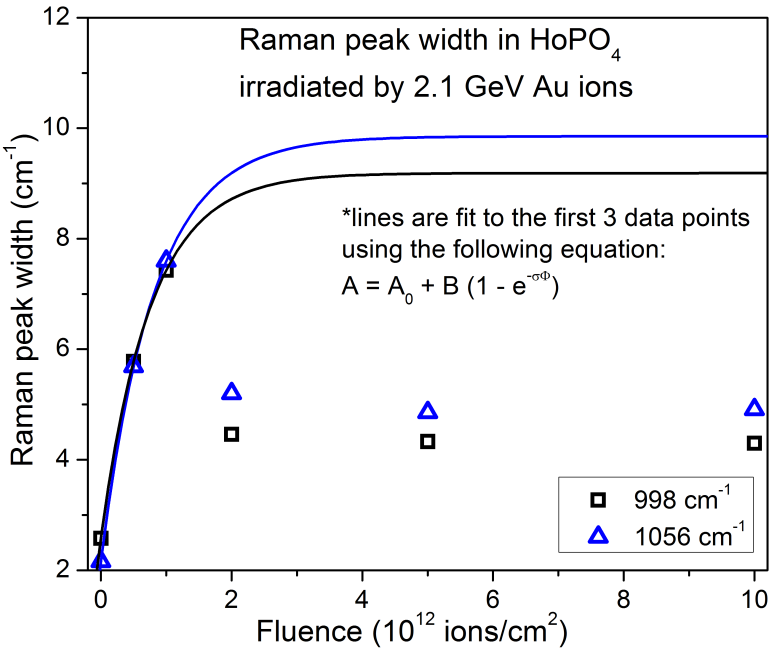

Figure 5.20: Fit of Raman data for the width of the $(PO_4)^{3-}$ stretching modes for $HoPO_4$ irradiated with 2.1 GeV Au ions.

Assuming that the defected halo causes the increase in the Raman peak width, we can apply the same logic used for the analysis of the amorphous ion track size. The analysis of Raman peaks was done only for the sharp intense peaks, and does not take into account the amorphized material. That means, we can expect the same exponential dependence of the Raman peak width to the ion fluence that should provide values for track radii larger than the radii of the amorphous tracks. Figure 5.20 represents the fluence dependence of Raman peak width for $HoPO_4$ and the fit to the exponential law for the first three experimental points. The equation used for the fit is:

$$A = A_0 + B(1 - \exp(-\sigma_{\text{def}} \cdot \Phi)), \tag{5.5}$$

where A_0 represents the value of Raman peak width for nonirradiated material, B is fitting parameter that indicates the radiation induced increase of the peak width, $\sigma_{\text{def}} = \pi\ \text{R}_{\text{def}}^2$ is a cross-section for the defect halo formation, R_{def} is the track radius of the defect halo. The resulting fitting equations were: y = 2.16 + 7.69 (1 - exp (-1.228x)) and y = 2.58 + 6.61 (1 - exp (-1.325x)) for symmetric and antisymmetric stretching modes respectively. The values for R_{def} obtained from fit correspond to: 6.5 nm for the peak of symmetric stretching mode at 998 cm^{-1}, and 6.3 nm for the peak of antisymmetric stretching mode at 1056 cm^{-1}. It should be taken into account that similar considerations could be applied for the stress and defect halo and explicitly distinguishing between these two could not be done based on the existing experimental data.

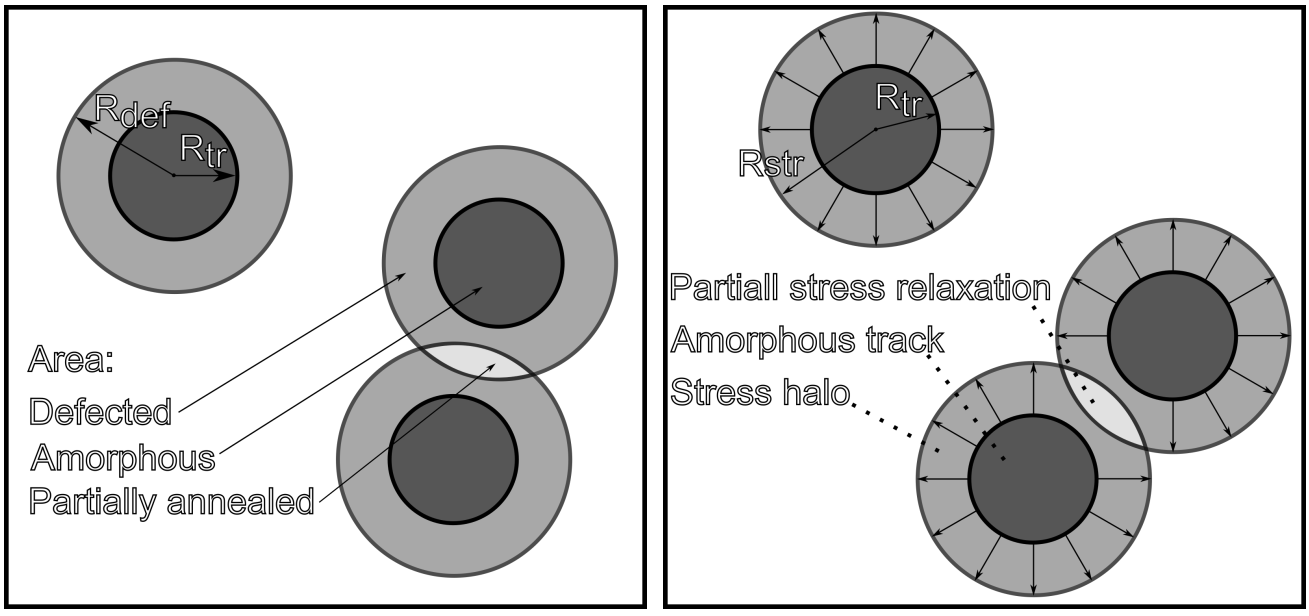

(a) (b)

Figure 5.21: Schematic representation of the defect and stress halo.

Putting together the values obtained for the amorphous track radii of 2.1 GeV Au in $HoPO_4$ equal to 5.0±0.3 nm (analysis in section 5.2.3) and values for the radius of the defected/stress halo of 6.4±0.1 nm, the resulting picture of the material response to swift heavy ion impacts could be illustrated by fig. 5.21.

The electronic energy loss in the rare earth phosphates is known to induce recrystallization at values of electronic energy loss beyond the critical value required to trigger amorphization [83, 84]. The decrease of the Raman peak width at fluences larger than 10^{12} ions/cm^2 represented in fig. 5.20 could come from the partial defect annealing in the overlapping halo regions of different ion tracks. In the stress halo interpretation, the two overlapping tracks can create a path for the stress relaxation. This would explain the Raman peak width for both established at the value about 4-5 cm^{-1} at the higher fluences. Data concerning the stress halo formation and evaluation of stresses around the ion tracks in rare earth phosphates is absent in literature.

5.2.5 Raman spectroscopy measurements along ion tracks

In section 5.2.1 (fig. 5.4) calculations of the electronic energy deposition of 2.1 GeV ^{197}Au ions along their path in $NdPO_4$ and $HoPO_4$ crystals is shown. Measurements from the side (see section 4.2) allow monitoring changes in the Raman spectra along the ion track. This section presents such measurements along the ion tracks and correlates them to visual changes in the crystals of both compounds.

Figure 5.22 presents a series of Raman spectra of a $NdPO_4$ single crystal irradiated with 2.1 GeV Au ions up to a fluence of 10^{13} ions/cm^2. The Raman spectra were taken on the crystal cross-section normal to the irradiated surface i.e. along the ion trajectories. Position “0” corresponds to the sample surface. The ion range according to the SRIM code is marked by an arrow. The strongly modified Raman spectra suggest complete sample amorphization up to a depth that is close to the length of the ion tracks. Close to the end of range few Raman spectra (measurements between 45 and 60 μm on fig. 5.22) show slightly different band intensities. It is assumed that this effect is related to cracks in the sample that typically appear close to the amorphous-crystalline interface (fig. 5.24(a)). Beyond the ion range, the intensities of the main bands quickly increase up to the values that correspond to the virgin crystalline material. Beyond the ion penetration depth, the amorphous background also rapidly vanishes and we see no effect of any structural changes.

The corresponding measurement for single-crystaline $HoPO_4$ irradiated by Au ions up to 10^{13} ions/cm^2 shows the same behavior (fig. 5.23). Within the ion range luminescence is nearly absent, spectra contain no sharp peaks, but exhibit the amorphous background which is present in the spectra. Close to the end of the ion range, the intensities of sharp Raman peaks rapidly increase and the spectra quickly transform to the one that corresponds to the unirra-

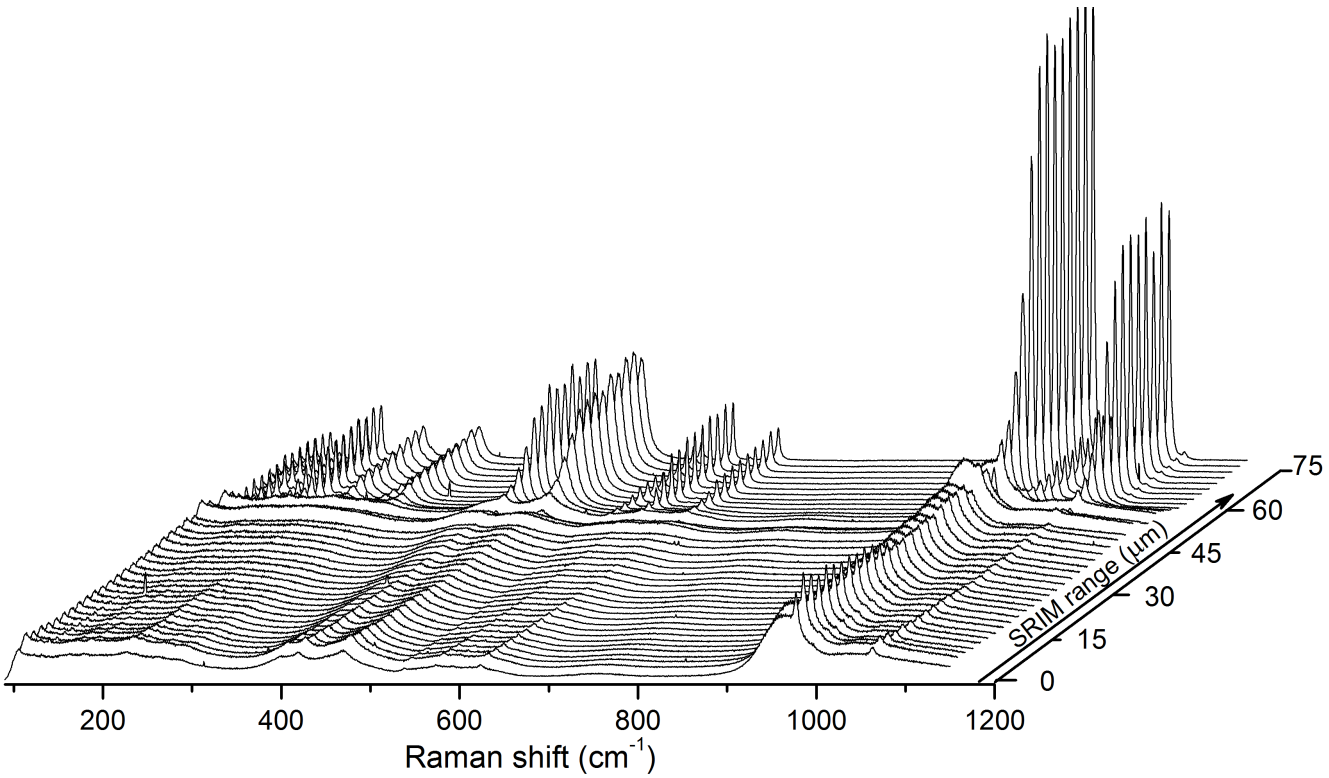

Figure 5.22: Raman spectroscopy measurements along ion tracks of $NdPO_4$ crystal irradiated by 2.1 GeV Au ion at a fluence of 1×10^{13} ions/cm^2. The arrow along the y-axis represents the ion range as calculated with the SRIM-2010 code.

diated sample material. Figure 5.24 shows the corresponding micrographs of the $HoPO_4$ and $NdPO_4$ crystals indicating the line along the Raman spectra were recorded.

When comparing scans along tracks in $NdPO_4$ and $HoPO_4$ the following differences are noticed: the intensity of the Raman signal produced by the amorphous material is higher in $NdPO_4$, the transition from the "amorphous" to the "crystalline" spectrum is more sudden regarding depth and, finally, the SRIM range calculation seems to correlate better with Raman measurements in the case of $NdPO_4$. The range seems to be overestimated for $HoPO_4$. This effect, however, is related to the sample size. In the case of $NdPO_4$, the irradiated sample fractured from the initially thicker irradiated crystal and thus was significantly thinner than the $HoPO_4$ sample. Therefore, for $HoPO_4$ the intensity of Raman signal arising from the nonirradiated volume beyond the ion track was much higher compare to the low intensity amorphous signal from the amorphized sample material. In addition, a slight sample misalignment affects the precision of depth assignment. In the transition region between 45 and 60 μm a small tilt of the sample smears out the Raman signal by measuring regions within and beyond the ion range.

In the section 5.1 I have mentioned that change of sample color that could be typically observed for irradiated crystals is below the range calculated with the SRIM code. Figure 5.24 presents the optical micrographs (image obtained before Raman measurements) and corresponding electronic and nuclear energy loss for both materials calculated with the SRIM-2010

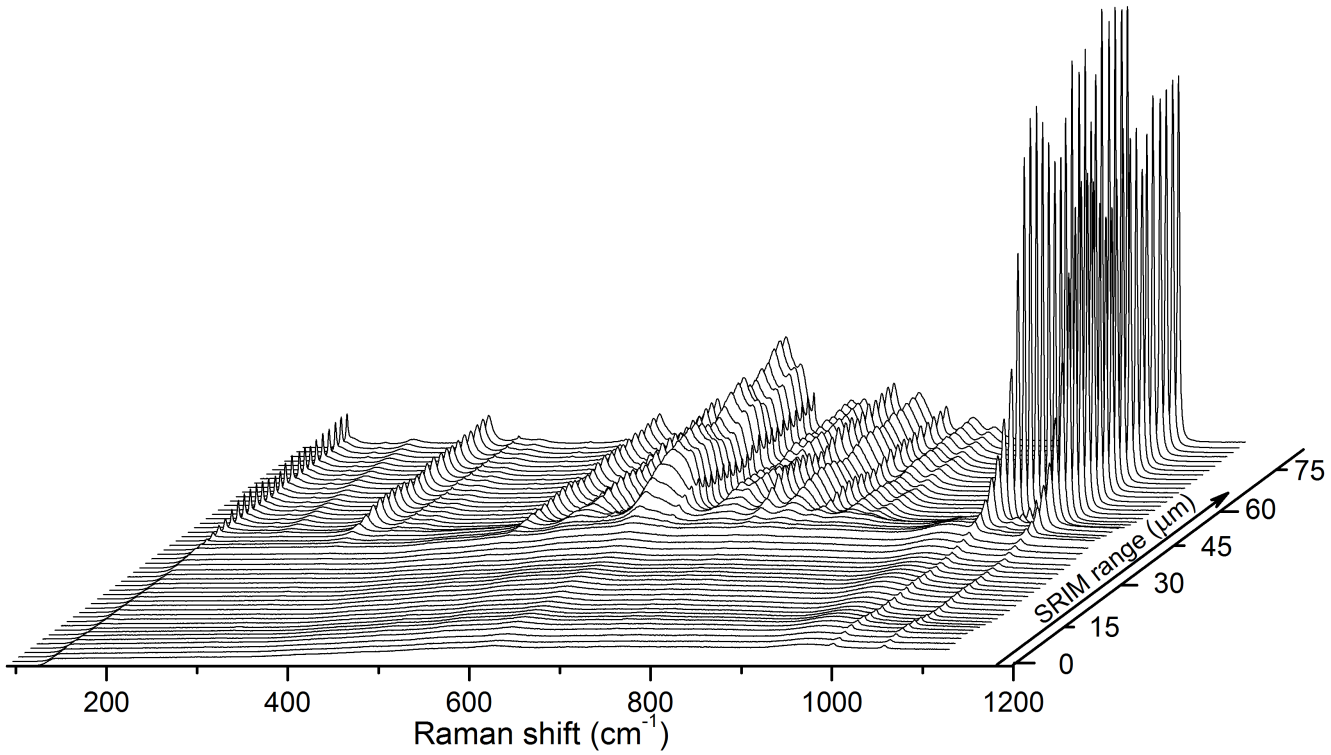

Figure 5.23: Raman spectroscopy measurements along ion tracks of $HoPO_4$ crystal irradiated by 2.1 GeV Au ion up to a fluence of 1×10^{13} ions/cm^2. The arrow along the y-axis represents the ion range as calculated with the SRIM-2010 code.

code. The dark sample part extends up to 55-57 μm, while the calculated ion range in both materials is about 65-67 μm. The sharper color transition in the case of $NdPO_4$ could be related to the larger sample size. The discrepancy between the SRIM range and depth of optical changes is either due to an overestimation of the SRIM calculation and/or due to a energy loss required for the production of optical effects.

$NdPO_4$ is almost completely amorphized at a Au ion fluence of 10^{13} ions/cm^2. The amorphous fractions based on the relative area of the remaining crystalline peak yield more than 95%. However, when analyzing the Raman measurement at the larger depth, a decrease of small crystalline peak between 40 and 50 μm is noticed. The decrease of intensity of sharp Raman peaks is associated with increasing amorphization. The amorphous fraction as a function of crystal depth follows the electronic energy loss as shown on fig. 5.25. This change is well illustrated by few Raman measurements at a depth of 7, 25, 45 and 60 μm.

The possible explanations for the decrease in the intensity of the small sharp crystalline Raman peak could be:

- So-called velocity effect, that consists in the increase of track radius at the same value of energy loss when the speed of impacting ion deceases;

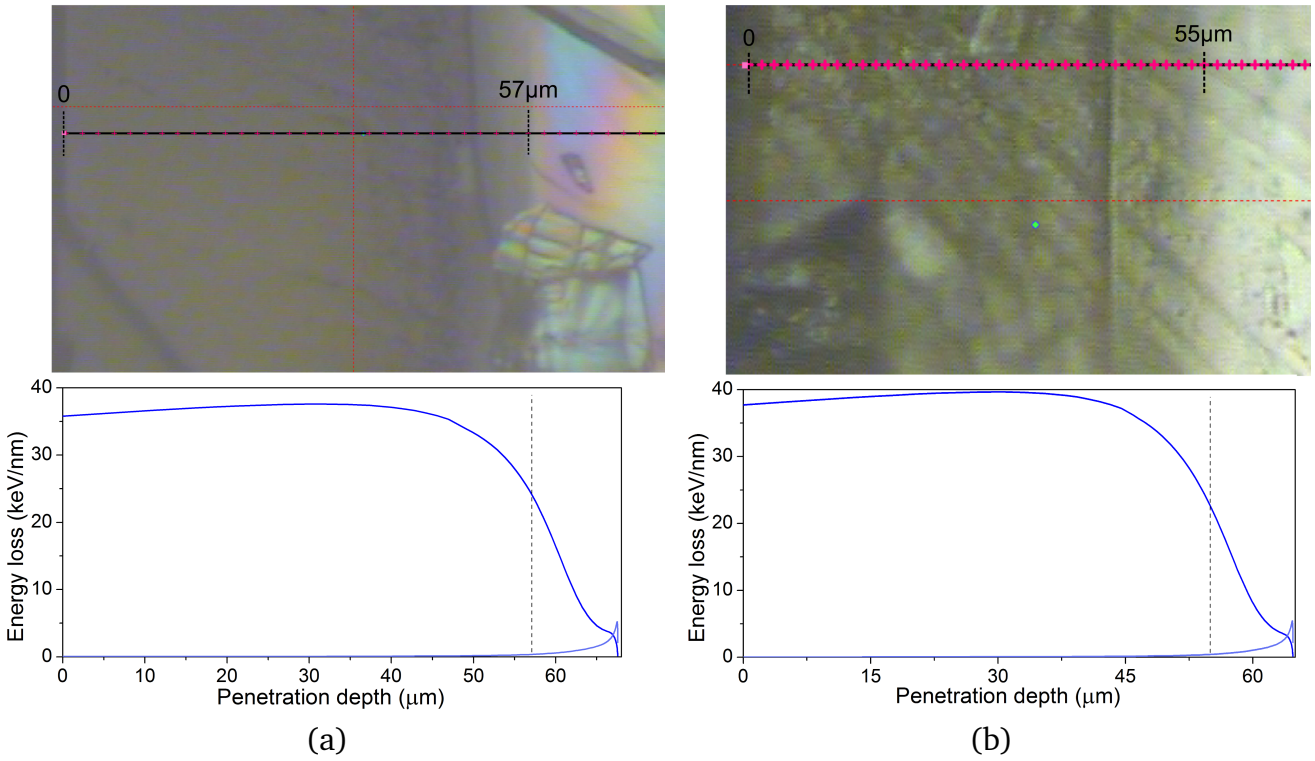

Figure 5.24: Optical micrograph and SRIM calculation of electronic energy loss as a function of penetration depth of 2.1 GeV Au ions for: a) $NdPO_4$; b) $HoPO_4$. "0" is close to the sample surface, dashed line indicates end of visible changes in the sample.

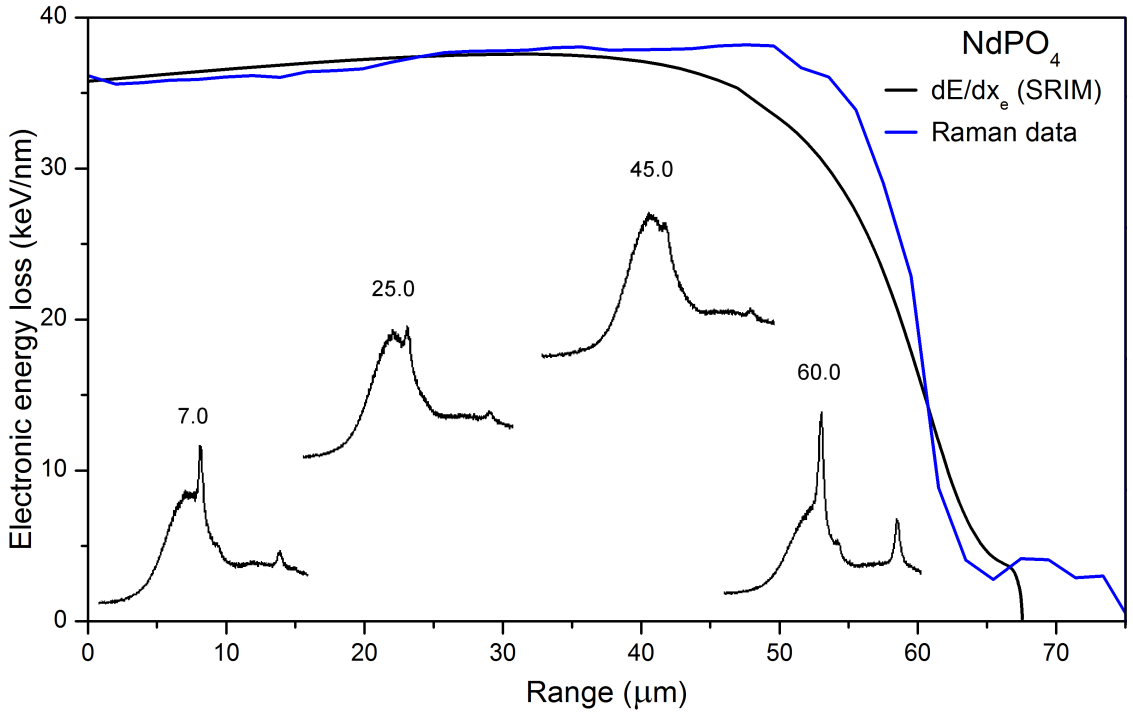

Figure 5.25: Remaining intensity of symmetric stretching mode in Raman spectrum of $NdPO_4$ irradiated with 2.1 GeV Au ion up to the fluence of 10^{13} ions/cm^2 vs SRIM-2010 calculation of electronic energy loss. Small inserts show Raman spectra at particular depth.

- In agreement with many other materials ([43]), the track radius scales with the electronic energy loss, what is reflected in slight variation of track radius (and amorphization cross-section) at different depth.

Partially this observation is supported by the SAXS measurements (table 5.1 contains results for $NdPO_4$ track radius variation, so called, polydispersity) that suggested variation of track radius around 0.5 nm.

The Raman spectra along the ion trajectories of a $HoPO_4$ single crystal irradiated with 2.1 GeV Au ions up to a fluence of 5×10^{11} ions/cm^2 is shown on fig. 5.26. At this lowest fluence the decrease in Raman peak intensities is rather modest. Shift of positions for the Raman bands in irradiated crystal relative to the virgin material (details are reported in the section 5.2.4) could be observed here as well (fig. 5.26).

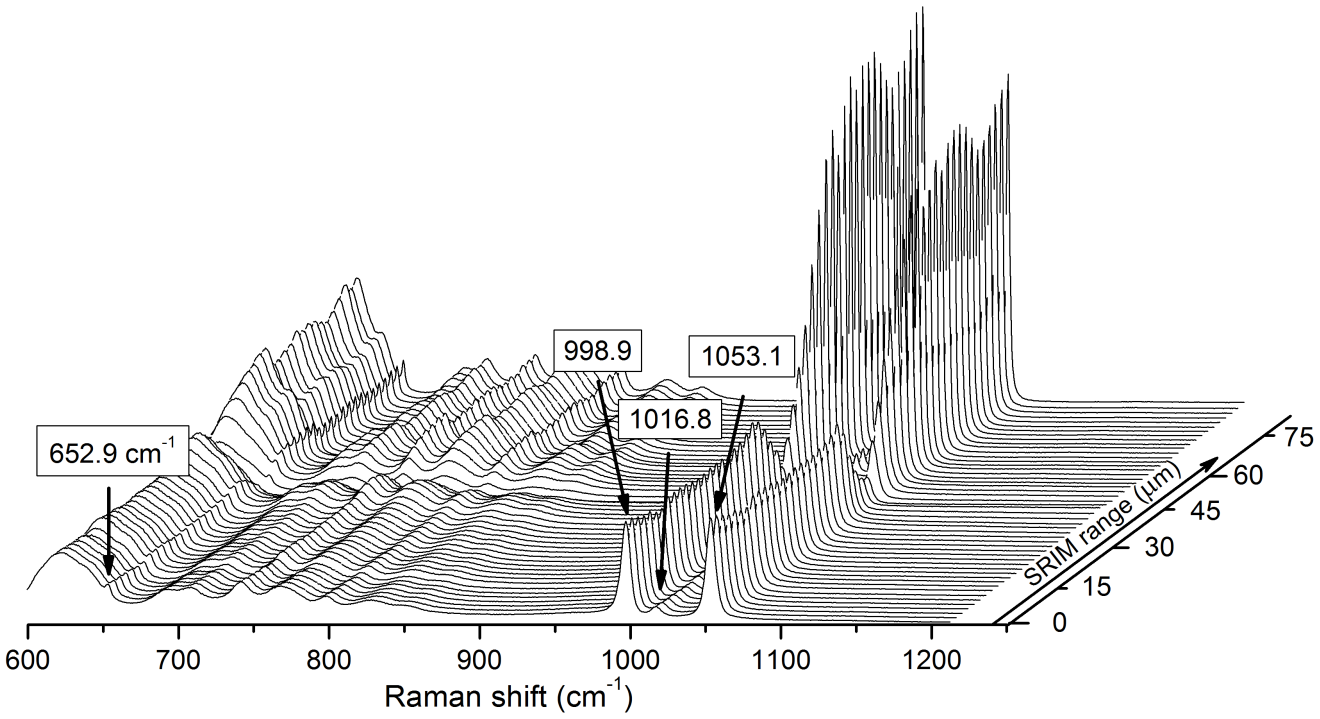

Figure 5.26: Raman spectroscopy measurements along ion tracks of $HoPO_4$ crystal irradiated by 2.1 GeV Au ion up to a fluence of 5×10^{11} ions/cm^2. The arrow along the y-axis represents the ion range as calculated with the SRIM-2010 code.

Scan along the ion path gives an opportunity to see the shift of Raman peaks as a function of depth. Figure 5.27 shows the same experimental data reported on fig. 5.26 representing it as a 2-dimensional scan. The X-axis corresponds to the Raman peak positions and Y-axis resembles position of the measurement point. The Y-axis reflects positions that were used by the Raman device, so it needs to be stated that value of Y-axis of -35 μm matches sample surface. Intensity of yellow color reflects the Raman signal intensity, while smearing out of the lines on 2D scan indicates Raman peak broadening. On the fig. 5.27(b) we can see three peaks that are present

in the region of PO_4 stretching in Raman spectra of $HoPO_4$. Some signal intensity indicating amorphous background is observed up to the position of about 20 μm (what corresponds to ion depth of 55 μm). In the region of bending modes small Raman peak is accompanied by large fluorescent contribution (fig. 5.27(a)). For all the Raman peaks in this region we can observe similar trend, where broadened Raman peaks of damaged material retain their positions up to the depth of approximately 45 μm (10 μm on the 2D scan). Between 45 and 55 μm (10-20 μm on the 2D scan) consecutive shift of all Raman peaks brings them to the positions typical for virgin $HoPO_4$ crystals.

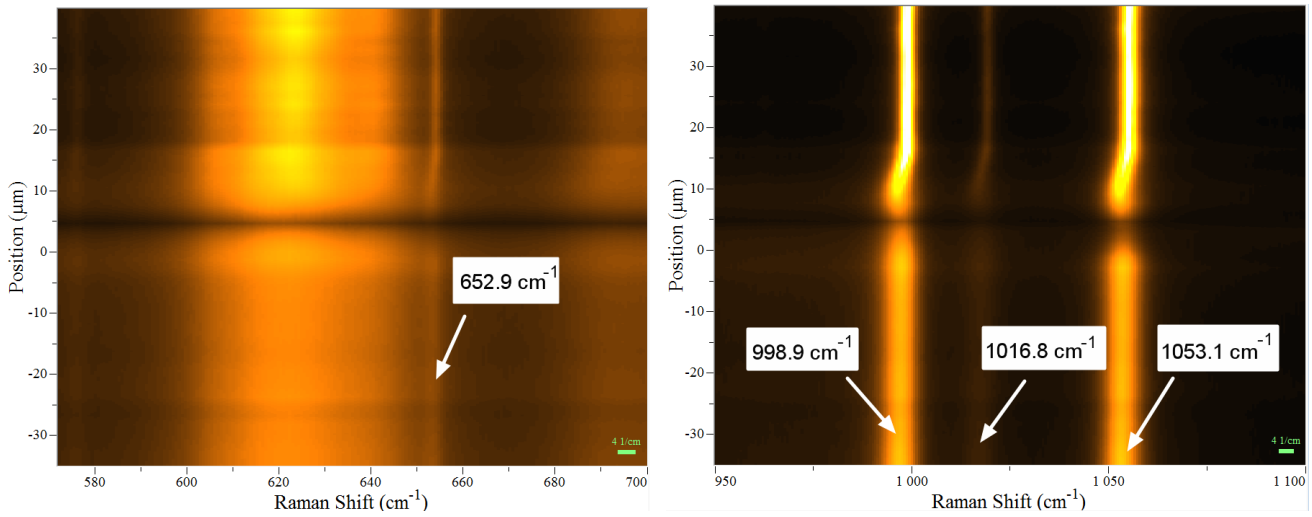

Figure 5.27: 2-dimensional representation of depth scan in $HoPO_4$ irradiated by 2.1 GeV Au ions at 5×10^{11} ions/cm^2: a) region of bending modes; b) region of stretching modes.

The line scan shown on fig. 5.27 suggests a gradual decrease of the amorphous background and recovery of peak positions close to the end of the ion range. Again we can notice here that the range of 55 μm for 2.1 GeV ions is shorter than the value suggested by SRIM calculation (64 μm).

5.2.6 Discussion and conclusions

Previous sections present the analysis of radiation damage in single crystals: monoclinic neodymium ($NdPO_4$) and tetragonal holmium phosphate ($HoPO_4$). Irradiations were performed with 2.1 GeV Au ions with fluences varying from 5×10^{11} ions/cm^2 up to 5×10^{13} ions/cm^2 for $HoPO_4$ and 5×10^{11} ions/cm^2 up to 10^{13} ions/cm^2 in case of $NdPO_4$. The irradiations were provided perpendicular to the sample surface. Many samples often broke and fractured as a result of irradiation. Raman spectroscopy measurements were taken at the irradiated surface as well as in cross section perpendicular to the direction of incoming ions. SEM images illustrated the radiation induced changes of macroscopic properties in $PrPO_4$. The irradiated specimens

changed the color and transparency in the irradiated layer. Severe fracturing of the crystals occurred especially at the region between amorphous and crystalline material close to the end of ion range. The embrittlement of the samples resulted from the accumulation of stresses in particular on the crystalline/amorphous interface. The SEM images clearly illustrate the volume expansion of the irradiated layer (swelling) and cracking within and beyond irradiated layer.

Raman spectroscopy measurements for both irradiated $NdPO_4$ and $HoPO_4$ show severe changes in the spectra. All sharp intense Raman peaks that were present in the virgin crystals gradually decrease in intensities and vanish with the accumulation of ion fluence. Tiny remains of symmetric and antisymmetric stretching modes (most intense peaks in the virgin spectra) were observed for both compounds at a fluence of 10^{13} ions/cm^2. The Raman spectrum of the $HoPO_4$ crystal irradiated at 5×10^{13} ions/cm^2 contains no traces of any Raman peak present in the initial spectrum. The decrease of all Raman peak intensities is accompanied in both materials by the appearance of broad humps (around 960 cm^{-1}) at the region of the stretching modes. The appearance of similar broad bands have been repeatedly reported for various compounds in the literature. The damage production in the materials is due to the accumulation of ion tracks. Ion tracks are extended amorphized cylinders with a diameter of about 5 nanometers formed along the path of each ion. The accumulation of ion tracks gradually increases the volume of the amorphous material fraction.

The first approach used for the calculation of track radii consisted in the calculation of the amorphous material fraction based on the relative peak intensities or area. The intensity ratio of the sharp crystalline peak of symmetric stretching mode and the amorphous hump were used to characterize a degree of amorphization. This approach to analyze Raman data did not match predictions from the direct-impact amorphization model and obviously significantly underestimated values of track radii. An alternative way to analyze Raman data was performed by renormalization of Raman spectra. All measured data was modified to have the same or very close increment of Raman signal in the spectral area close to zero. That procedure supposed that in the end all the spectra will be renormalized to the Raman filter (what is a property of an equipment). From the rescaled spectra the absolute intensities of Raman peaks assigned to the crystalline material were deduced and allowed me to calculate degree of amorphization. In this case, the analysis provided values that match well with the data for similar compounds from the literature. For both $NdPO_4$ and $HoPO_4$ the track radius was found to be close: 5.0±0.4 nm for $NdPO_4$, 5.0±0.3 nm for $HoPO_4$. Appearance of ion tracks I have illustrated by additional experimental techniques: TEM for $NdPO_4$ and AFM for $HoPO_4$.

The analysis of the Raman peak width and shift in the spectra of both compounds showed an unusual behavior. For $NdPO_4$ at the first fluence step of 5×10^{11} ions/cm^2 all Raman peaks shift towards lower wavenumber. With further increase of fluence, the peaks start to shift towards lager wavenumbers. For $HoPO_4$ trend changes direction a little bit later at the fluence of 10^{12} ions/cm^2. Peaks that represent the stretching of $(PO_4)^{3-}$ tetrahedron surpass the value of

Raman peak position for the virgin material at a fluence of 5×10^{12} ions/cm^2 for both compounds and continue to shift further at the following irradiation step. Raman peak width also indicates change in the trend at the same fluences. At the very first irradiation step for $NdPO_4$ (for the first two for $HoPO_4$) width of Raman bands increases in comparison to nonirradiated material. With the subsequent irradiations at the fluences larger than 10^{12} ions/cm^2 and 2×10^{11} ions/cm^2 for $HoPO_4$ I observed decrease of peak width for both symmetric and antisymmetric stretching modes. Fluence dependence of Raman peak width for $HoPO_4$ allowed to make an assumption about the existence of defect/stress halo around the amorphous tracks. The exponential law fit to the experimental data for the Raman peak width suggested defect halo radius of 6.4±0.1 nm for $HoPO_4$. The decrease of Raman peak width at the higher fluences was interpret by the partial defect annealing in the overlapping halos of impacting ion tracks.

Measurements of samples with cracked facets allowed Raman spectra recording as a function of ion penetration depth. Raman spectra were found to correlate with the energy deposition suggested by the SRIM computational code, however, the range of ion penetration from the SRIM calculation was found to be on ∼15% larger than the depth of modified sample material. Same discrepancy was found for the optical observations. Analysis of Raman spectra along the ion path at a fluence step of 1×10^{13} ions/cm^2, what is close to complete amorphization, showed slight increase of damage production inside of sample. That tendency of slightly more effective amorphization along the ion path coincided with calculated depth profile of energy deposition and is most likely accompanied by the velocity effect. Velocity effect assumes larger contribution to the material amorphization with the decrease of ion energy due to increased time of ion-solid interaction. Finally, Raman depth scan of the $HoPO_4$ crystal irradiated with 2.1 GeV Au ions up to 5×10^{11} ions/cm^2 helped to visualize the transition area between the amorphous and crystalline material. At the ion range of ∼45 μm all Raman bands start to gradually sharpen and shift towards the positions typical for nonirradiated sample. Transition takes place for the next 5-10 μm and accompanied by steady decrease of broad amorphous background.

5.3 Trends within the $LnPO_4$ series

5.3.1 Radiation damage in the monoclinic group of $LnPO_4$

In this section I will discuss radiation damage in the monazite group of rare earth phosphates. A detailed analysis of damage produced by swift heavy ions in $NdPO_4$ was provided in section 5.2.2. Here I will present an analysis of the amorphization cross-sections in several other monoclinic compounds, namely $PrPO_4$, $SmPO_4$ and $EuPO_4$.

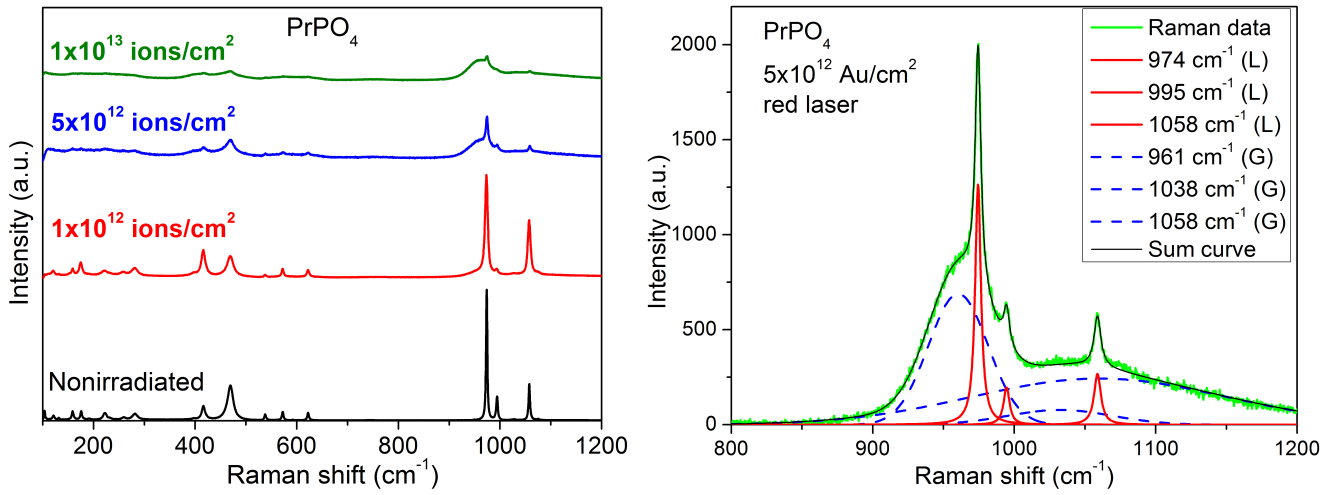

Figure 5.28: Raman spectra of $PrPO_4$ irradiated by 2.1 GeV Au ions: a) fluence series measured with red laser (λ = 632.82 nm); b) peak fit for 5×10^{12} ions/cm^2 sample.

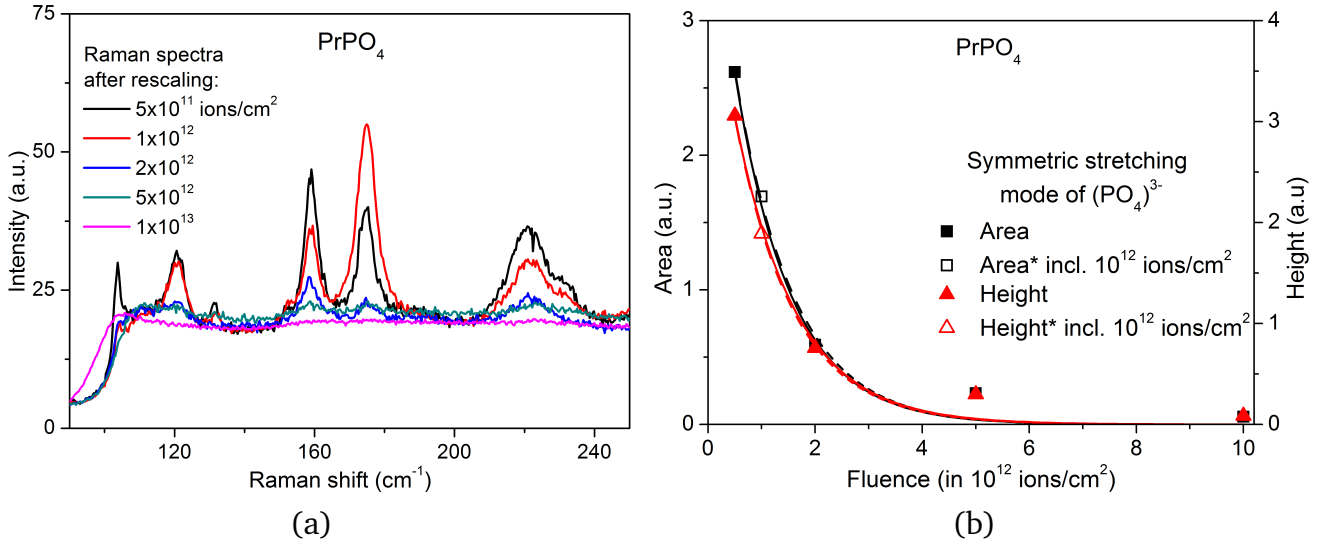

Figure 5.29: a) Raman spectra (red laser) of irradiated $PrPO_4$ after rescaling; b) absolute values of the peak area and height of $(PO_4)^{3-}$ symmetric stretching mode plotted as a function of fluence. The lines represent fits to the data using the Poisson law.

A series of Raman spectra measured using a red laser (632.82 nm) are presented as a function of ion fluence on the fig. 5.28. The large fluorescence in the $PrPO_4$ doesn't allow performing measurements with a blue laser (λ = 473.04 nm) as the luminescence completely overwhelms the spectrum (details in section 3.1). The intensity of all Raman bands goes down with increasing ion fluence. This trend appears to be similar to the behavior of $NdPO_4$ and $HoPO_4$ as discussed in previous sections. Similar to the case of $NdPO_4$, broad amorphous humps appear in the Raman spectrum with the irradiaion and progress with the fluence accumulation. Figure 5.28(b) shows a fit of Raman data in the region of PO_4 stretching modes for the $PrPO_4$ crystal irradiated by 2.1 GeV Au ions at a fluence of 5×10^{12} ions/cm^2. The broad amorphous contribution could be fit using three Gaussian peaks similar to $NdPO_4$ (indicated by the dashed lines). A lorentzian shape is used for the Raman peaks assigned to the crystalline fraction. We will later see that such a fit works well for all monazite-type rare earth phosphates unless some additional luminescent contribution in present in the spectrum.

In the sections 5.2.2 and 5.2.3 I have used a spectra renormalization (rescaling of the spectra to have an identical increase of the signal in the region between 90 and 120 cm^{-1}). This method works well if there is a signal intensity in the desired region. In this case luminescence is even welcomed as it creates a more intense background that is cut by the filter which benefits the precision of the rescaling procedure. In the ideal case, the spectra should have a significant luminescent contribution but still contain a good signal to noise ratio.

Raman spectra of the $PrPO_4$, $SmPO_4$ and $EuPO_4$ do not contain a significant luminescent background when nonirradiated. This background does not increase with the accumulation of ion fluence. I have still used this method for the analysis of the amorphization cross-section and track radii, but deduced values do not correlate with the other experimental techniques.

On fig. 5.29 the series of Raman spectra of irradiated $PrPO_4$ are plot after the rescaling. We can observe the decrease of the Raman peak intensities. The background in the region below 120 cm^{-1} is not sufficient to allow the rescaling method described above, so additionally I normalized the background level at the region 120 - 250 cm^{-1}.

Afterwards I deduced the parameters of sharp Lorentzian Raman peaks taking into consideration only their absolute area and height. Peak height and area were used for the quantification of remaining crystallinity for each fluence. Obtained data points were fit by the exponential function (eq. (5.4)) according to the direct-impact amorhpization model (details in section 5.2.2). The results are shown on fig. 5.29(b). In the case of $PrPO_4$ one sample was cracked (ion fluence of 1×10^{12} ions/cm^2) which made it impossible to obtain Raman spectra in the same orientation as for the other fluence steps. I recalculated the intensity of the symmetric stretching bond and the corresponding results are shown with hollow points on fig. 5.29(b). I have calculated the damage cross-section twice: first without the 1×10^{12} ions/cm^2 data point, and a second time including it. In both cases the values of the track radii appear to be very close. The values of damage cross-section and track radii for 2.1 GeV Au ions in $PrPO_4$ are presented in table 5.4.

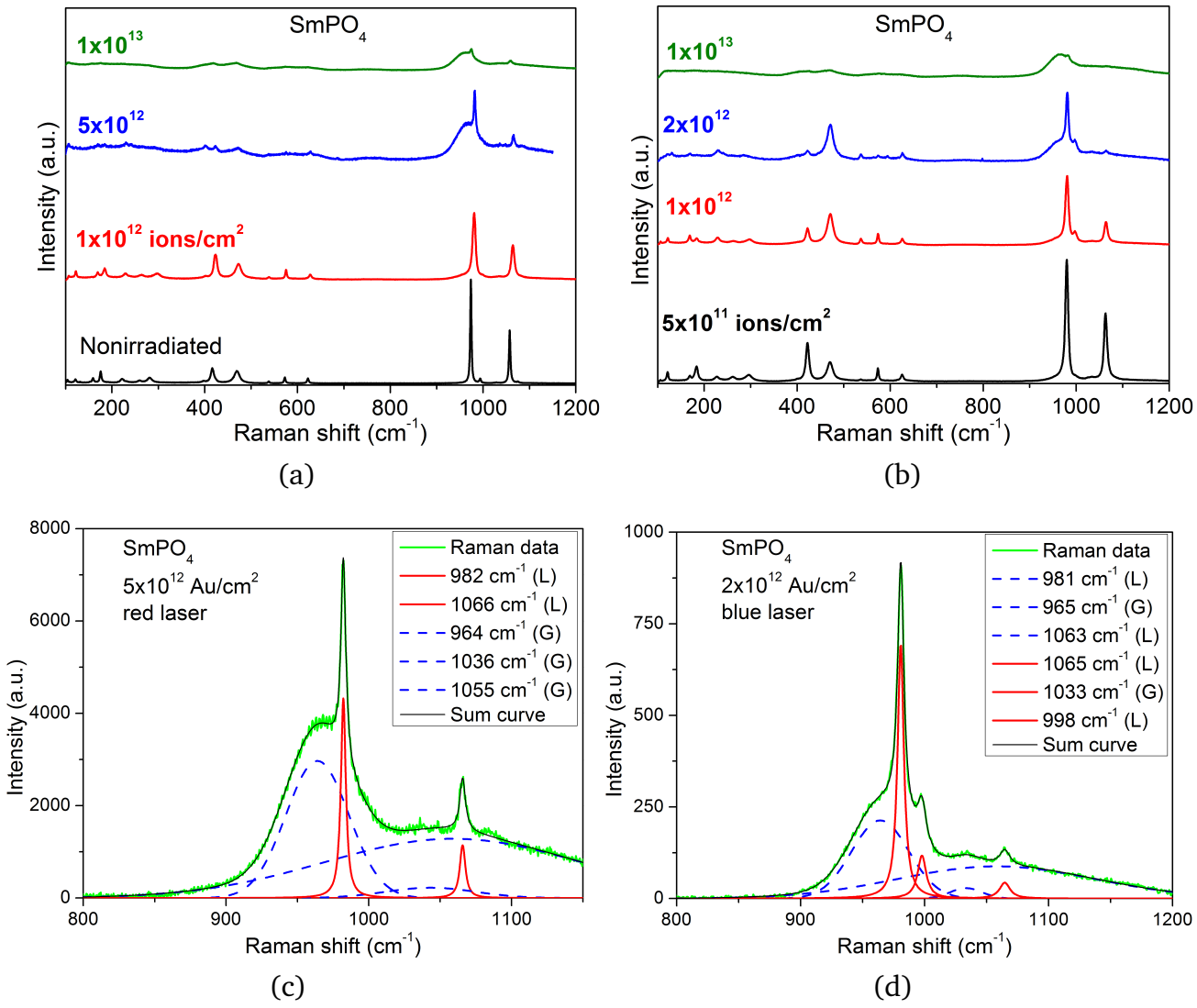

Figure 5.30: Raman spectra of $SmPO_4$ irradiated by 2.1 GeV Au ions: a) fluence series measured with a red laser (λ = 632.82 nm); b) fluence series measured with a red laser (λ = 473.03 nm); c) peak fit for the sample measured with a red laser; d) peak fit for the sample measured with a blue laser.

On fig. 5.30 we can see a series of Raman spectra for $SmPO_4$ measured with a red (fig. 5.30(a)) and a blue (fig. 5.30(b)) laser. A weak luminescent contribution could be observed in the Raman spectra for both lasers. A fit of the Raman data is shown on fig. 5.30(c) for the measurement in $SmPO_4$ crystals irradiated with 2.1 GeV Au ion up to the fluence of 5×10^{12} ions/cm^2. Unfortunately, the sample was destroyed (broke down and crumbled apart), so further measurements were not possible. That is why for the blue laser, fig. 5.30(d) shows the Raman data fit for the samples irradiated up to 2×10^{12} ions/cm^2. The main difference appears to be only in the intensities of the peaks that represent the crystalline and amorphous fractions. The rescaling of the Raman spectra was done in the way described above. Figure 5.31 shows the result of spectra rescaling and fits to the experimental data. The values of the damage cross-section and track radii for 2.1 GeV Au ions in $SmPO_4$ are reported in table 5.4.

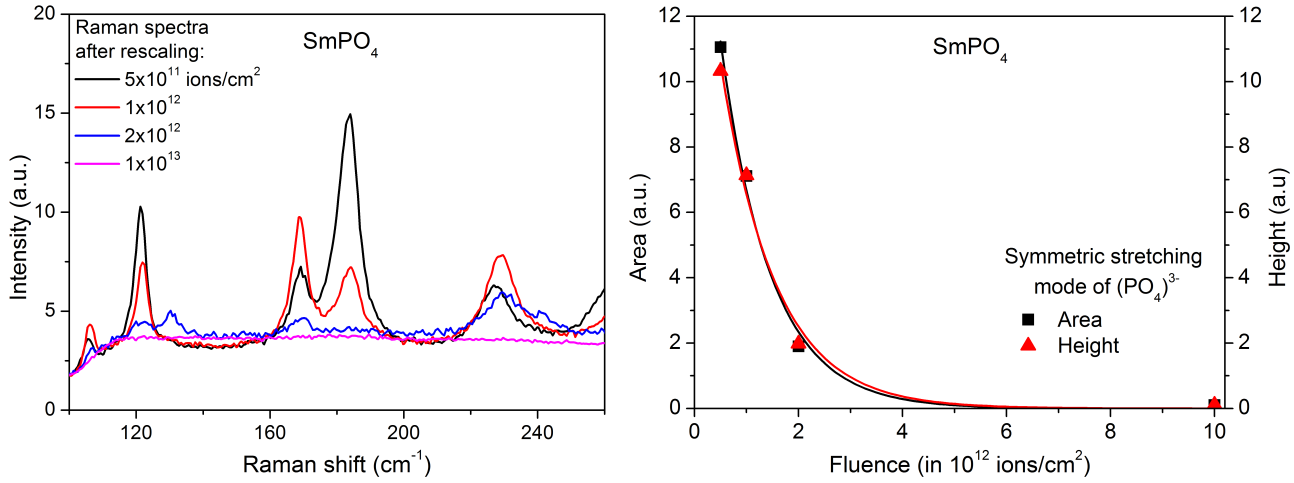

Figure 5.31: a) Raman spectra (blue laser) of irradiated $SmPO_4$ after rescaling; b) absolute values of peak area and height of $(PO_4)^{3-}$ symmetric stretching mode plotted as a function of ion fluence. The lines are fits to the data using the Poisson law.

For $EuPO_4$ some luminescent contribution could be observed in the Raman spectra obtained using a red laser. A series of Raman spectra for different fluence steps is reported on figs. 5.32(a) and 5.32(b). The fit for the spectra obtained using a red laser (fig. 5.32(c)) contains additional peaks (marked with light blue color) that were assigned to the luminescence and were not taken into account when calculating the damage cross-section. The rescaling of Raman spectra for $EuPO_4$ was done in the same way as for $SmPO_4$. I tried to compensate the lack of luminescence in the far left region of the spectrum by matching the overall background level in the broader spectral region. All the spectra could be successfully manipulated apart from the 1×10^{12} ions/cm^2 sample, where luminescence seems to be lower in comparison with the other ion fluences. The values of damage cross-section and track radius for 2.1 GeV Au ions in $EuPO_4$ are reported in table 5.4.

The variation of track radii among studied monoclinic phosphates can be illustrated by the comparison of Raman spectra in the samples that are close to be completely amorphous. Figure 5.34 shows the Raman spectra for $PrPO_4$, $NdPO_4$, $SmPO_4$ and $EuPO_4$ irradiated up to 5×10^{12} ions/cm^2. We can see an increase of intensity for the broad amorphous peaks following the increase of the cation's atomic number. At the same time, the intensity of sharp crystalline peaks follows an opposite trend, decreasing from praseodymium (Pr) to europium (Eu). A deviation from this trend is only observed for neodymium (Nd) and samarium (Sm) phosphates. Based on the existing data, it is difficult to distinguish, whether this is an experimental error, or an actual physical phenomenon.

Small-angle X-ray scattering (SAXS) measurements (details on fig. 5.35) were done on the same monazite-type phosphates that were previously discussed in this section. Samples were irradiated up to the fluence of 5×10^{10} ions/cm^2 with 2.2 GeV Au ions and polished down af-

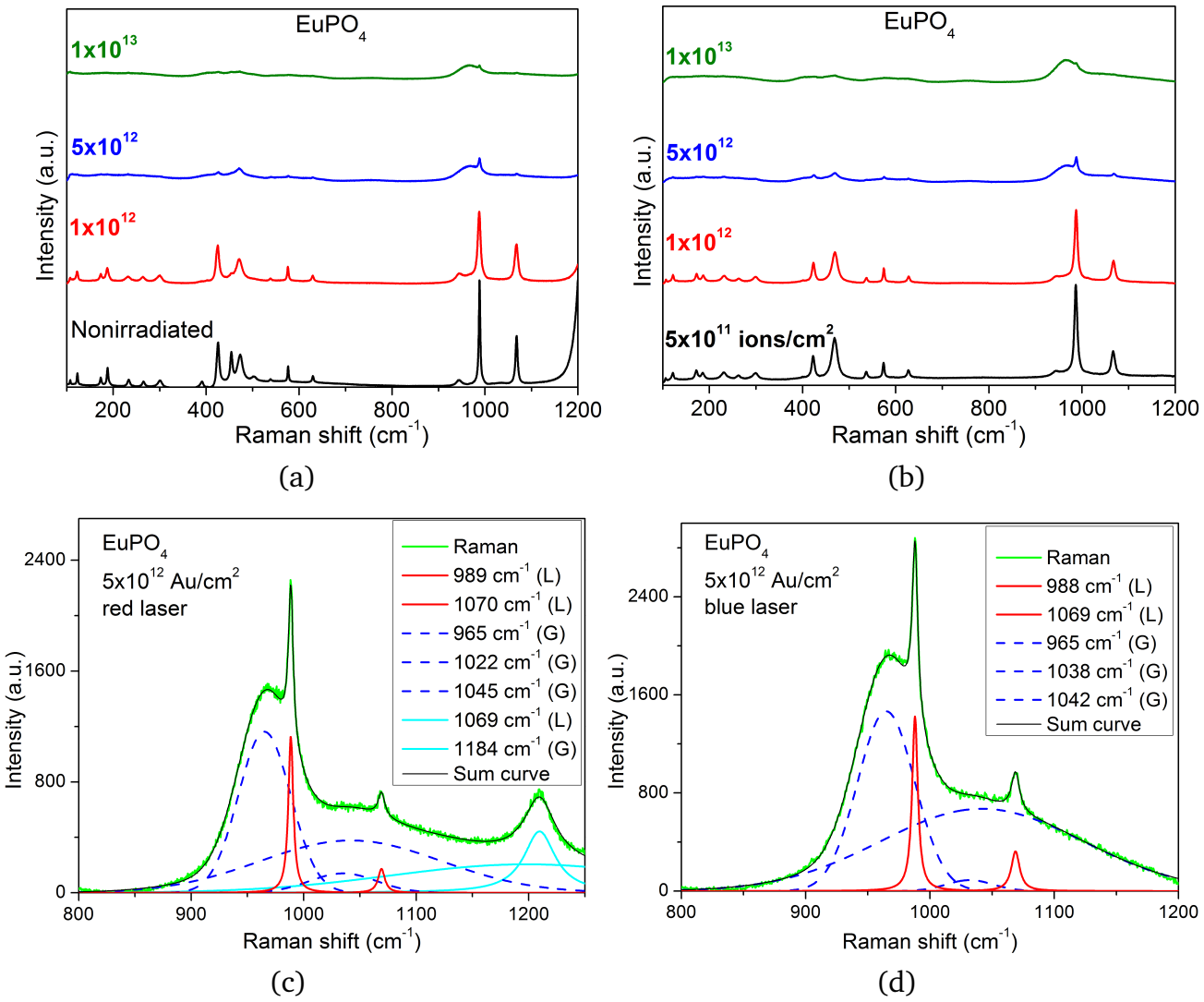

Figure 5.32: Raman spectra of $EuPO_4$ irradiated by 2.1 GeV Au ions: a) fluence series measured with a red laser (λ = 632.82 nm); b) fluence series measured with a red laser (λ = 473.03 nm); c) peak fit for the sample measured with a red laser; d) peak fit for the sample measured with a blue laser.

terwards to the thickness of approximately 30 μm. Thus, values of the track radii, that are suggested by SAXS, correspond to the track radii measured along the whole sample thickness. On the detector image of XRD reflexes (fig. 5.35) we can observe the appearance of an additional signal. This extra lines appear due to the scattering of X-rays on the extended objects with a density different from the surrounding matrix - in other words, on the ion tracks.

Figure 5.35 shows a detector image for a single crystals of (from left to right) $PrPO_4$, $EuPO_4$, $NdPO_4$, $SmPO_4$. The absence of ion tracks in the $SmPO_4$ crystal is related to a failure during sample preparation. Figure 5.36 reports the intensity variation along the line resulted from the scattering on the ion tracks (open circles). The solid lines represent the simulation of the scattering from cylindrical objects. The track radius is determined from the simulation that best fits the experimental data. In all cases a very good agreement between SAXS measurements and the simulation was achieved. The values of track radius for 2.2 GeV Au ion in $PrPO_4$, $NdPO_4$

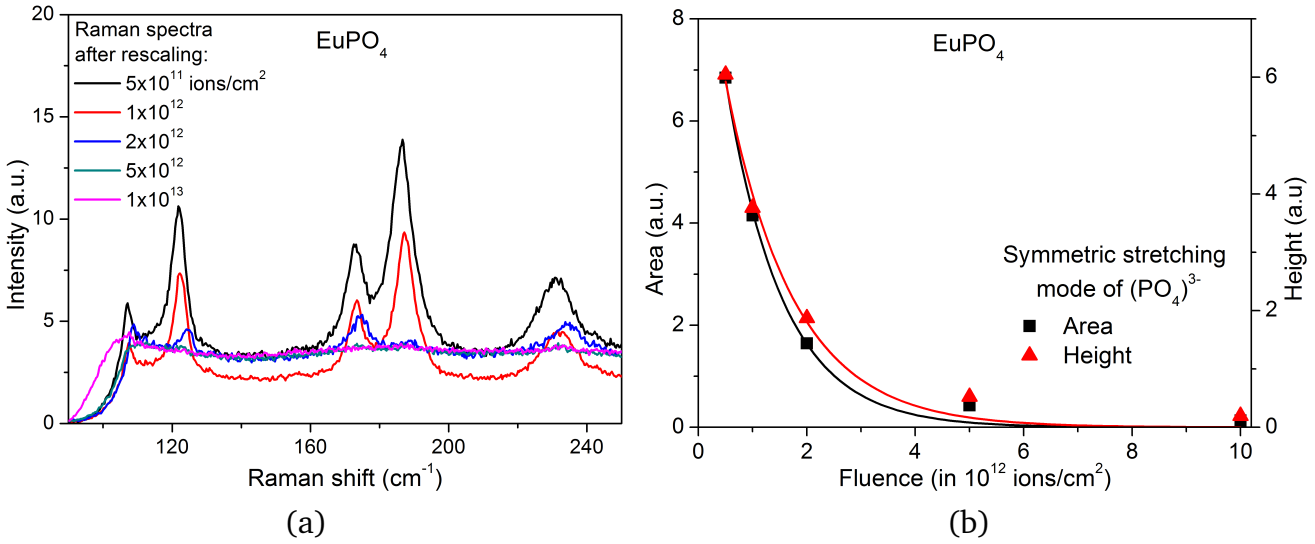

Figure 5.33: a) Raman spectra (red laser) of irradiated $EuPO_4$ after rescaling; b) absolute values of the peak area and height of $(PO_4)^{3-}$ symmetric stretching mode plotted as a function of ion fluence. The lines represent fits to the data using the Poisson law.

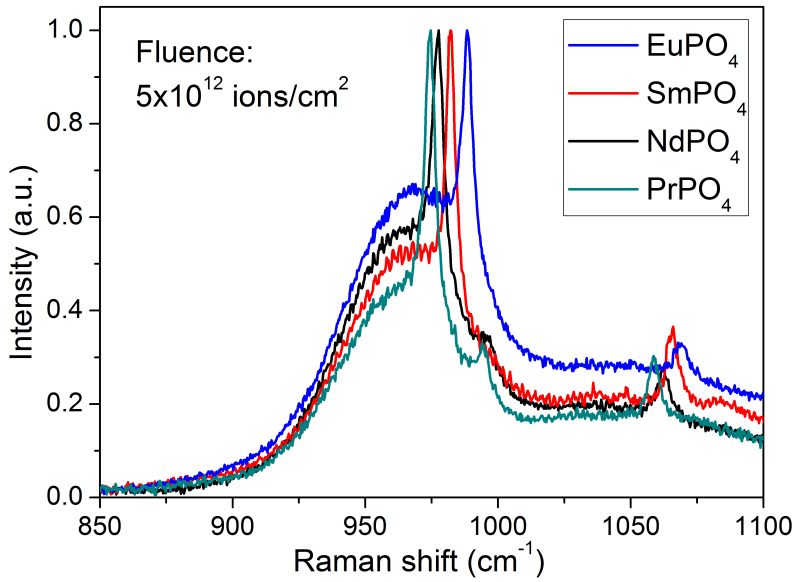

Figure 5.34: Raman spectroscopy measurements of several monazite-type lanthanide phosphates. The spectra were obtained using a 632.82 nm laser from the samples irradiated by 2.1 GeV Au ions up to 5×10^{12} ions/cm^2.

and $EuPO_4$ are reported in table 5.4. Possible variations of the track radius along the ion track (or at the different depth in the material) were taken into account as polydispersity.

The summary of track radii determination and corresponding amorphization cross-sections is reported in table 5.4. The Raman spectroscopy analysis does not allow to draw conclusions concerning the trend for track radius change depending on the rare earth cation due to a lack of precision. The SAXS data suggests a trend of slight increase in the track radius with the increase of Ln atomic number, however, values for the track radius overlap within the error bars. The

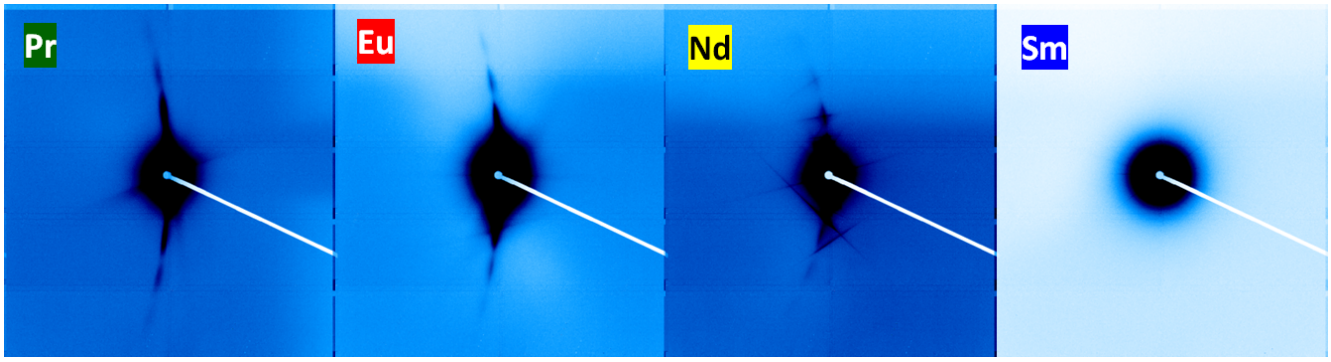

Figure 5.35: Detector image of small-angle X-ray scattering in $PrPO_4$, $EuPO_4$ and $NdPO_4$ irradiated by 2.2 GeV Au ions at 5×10^{10} ions/cm^2. In the case of $SmPO_4$, a nonirradiated sample was measured.

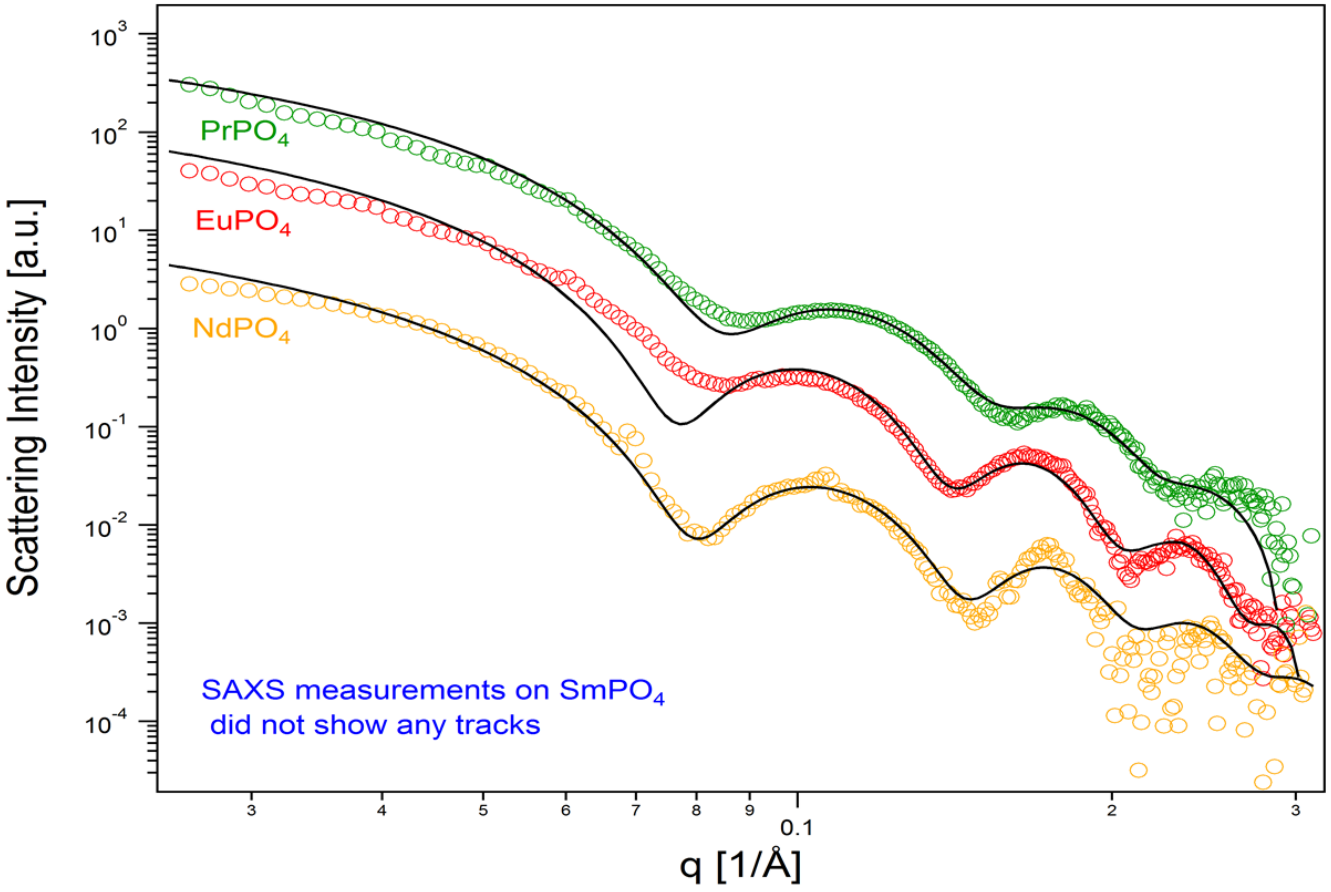

Figure 5.36: SAXS intensity as a function of scattering vector q.

density of $LnPO_4$ compounds also scales with the rare earth atomic number, resulting in an increase of electronic energy loss, what could be a further argument against this trend.

5.3.2 Radiation damage in the tetragonal group of $LnPO_4$

The Raman spectroscopy measurements performed on the tetragonal lanthanide phosphates support all previously reported results of radiation-induced changes. All the Raman measurements reported in this section were performed with a blue laser excitation (wavelength

Table 5.4: Damage cross-sections and track radii for 2.1 (Raman) and 2.2 GeV (SAXS) Au ions in monoclinic $LnPO_4$. Damage cross-sections are determined from Raman data based on the intensities and area of $(PO_4)^{3-}$ symmetric stretching modes. Raman measurements were performed with: blue laser for $NdPO_4$ and $SmPO_4$; red laser for $PrPO_4$ and $EuPO_4$.

Sample	Raman (peak area)		Raman (peak height)		SAXS
	σ_a ($\times 10^{-14}$cm^2)	R±ΔR (nm)	σ_h ($\times 10^{-14}$cm^2)	R±ΔR (nm)	R±ΔR (nm)
$PrPO_4$	95.3 88.4	5.5±0.5 5.3±0.4	92.2 90.9	5.4±0.4 5.4±0.4	4.7±0.2
$NdPO_4$	77.7	5.0±0.3	70.3	4.7±0.4	4.9±0.2
$SmPO_4$	104.7	5.8±0.6	96.0	5.5±0.5	-
$EuPO_4$	95.1	5.5±0.4	79.2	5.0±0.4	5.1±0.2

of 473.03 nm) to invoke a larger fluorescence in the spectra. This additional fluorescence does greatly improve the process of rescaling the Raman spectra. We will see that despite having a significantly variable background, the quality of the fit to the Raman data for the tetragonal phosphates is much lower than in the case of the monoclinic samples represent in section 5.3.1. For $LuPO_4$ and YPO_4 a lack of samples limited the irradiation, so that there are no data points for 2×10^{12} ions/cm^2. For YPO_4 the crystal of 1×10^{13} ions/cm^2 was destroyed prior to the measurement.

The Raman spectroscopy analysis of radiation damage in the $TmPO_4$ is shown on fig. 5.37. We can see that the changes of the Raman spectra correspond to the behavior of the monoclinic samples. Similar to $HoPO_4$, the luminescence present in the Raman spectra of virgin $TmPO_4$ decreases with increasing irradiation and vanishes at a fluence around 1×10^{13} ions/cm^2. Despite the Raman spectra having a luminescent contribution in the area below 150 cm^{-1}, the data yielded after renormalization had significantly larger uncertainties than in the case for the monoclinic samples or $HoPO_4$. The peak intensities and area of the $(PO_4)^{3-}$ symmetric stretching mode deviate from the exponential law (see fig. 5.37(d)).

In the case of $LuPO_4$, the mismatch between Raman spectroscopy data and the Poisson law is obvious (fig. 5.38). Thus, the calculation of the track radii, which is based on the intensity and area of the symmetric stretching mode, exhibits large variation. The analysis suggests a track radius of 4.9 nm based on the peak area, and 6.6 nm based on the peak height. This is related to a fewer data points and an overall lower quality of the rescaling procedure for this material. Lastly, the Raman spectra obtained for YPO_4 do not allow to calculate the track radius at all. Having few irradiated samples, the Raman spectra of the YPO_4 crystals irradiated at a 5×10^{11} and 1×10^{12} ions/cm^2 produce nearly identical Raman spectra. This is most likely linked to the low density of YPO_4 and thus a much smaller track radius than in the case of the other reported compounds. With Raman data having very similar peak intensities, the slight variation of the

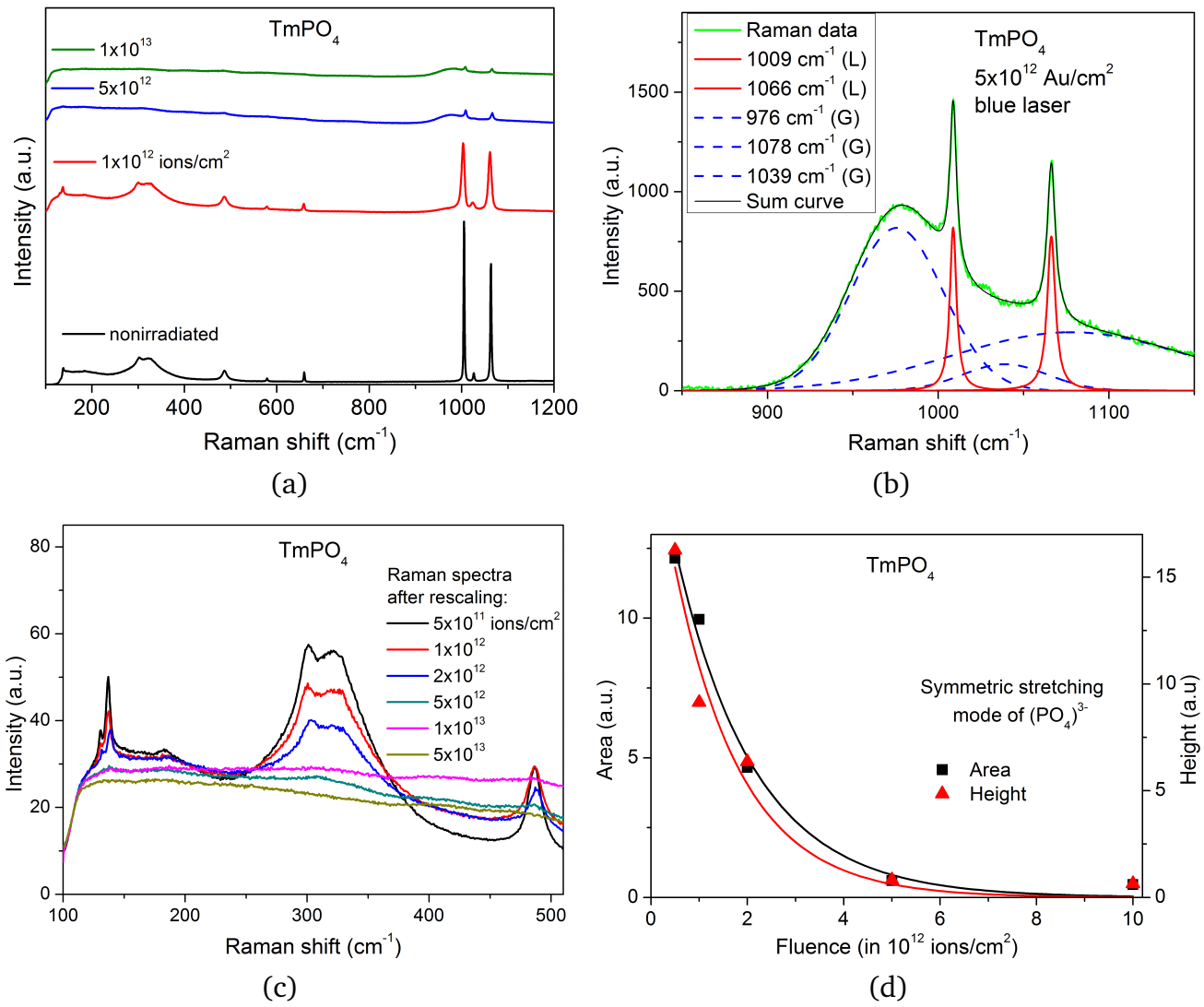

Figure 5.37: Raman spectroscopy analysis of radiation damage produced by 2.1 GeV Au ions in $TmPO_4$: a) a series of Raman spectra measured with a blue laser plotted as a function of ion fluence; b) peak fit for a sample measured with a blue laser; c) Raman spectra of irradiated $TmPO_4$ after rescaling; d) absolute values of the peak area and height of the $(PO_4)^{3-}$ symmetric stretching mode plotted as a function of ion fluence. The lines are fits to the data using Poisson law.

data for the sample irradiated at $1{\times}10^{12}$ ions/cm^2 drastically affects the analysis results. That makes a quantitative analysis of the track radii for YPO_4 completely unfeasible.

Qualitatively we can observe a difference in the radiation damage produced by 2.1 GeV Au ions in the four tetragonal phosphates (discussed in this chapter) by the comparison of samples irradiated at $5{\times}10^{12}$ ions/cm^2. On fig. 5.40 we can clearly observe a much lower intensity of the amorphous hump and more intense crystalline peaks for the YPO_4 sample compared to the other phosphates. For the other three tetragonal phosphates, the dependency is not so straightforward. On the one hand, the intensity of the Raman signal between 1000 and 1150 cm^{-1} increases from $HoPO_4$ to $TmPO_4$ over to $LuPO_4$, but at the same time this requires a decrease of the main hump close to 970 cm^{-1} to have a similar overall Raman signal intensity.

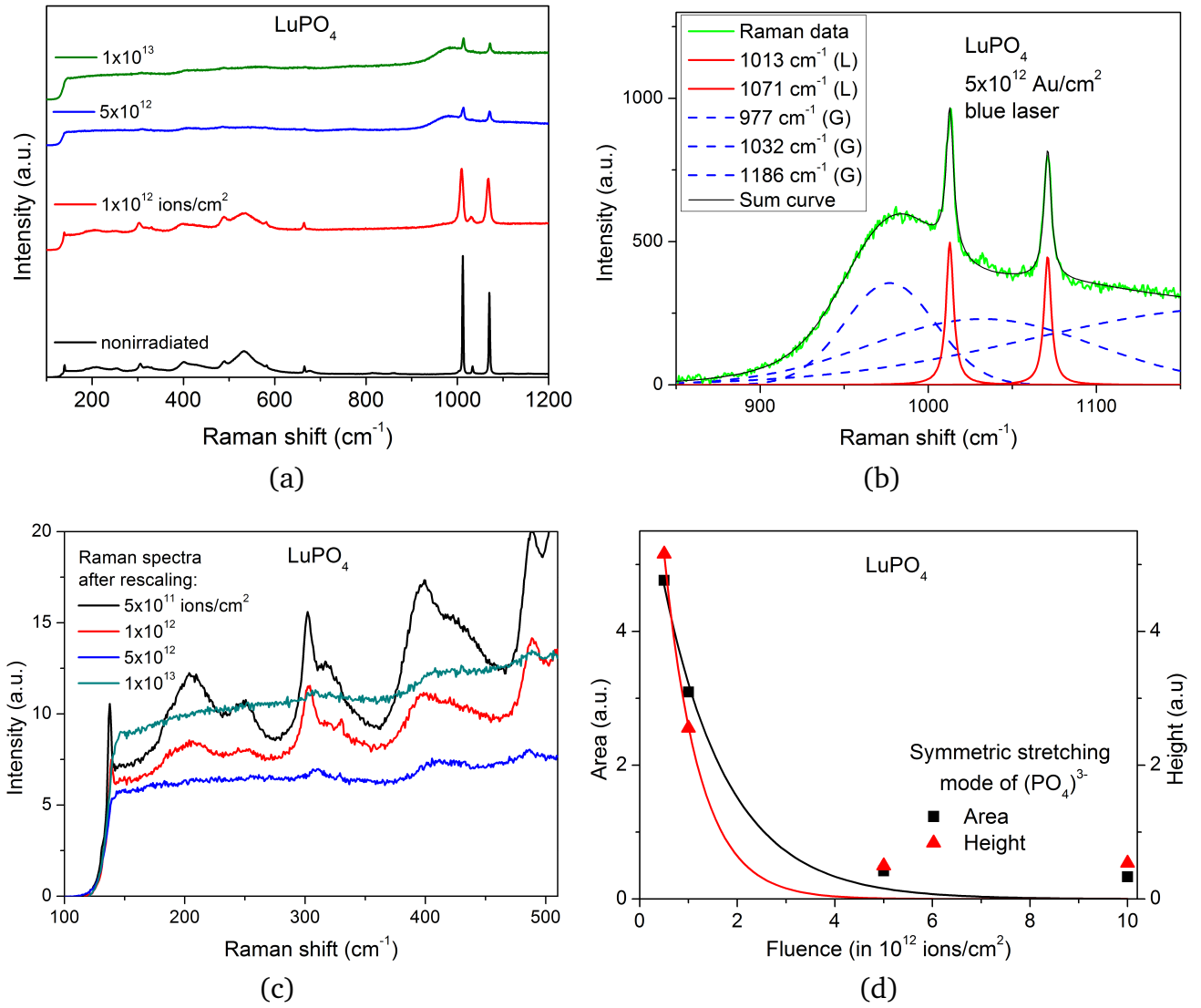

Figure 5.38: Raman spectroscopy analysis of radiation damage produced by 2.1 GeV Au ions in $LuPO_4$: a) A series of Raman spectra measured with a blue laser, plotted as a function of ion fluence; b) peak fit for a sample measured with a blue laser; c) Raman spectra of irradiated $LuPO_4$ after rescaling; d) absolute values of the peak area and height of the $(PO_4)^{3-}$ symmetric stretching mode plotted as a function of ion fluence. The lines represent fits to the data using the exponential law.

It is not clear whether the only hump close to 970 cm^{-1} represents a Raman signal from the amorphous fraction. In most irradiated samples we can observe one more intense Gaussian hump at around 1070-1100 cm^{-1}. But this hump at 1070-1100 cm^{-1} is absent for $HoPO_4$, a sample with a simple linear background in the region of the stretching modes, where one would expect a most reliable fit to the experimental data. All of this advocates that an estimation based only on the hump at 970 cm^{-1} suggests a degree of amorphization that is decreasing from Ho to Tm, Lu and Y.

The summary for the calculation of the track radii and the amorphization cross-sections for 2.1 GeV Au ions in tetragonal rare earth phosphates is reported in table 5.5. The larger un-

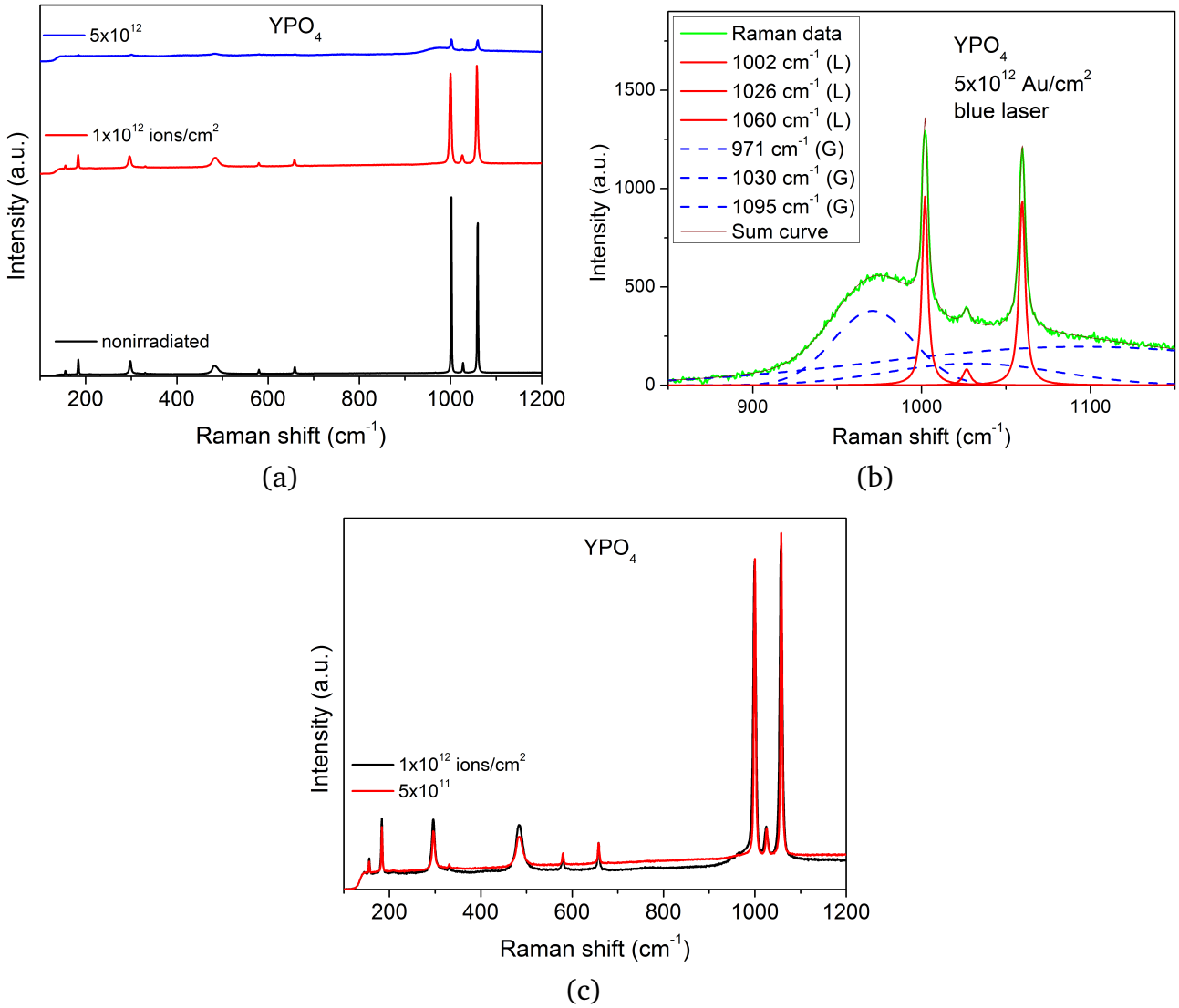

Figure 5.39: Raman spectroscopy analysis of radiation damage produced by 2.1 GeV Au ions in YPO_4: a) A series of Raman spectra measured with a blue laser plotted as a function of ion fluence; b) peak fit for a sample measured with a blue laser; c) The calculation of the damage cross-section was not possible based on the existing data because the Raman spectra of the samples irradiated at 5×10^{11} and 1×10^{12} ions/cm^2 do not show any significant changes.

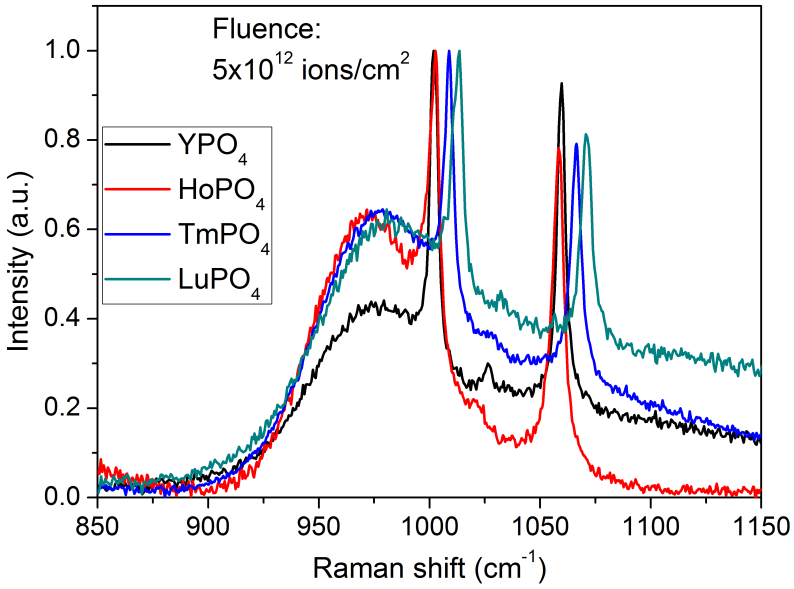

Figure 5.40: Raman spectroscopy measurements of several tetragonal lanthanide phosphates irradiated by 2.1 GeV Au ions at 5×10^{12} ions/cm^2. Spectra were obtained using a laser with a $\lambda = 473.03$ nm.

certainties for track radii compared to the values presented for the monoclinic phosphates are related to a poor quality of the Raman data fit to the Poisson law.

Table 5.5: Damage cross-sections and track radii for 2.1 GeV Au ions in tetragonal $LnPO_4$. Damage cross-sections are determined from the Raman data based on intensities and area of the $(PO_4)^{3-}$ symmetric stretching mode. Raman measurements were done with a blue laser for all presented samples.

Sample[a]	Raman (peak area)		Raman (peak height)	
	σ_a ($\times10^{-14}$cm^2)	R±ΔR (nm)	σ_h ($\times10^{-14}$cm^2)	R±ΔR (nm)
$HoPO_4$	73.9	4.9±0.3	75.2	4.9±0.4
$TmPO_4$	60.9	4.4±0.7	71.4	4.8±0.9
$LuPO_4$	75.3	4.9±1.0	79.2	6.6±1.6

[a] Existing experimental data did not allow the calculation of track radii for YPO_4.

X-Ray diffraction measurements were done to observe the amorhpization and calculate the damage cross-section using another experimental technique investigating several tetragonal phosphates (YPO_4, $TmPO_4$ and $ErPO_4$). The choice of those particular samples was based on the crystal size and availability of appropriate sample to perform the experiment within a reasonable measurement time.

The single-crystal X-Ray diffraction measurements were performed on three tetragonal rare earth phosphates: YPO_4, $TmPO_4$ and $ErPO_4$. Two types of measurements were performed after each ion fluence step: standard “Two theta” (2θ) and “Chi” scans. The 2θ angle gives a set of peaks that satisfy the Bragg’s law. The Chi scan is done by a sample rotation with fixed 2θ at the maximum intensity of a desired reflex. Thus, 2θ measurements give access to understanding the sample amorphization, whereas a Chi scan was used to observe the relative orientations of

surface domains in single crystals. The specifications of X-Ray measurements and a scheme of the experiment are reported in section 4.3.1.

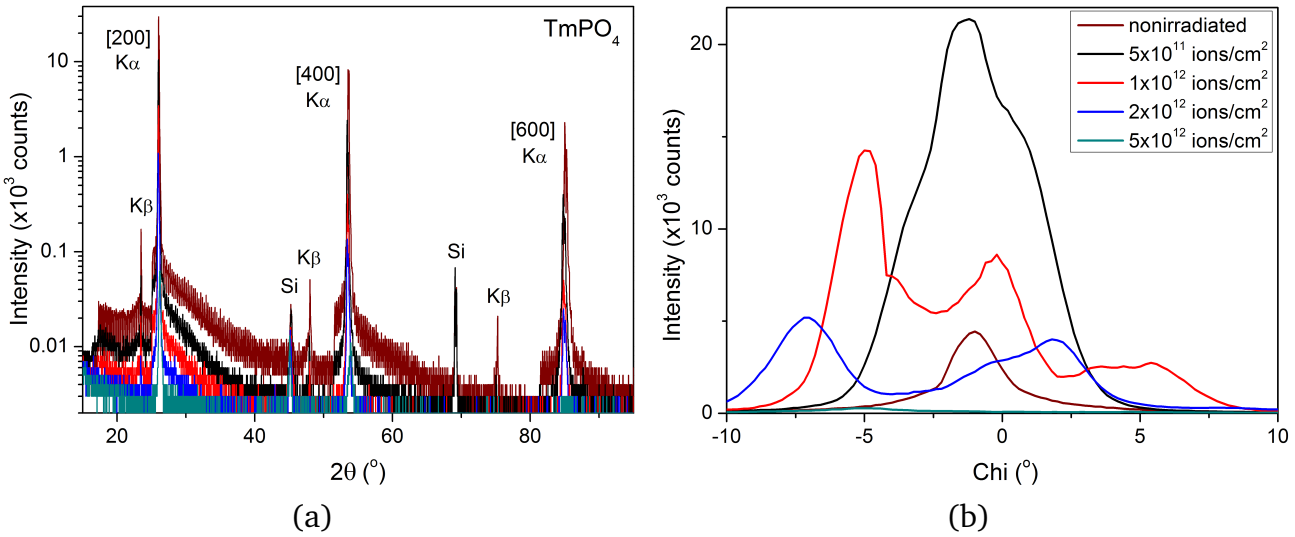

Figure 5.41: XRD measurements for $TmPO_4$ irradiated with 945 MeV Au ions: a) 2 theta scan; b) Chi scan.

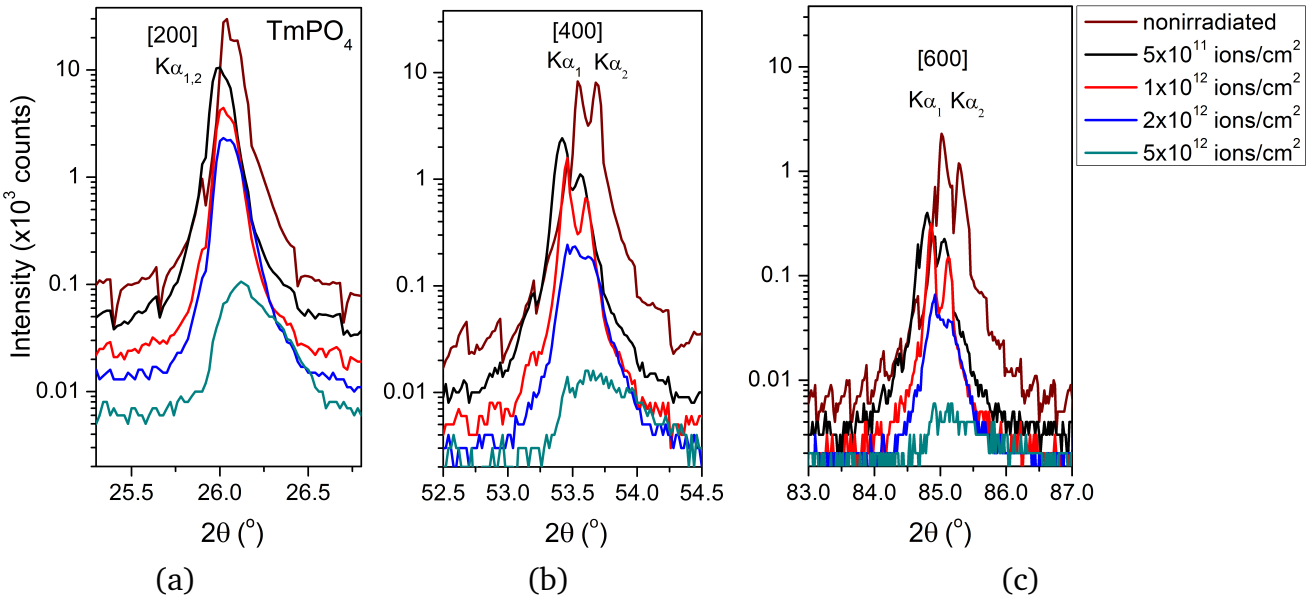

Figure 5.42: XRD measurements for $TmPO_4$ irradiated with 945 MeV Au ions (measured at maximum of Chi): a) [200]; b) [400]; c) [600].

Figure 5.41 reports the results of XRD online measurements of $TmPO_4$ irradiated with 945 MeV Au ions (corresponds to 4.8 MeV/u specific energy). The spectra are presented as a function of ion fluence. Results of the 2θ scans are shown on fig. 5.41(a). The intensities of all peaks decreases with accumulation of ion fluence. The expected amorphization of the sample typically appears as an increase of the background close to XRD reflexes. However, we can observe a steady decrease of the background intensity in all the measured spectra. This

pattern can be found as well in the other samples. An explanation could be given, taking into account the absence of a monochromator in the used XRD system. In addition to the Cu Kα_1, Kα_2 and Kβ emission lines, a "white" X-Ray beam (Bremsstrahlung) is provided to the sample. In the beginning, the samples maintain a crystallinity, so a significant portion of the "white" signal contributes to the background. With the sample amorphization, a intensity decrease of the scattered X-Rays can be observed not only for the main emission lines, but also for the "white" part of X-Ray tube emission, resulting in the described lowering of the background.

In this work I have repeatedly mentioned the weak mechanical stability to the radiation damage in tetragonal phosphates. A series of Chi scans on $TmPO_4$ irradiated by 945 MeV Au ions shown on fig. 5.41(b) shows a sample fracturing. The nonirradiated single crystal produces a symmetric Chi reflex. With ongoing irradiation, the Chi reflex starts to split into several peaks, which suggests the formation of polycrystalline domains with the sample. The Chi scans were done at the 2θ maximum for the Kα_1 emission line of the [200] reflex. The XRD measurement of the nonirradiated sample was done in the air environment, resulting in a lower absolute signal than for the subsequent measurements of the irradiated samples, which were performed in vacuum. With the ion-fluence accumulation, the clear split of the initial Chi peak can be observed. Decreasing in the intensity, the Chi peaks continue to shift from the initial position.

Additional 2θ measurements were performed for each of the two most intense Chi reflexes: the main peak that shifts from -1 to -5 and to -7.5 (fig. 5.42); secondary peak that shifts from -1 to 0 and to 2.5 (fig. 5.43). In both cases all 2θ reflexes showed a similar trend of intensity decrease with the irradiation. The used XRD system doesn't provide a possibility to vary the omega angle, so a determination of the full intensity of a particular peak was not possible.

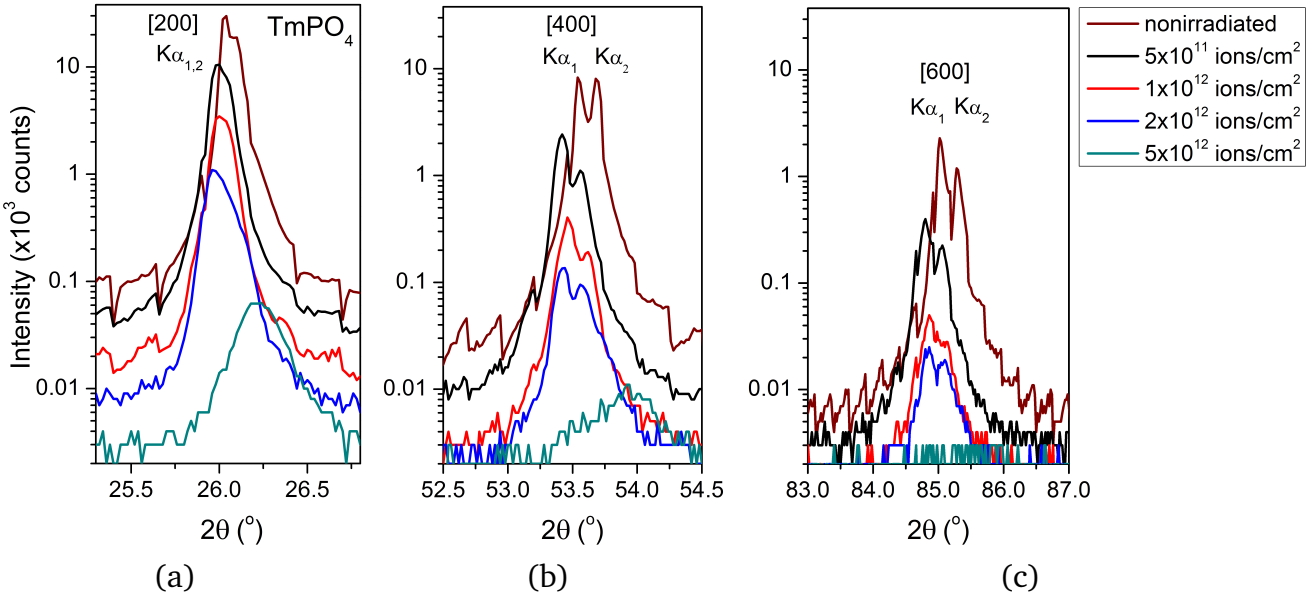

Figure 5.43: XRD measurements for $TmPO_4$ irradiated with 945 MeV Au ions (measured at secondary Chi): a) [200]; b) [400]; c) [600].

Thus, the analysis of absolute values of peak intensities does not allow a calculation of track radii.

However, the position of XRD peaks provides support to the phenomena of unusual peak shifts with increasing ion fluence, that was observed in section 5.2.4. At the first fluence step of 5×10^{11} ions/cm^2, all reflexes shift towards smaller 2θ angles (to larger d-spacing). The subsequent irradiation produces a consistent shift of all the peaks towards larger 2θ angles. At a fluence of 5×10^{12} ions/cm^2, the positions of the reflexes roughly correspond to the values of the nonirradiated crystal.

Similar to the case of $TmPO_4$, the same XRD measurements were done on a YPO_4 crystal. The measurements of 2θ and Chi as a function of ion fluence are represented on fig. 5.44. This sample was not measured before the irradiation. Thus, both fig. 5.44(a) and fig. 5.44(b) contain a series of fluence steps without a measurement of the virgin sample.

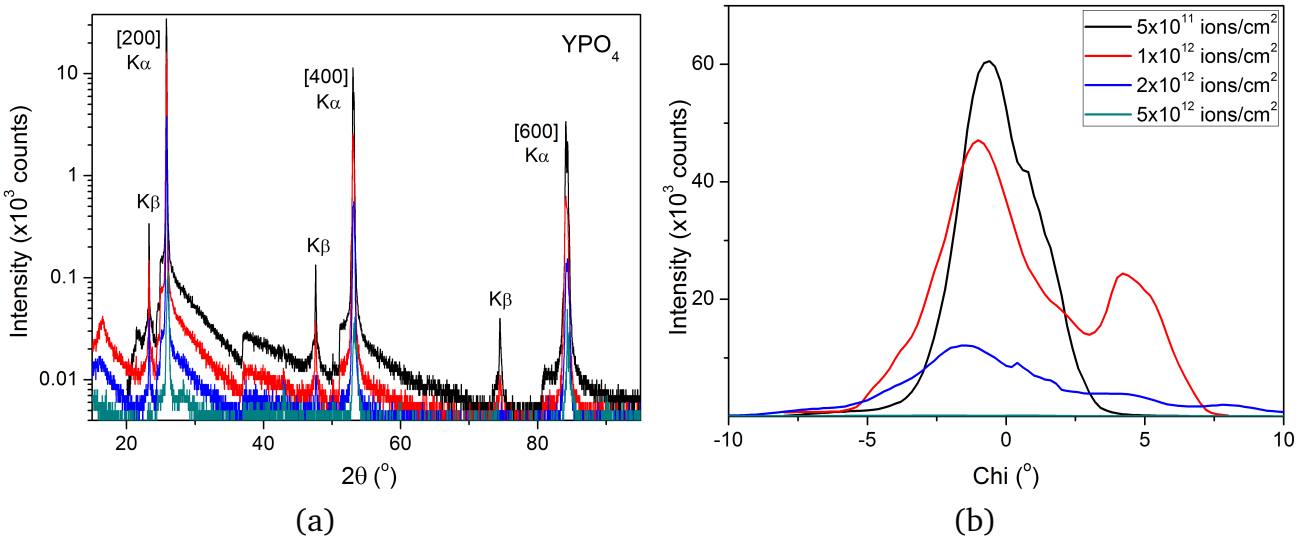

Figure 5.44: XRD measurements for YPO_4 irradiated with 945 MeV Au ions: a) 2 theta scan; b) chi scan.

Another crystal of YPO_4 was measured offline at a similar system using the same X-Ray wavelength. The position of the peaks for the CuKα_1 emission line for the [200], [400] and [600] reflexes in the nonirradiated sample are shown as brown line on fig. 5.45. The analysis of the peak positions suggests, that a change in the direction of peak shift appears at slightly elevated ion fluences for YPO_4 in comparison to the $TmPO_4$. Namely, for the first two irradiation steps up to the ion fluence of 10^{12} ions/cm^2, all the peaks shift towards smaller 2θ angles. This trend is inverted at further irradiation. In the previous sections I have shown a direct correlation between the damage production efficiency and the value of electronic energy loss inside of the material. That is why such a discrepancy between YPO_4 and $TmPO_4$ could be related to the lower density in YPO_4 and, as result, smaller values of electronic energy loss for 945 MeV Au ions in YPO_4. The smaller amorphization cross-section simply requires an accumulation of larger fluence to produce significant influence on the nonirradiated surrounding matrix.

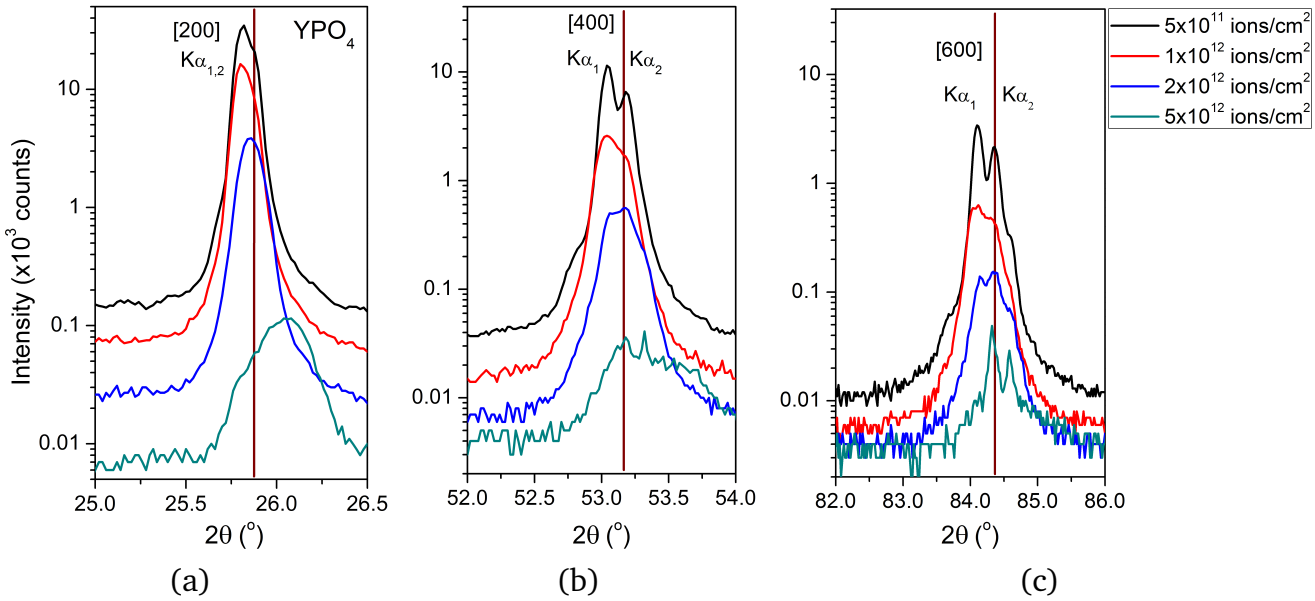

Figure 5.45: XRD measurements for YPO_4 irradiated with 945 MeV Au ions: a) [200]; b) [400]; c) [600].

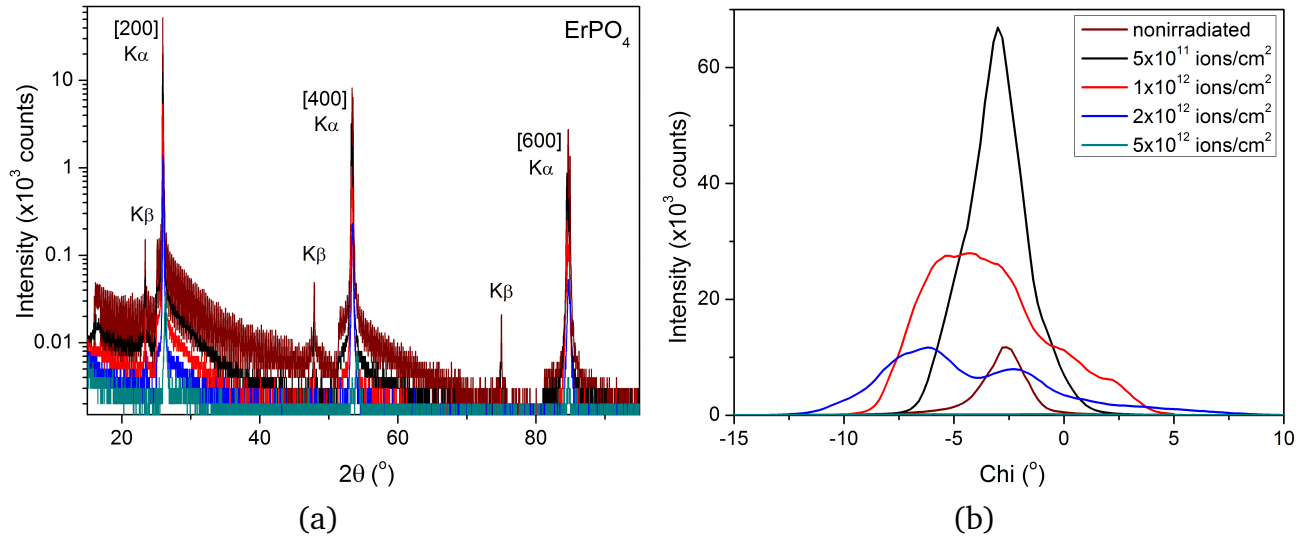

Figure 5.46: XRD measurements for $ErPO_4$ irradiated with 945 MeV Au ions: a) 2 theta scan; b) Chi scan.

In $ErPO_4$, XRD measurements have shown trends similar to $TmPO_4$. Figure 5.46 shows the change of XRD spectra for the various ion fluence steps. A low signal intensity during Chi measurement for nonirradiated sample appears due to the XRD measurement performed in air. Similar to the other samples, we can observe a decrease of the intensity of all peaks accompanied by a decrease of the background (fig. 5.46(a)). The changes in Chi (fig. 5.46(b)) suggest the fragmentation of the single crystal, similar to what was observed in YPO_4 and $TmPO_4$. The XRD peak shift follows the trend similar to $TmPO_4$: at the very first irradiation step all peaks are shifted towards lower diffraction angles, and for the subsequent irradiation steps all the peaks steadily moved towards higher values.

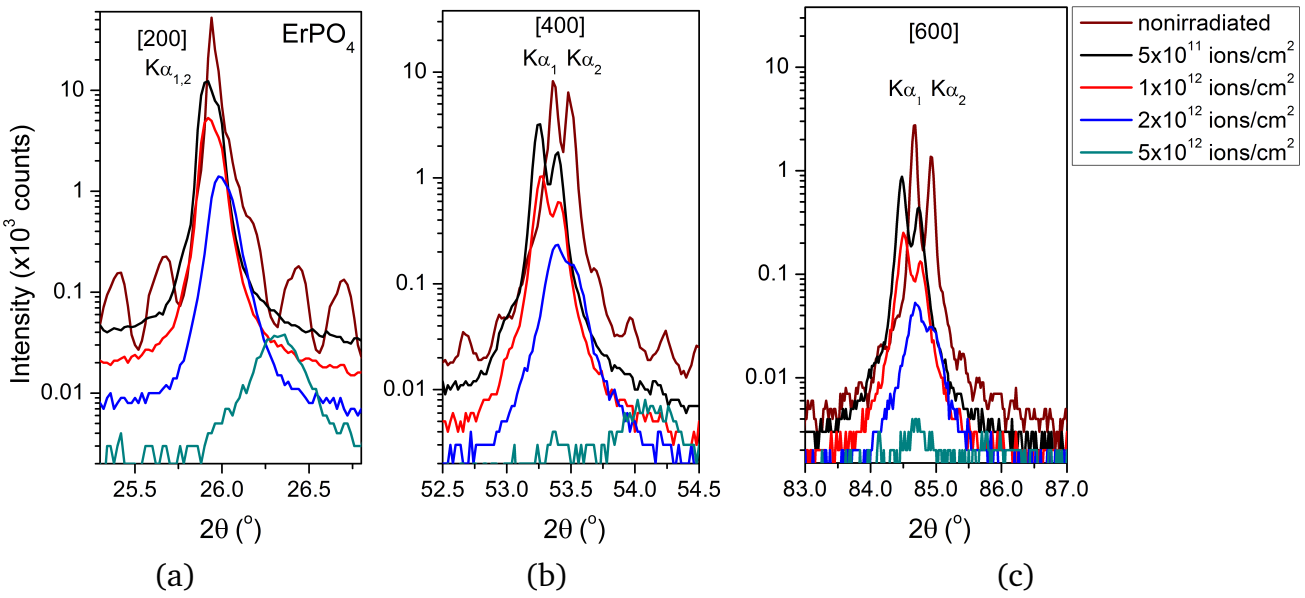

Figure 5.47: XRD measurements for $ErPO_4$ irradiated with 945 MeV Au ions: a) [200]; b) [400]; c) [600].

The shift of XRD reflexes to the lower angles for the first ion fluence step indicates an increase of the inter-atomic distances in the planes parallel to the irradiated (and measured) surface. This trend reverses at higher ion fluences where all the XRD peaks shift towards larger angles. This behavior is quite similar to the change in Raman peak positions discussed in section 5.2.4 and in fact happens even at the exact same fluence steps. Additionally there is another underlying phenomena which can explain this behavior. In this case it is more likely, that shifts of XRD peaks reflect the accumulation of macroscopic stresses in the crystals. Samples being fixed with the epoxy on the silicon wafer (see section 4.1) have very little room for the release of accumulated stress and with the discrete fluence steps, the release of stresses coincides with the fluence where defect halos start to overlap (see section 5.2.4). Mechanical stresses induced by the irradiation lead to severe sample cracking (shown on fig. 4.2) and a precise detection, when the samples start to crack, is very difficult with the used experimental setup.

The Raman spectroscopy measurements were performed for $ErPO_4$, $TmPO_4$ and YPO_4 samples offline after the XRD experiments. After the irradiation all crystals had a large amount of cracks. Small platelets of samples containing both irradiated layer and parts of the virgin sample material were broken off from each sample and used for the Raman measurements. Figure 5.48 shows Raman spectra of $TmPO_4$, YPO_4 and $ErPO_4$ crystals irradiated by 945 MeV Au ions at the fluence of 5×10^{12} ions/cm^2. Some parasitic reflexes could be observed in the Raman spectra of $TmPO_4$ and YPO_4 which do not belong to the spectra of sample itself but come from traces of epoxy used for mounting the sample. The Raman spectra suggest an almost complete amorhpization for all samples. The remaining traces of the symmetric stretching mode suggest

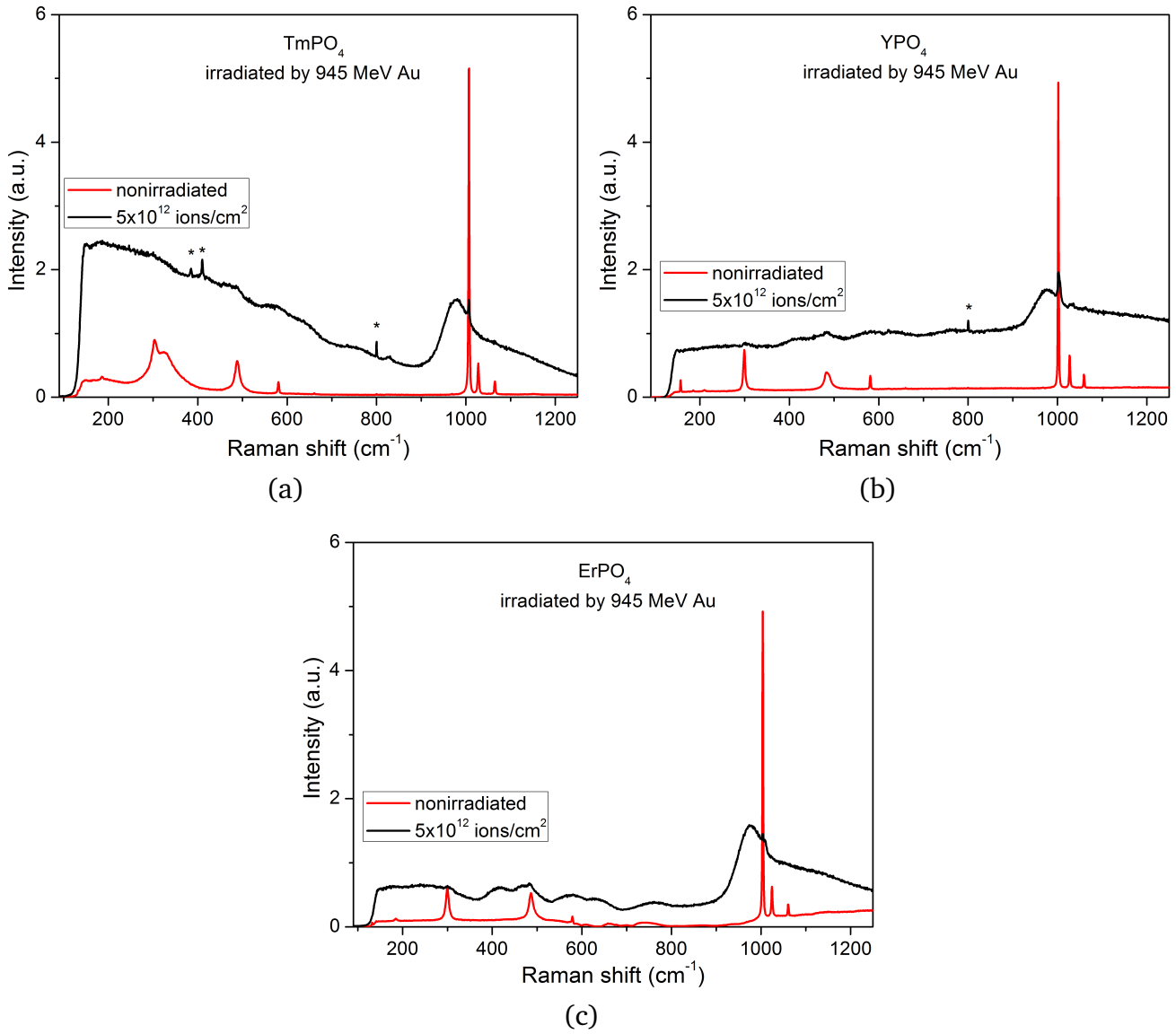

Figure 5.48: *ex-situ* Raman spectroscopy measurements of rare earth phosphates irradiated with 945 MeV Au ions up to the fluence of 5×10^{12} ions/cm^2: a) $TmPO_4$, b) YPO_4, c) $ErPO_4$. Reflexes marked with an asterix originate from the glue used for mounting the sample during the online XRD experiments.

a slightly lower degree of amorphization for the YPO_4 crystal. This is associated with the lower energy deposition for the Au ions in this material compared to the other.

5.3.3 Full series of $LnPO_4$ irradiated at exact same conditions

A series of all lanthanide phosphates was irradiated by 2.1 GeV Au ions up to the fluence of 2×10^{12} ions/cm^2 for the purpose of studying the production of radiation damage depending on the Ln^{3+} cation. Irradiation conditions are considered to be exactly the same as the samples were irradiated on the same holder with the same flux. With the severe deficiency in the sample quantity it was impossible to perform a full series of irradiations for all the materials. The

fluence was chosen estimating the track radii for 2.1 GeV Au ions to be around 5 nm, where a fluence of 2×10^{12} ions/cm^2 would provide severe amorphization with the ratio of the Raman signal from the amorphous and crystalline parts being roughly 50:50.

The Raman spectroscopy analysis that was used for this series is described in section 5.2.1. The area of the sharp intense Raman bands was assigned to the amount of remaining crystalline sample volume, whereas the area of the broad hump represented the amount of amorphous sample material. In section 5.2.1 it was shown that such a method of Raman analysis yields worse results compared to the analysis of absolute Raman peak parameters after the Raman spectra renormalization. With the many various backgrounds and luminescent contributions, a renormalization of Raman spectra for all the phosphates was not possible. Instead I have chosen the less reliable approach, hoping that I can at least figure out the trends for radiation hardness within the monoclinic and tetragonal groups.

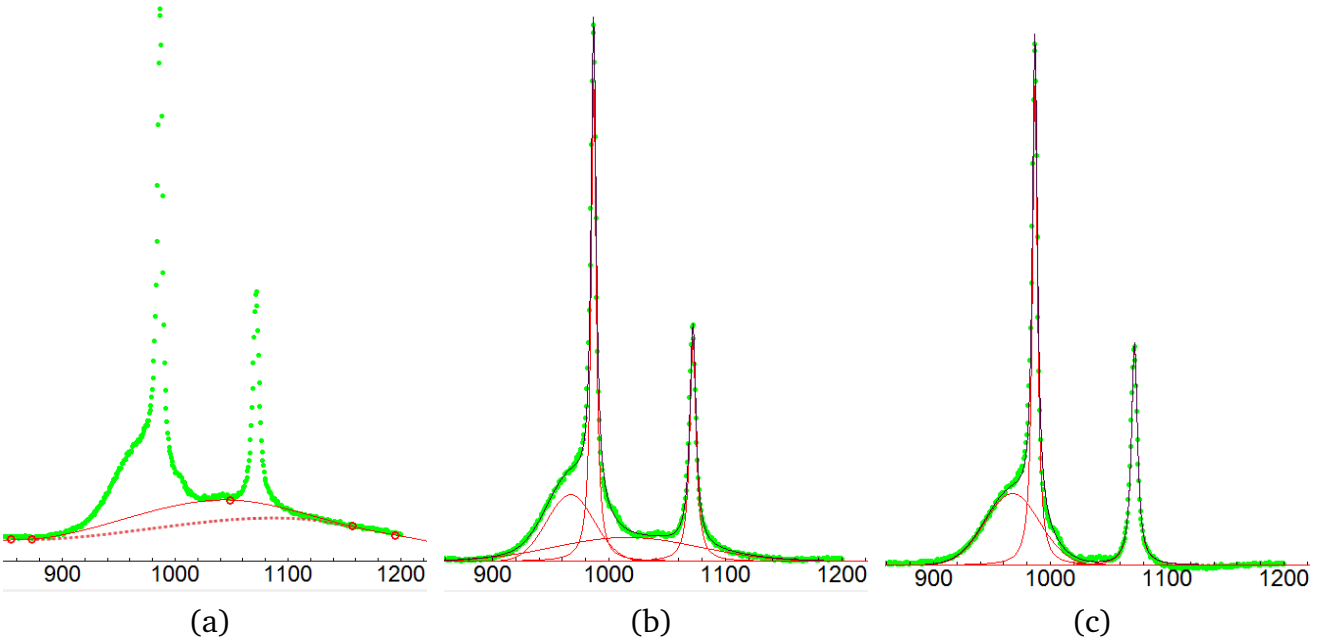

Figure 5.49: Fit of the Raman data of $GdPO_4$ irradiated with 2.1 GeV Au ions up to 2×10^{12} ions/cm^2: a) background fit: slight cut - dashed line, extensive cut - solid line; b) peak fit for slight cut; c) peak fit for extensive cut.

With the aim to reduce the dependence of my results on the luminescent contribution and radiation induced background, I have subtracted the background for each Raman spectra in two ways. For the first way, denoted as “slight cut” on fig. 5.49(a), I picked the points for the background fitting relatively far from the spectral region of interest and let the background function be linear-like. For the other way, that I refer to as “extensive cut” on fig. 5.49(a), I selected points to cut away as much contribution as possible outside the range of the main broad hump around 960 cm^{-1}, that is observed as an universal feature in all lanthanide phosphates. The fits of the Raman data for the slight cut and for the extensive cut are shown on fig. 5.49(b) and fig. 5.49(c), respectively. A quantification of the amorphous fraction was done taking into

account only the broad hump around 960 cm^{-1}, and the crystalline fraction was characterized by the area of the symmetric stretching mode of the PO_4 tetrahedron (for $GdPO_4$ on the fig. 5.49 this mode is slightly below 1000 cm^{-1}).

The calculation of the amorphization cross-section and track radii was based on the direct impact amorphization model. The fraction of crystalline sample volume (C∈[0,1]) at the particular fluence step (Φ) should follow an exponential decay. In this case at the fluence step Φ the fraction of remaining crystalline material C could be written as:

$$C = \exp(-\pi R^2 \Phi), \tag{5.6}$$

that gives an expression for track radius:

$$r = \sqrt{\frac{\ln\frac{1}{C}}{\pi\Phi}}. \tag{5.7}$$

Now I had to consider values of uncertainty of this determined track radius. A general expression for error calculation could be written as

$$\Delta F = \sqrt{\sum_{i=1}^{n}\left[\Delta x \frac{\partial F}{\partial x_i}\right]^2}. \tag{5.8}$$

Series of following simple mathematical calculations

$$\Delta r = \frac{\partial r}{\partial C}\Delta C, \qquad \text{using} \qquad \frac{\partial r}{\partial C} = \frac{1}{\sqrt{\pi\Phi}} \times \frac{1}{2\cdot\sqrt{\ln\frac{1}{C}}} \times C \times \left(\frac{1}{-C^2}\right) \tag{5.9}$$

would give the formula for error of track radius determination as:

$$\Delta r = \frac{1}{2C\sqrt{\pi\Phi\ln\frac{1}{C}}}\Delta C. \tag{5.10}$$

The values of track radii for all the phosphates were calculated according to eqs. (5.7) and (5.10). The calculation of track radius using eqs. (5.7) and (5.10) does not take into account the uncertainty of the fluence determination. This assumption is valid because the full series of phosphates was irradiated at the same time with the same ion fluence.

For the monoclinic group of phosphates, the results of the analysis drastically scatter and a steady trend could not be observed on fig. 5.50. Track radii have a slight tendency to increase with the decrease of the ionic radii of the Ln^{3+} cations. This trend correlates with the analysis results represented in section 5.3.1. The Raman data for the tetragonal group of lanthanide phosphates suggests a more pronounced trend of track radius decrease with decreasing Ln^{3+} ionic radius.

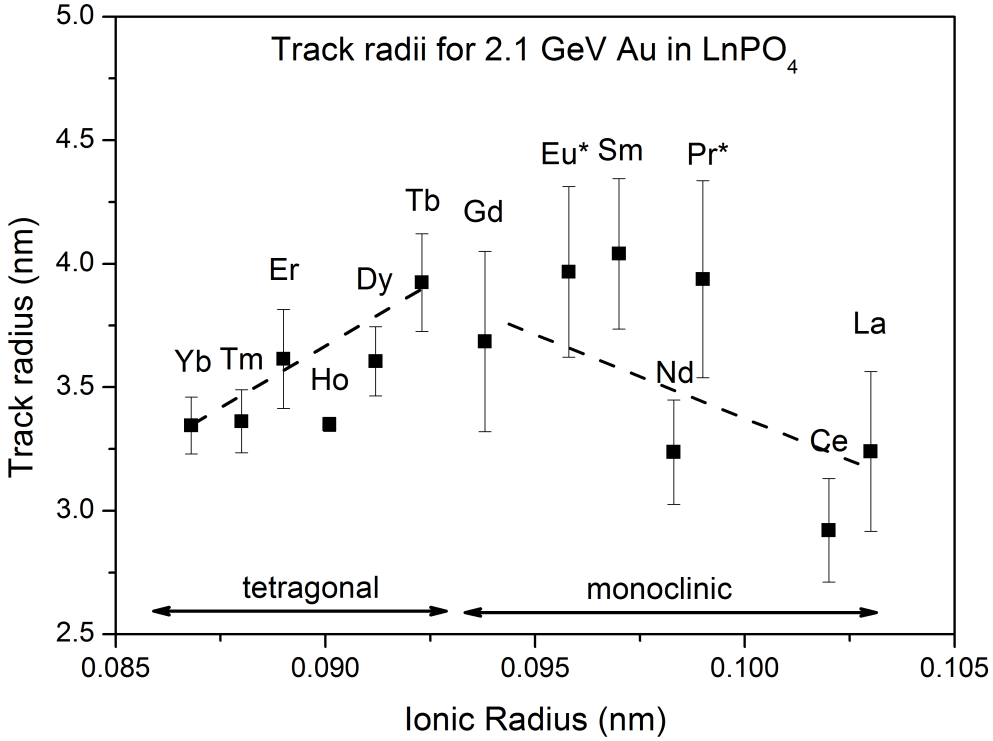

Figure 5.50: Track radii deduced from Raman spectra of $LnPO_4$ irradiated by 2.1 GeV Au ions up to $2{\times}10^{12}$ ions/cm^2. The Raman spectra were measured using a blue laser ($\lambda = 473.05\ nm$) for most materials. $EuPO_4$ and $PrPO_4$ were measured using a red laser light ($\lambda = 623.82\ nm$). The lines are guides for the eye.

The analysis of the track radii for 2.1 GeV Au ion in $LnPO_4$ shown on fig. 5.50 does not take into account the different energy deposition for Au ion in the particular sample. With the decrease of ionic radius, the density of the samples gradually increases (see table 3.1). The increase in the material density causes the 2.1 GeV Au ions to release more energy per unit of its path in $LuPO_4$ than it does in $LaPO_4$. To take into account the difference in the values of energy loss through the series of lanthanide phosphates, I have normalized the track radii to the peak value of the electronic stopping power for the 2.1 GeV Au ion for all $LnPO_4$. The results of this analysis are shown on fig. 5.51.

The normalization of the track radii to the corresponding electronic stopping powers diminishes the trend for the monoclinic phosphates and makes the observed slope steeper for the tetragonal phosphates.

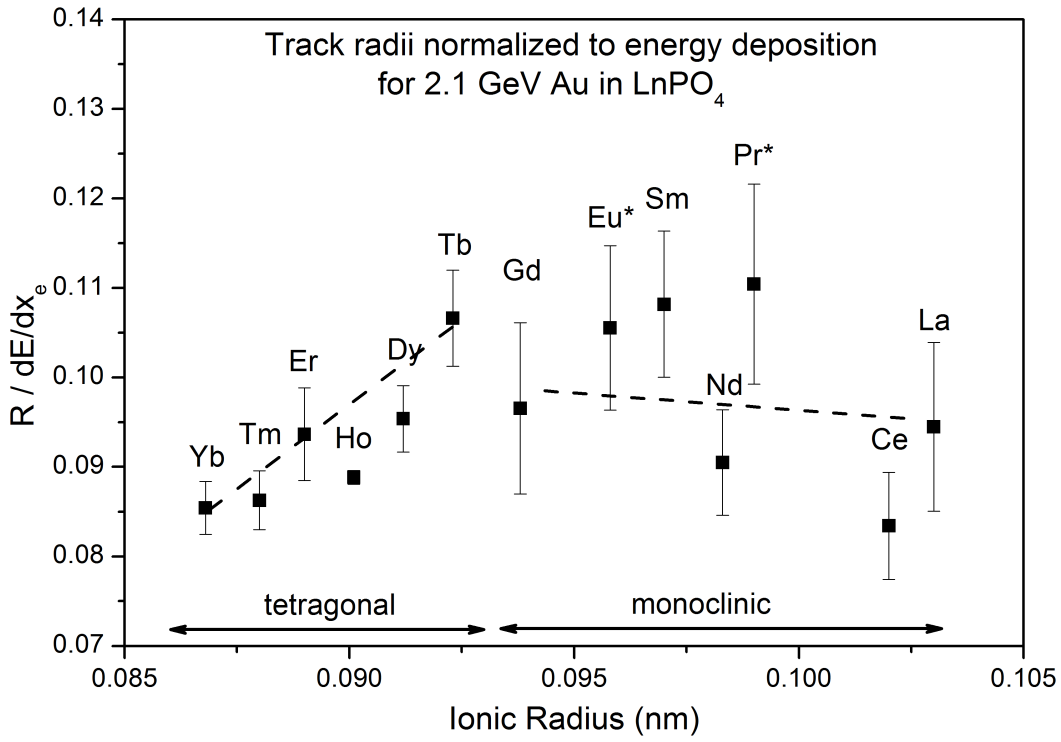

Figure 5.51: Track radii for 2.1 GeV Au ion in $LnPO_4$ normalized to energy deposition dE/dx. The lines are guides for the eye.

5.3.4 Discussion and conclusions

The Raman spectroscopy analysis of the radiation damage in both monoclinic and tetragonal $LnPO_4$ showed a strong degradation of Raman spectra with the increase of ion fluence for all rare earth phosphates. The decrease of sharp peaks accompanied by the increase of background and the appearance of a broad humps at the region around 970 cm^{-1} suggests that all rare earth phosphates could be successfully amorphized by the swift heavy ion beam. In the region of $(PO_4)^{3-}$ stretching modes a few broad peaks appear and progress in intensities with the irradiaion. For the most of compounds in this region a three broad Gaussian shaped peaks could be fit to the Raman data for the contribution of amorphous sample material. In the case of $HoPO_4$, only two Gaussian peaks are necessary to fit spectra. This could be linked to a special luminescent contribution present in the Raman spectra of $HoPO_4$ and the fact that it is the only material where background subtraction was done by the line with a certain tilt, whereas for the rest of compounds the horizontal line fit was sufficient.

Calculation of amorphization cross-sections and track radii for the series of samples irradiated by the Au ion beam up to various fluences showed, that precision of the Raman spectroscopy analysis is not enough to deduce any reliable trends of track radius variation depending on the composition. All the values for track radii scatter around 5 nm for all the studied phosphates except of YPO_4, where calculation of track radii was not possible due to the lack of experimental

data. Measurements performed on three monazite rare earth phosphates using small-angle X-ray scattering suggested the slight trend of a track radius increase with the increase of atomic number of rare earth cation. The values, however, overlap within as error bars. We should take into account, that the increase of electronic energy loss in this compounds also scales with the cation atomic number. All that suggests slight to no trend for track radius variation depending on the cation in the monazite group of $LnPO_4$. The Raman analysis of full series of rare earth phosphates irradiated up to the fluence of 2×10^{12} ions/cm^2 gave a hint for the track radius decrease with the increase of Ln atomic number. The accurate proof of this dependence requires additional experimental data, preferably combined with the other experimental techniques i.e. SAXS and TEM, and could not be done within this research.

5.4 Radiation damage in $LnPO_4$ depending on beam conditions

5.4.1 Flux effect in YPO_4 and $TmPO_4$

This section describes the response of YPO_4 and $TmPO_4$ samples to the ion beam in different flux regimes. The samples were irradiated with the Au ion beam (50 Hz repetition rate, 5 ms pulse length) using a flux of either 10^8 or 10^9 ions/cm^2·s up to a fluence of 5×10^{12} ions/cm^2. For the qualitative comparison of radiation damage, additional samples were irradiated up to 1×10^{13} ions/cm^2 (10^9 ions/cm^2·s flux). The used ion beam provides irradiation with the most homogeneous time distribution of ion-impact events over the sample volume (details are given in section 4.1).

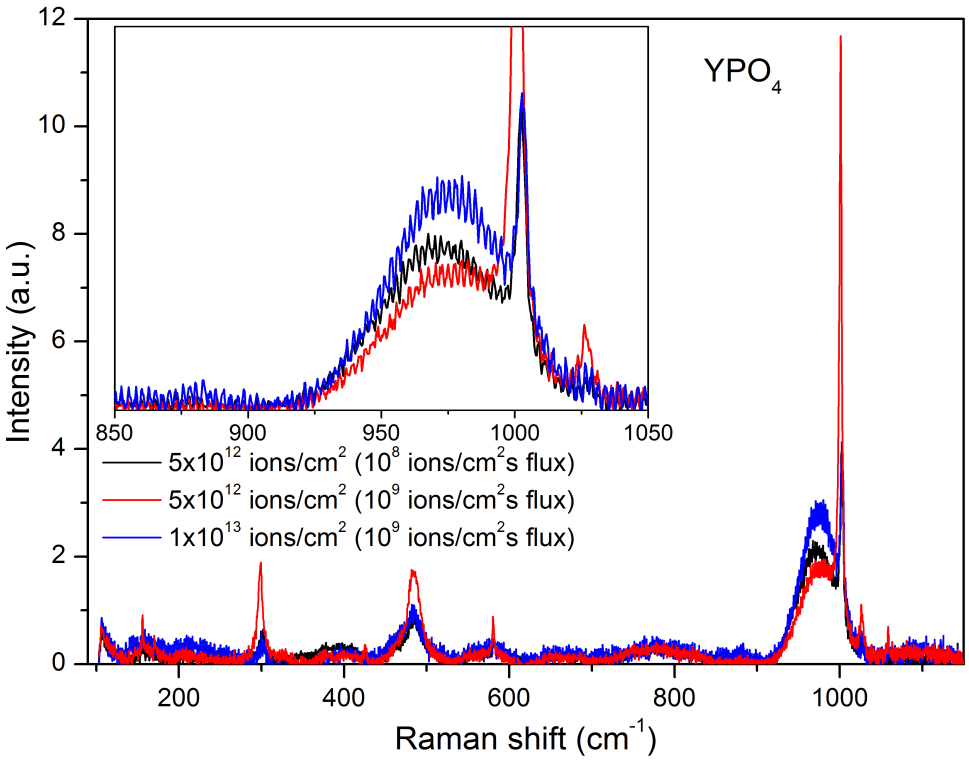

Figure 5.52: Flux effect in YPO_4 irradiatied by 2.1 GeV Au ions.

Figure 5.52 shows the Raman spectra of YPO_4 irradiatied by 2.1 GeV Au ions at different fluxes. The measurements were performed with a red laser (λ = 632.82 nm). Automatic background subtraction was used for all three spectra. All the typical radiation-induced changes, as discussed in the previous sections, can be observed in the Raman spectra: the decrease of the sharp Raman bands, the increase of the background, and the appearance of a broad hump around 970 $^{-1}$. The broad peak at 970 cm^{-1} is observed in all three spectra, however depends on the beam parameters. The sharp Raman peaks have the highest intensities for the sample with a fluence of 5×10^{12} ions/cm^2 irradiated with a flux of 10^9 ions/cm^2·s. Comparing

the three Raman spectra allows to draw the conclusion, that an increase of ion flux leads to partial annealing of radiation damage. This becomes evident when comparing the samples irradiated at a fluence of 5×10^{12} ions/cm^2 using different fluxes: the sample irradiated by a flux of 10^9 ions/cm^2·s has a less pronounced broad hump (indicating a lower fraction of amorphous material) and more intense sharp peaks (indicating a larger amount of remaining crystalline material) than the sample irradiated with a flux of 10^8 ions/cm^2·s. The YPO_4 sample irradiated up to 1×10^{13} ions/cm^2 with the higher flux (10^9 ions/cm^2·s) exhibits a slightly larger material degradation than sample irradiated up to 5×10^{12} ions/cm^2 with the lower flux (10^8 ions/cm^2·s).

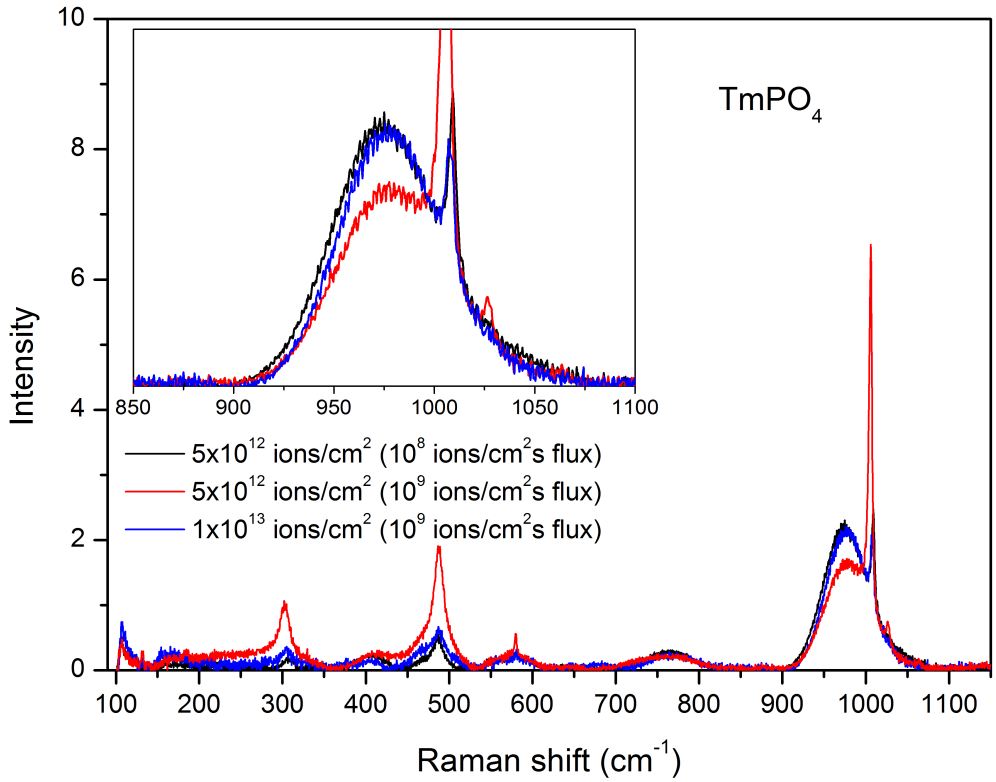

Figure 5.53: Flux effect in $TmPO_4$ irradiatied by 2.1 GeV Au ions.

The effect of a damage decrease with increasing ion flux is also observed for $TmPO_4$ irradiated by 2.1 GeV Au ions, presented on fig. 5.53. The measurement conditions and analysis of the Raman data were identical to YPO_4. We can observe that the increase of the ion flux leads to a decrease of the radiation damage in the sample. The Raman spectra of 5×10^{12} ions/cm^2 (10^8 ions/cm^2·s) and 1×10^{13} ions/cm^2 (10^9 ions/cm^2·s) samples in fact look so much alike, allowing the conclusion, that for the $TmPO_4$ sample an increase of the ion flux from 10^8 to 10^9 ions/cm^2·s doubles the required amount of impacting ions to produce the same damage in the material.

This flux effect observed in the YPO_4 and $TmPO_4$ samples is presumably linked to a temperature increase and partial defect annealing in the samples during the irradiation. The rare earth phosphates are known to have a relatively low recrystallization temperatures [84] and a

low thermal conductivity [85]. The ion beam induced temperature increase in the irradiated layer may lead to a defect annealing and recrystallization [86–88]. A more detailed analysis of this flux effect would require more experimental data with larger flux variations as well as maintaining of a macroscopic sample heating.

5.4.2 Response to the different ion beam pulse intensities

Several samples of rare earth phosphates (monoclinic $PrPO_4$, $SmPO_4$ and tetragonal YPO_4, $TmPO_4$) were irradiated by the Xe ion beams using two different pulse intensities. The total accumulated ion fluence for all samples reported in this section is the same: 1×10^{12} ions/cm^2. The high pulse intensity setting of the ion beam uses a flux of 1.8×10^{8} ions/cm^2·s with a repetition rate of 2 Hz and a pulse length of 0.2 ms, leading to a beam intensity of 0.9×10^{8} ions/cm^2 per pulse. The low pulse intensity setting of the ion beam uses a flux of 3.2×10^{8} ions/cm^2·s with a repetition rate of 5 Hz and a pulse length of 1 ms, leading to a beam intensity of about 0.6×10^{8} ions/cm^2 per pulse. The Xe ions in both cases had a total energy of 1.5 GeV (specific energy equal to 11.1 MeV/u).

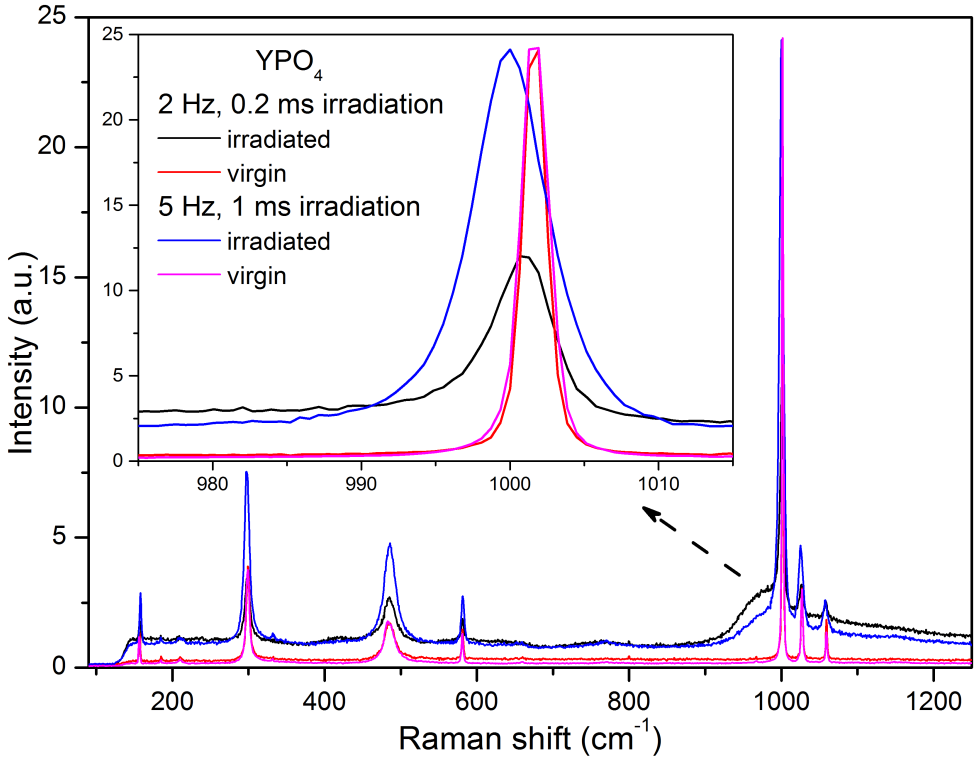

Figure 5.54: YPO_4 irradiatied at 1×10^{12} ions/cm^2 by 1.5 GeV Xe ions using a low repetition rate coupled with a low pulse intensity (5 Hz, 1 ms) and a low repetition rate coupled with a high pulse intensity (2 Hz, 0.2 ms) ion beams.

A detailed description of the irradiation conditions and beam pulse structures is discussed in section 4.1. For each irradiated sample the Raman spectra were measured in two positions.

First measurement was performed close to the irradiated surface within the ion range, while the second one was done far away from the irradiated surface. That made a crystal orientation being identical for both Raman measurements. It allows a comparison of the Raman spectra for the damaged and virgin crystalline material. The Raman spectra were taken using a blue laser (λ = 473.05 nm) for the YPO_4, $TmPO_4$ and $SmPO_4$ samples. $PrPO_4$ was measured using a red laser (λ = 632.82 nm) due to a large fluorescence caused by the blue laser light (see fig. 3.7). During the discussion of the material response to the ion irradiation in this section I will neglect the difference in overall flux between beams of 3.2×10^8 and 1.8×10^8 ions/cm^2·s. The possible flux effects discussed in the section 5.4.1 are considered to be negligible here due to the small difference in flux values.

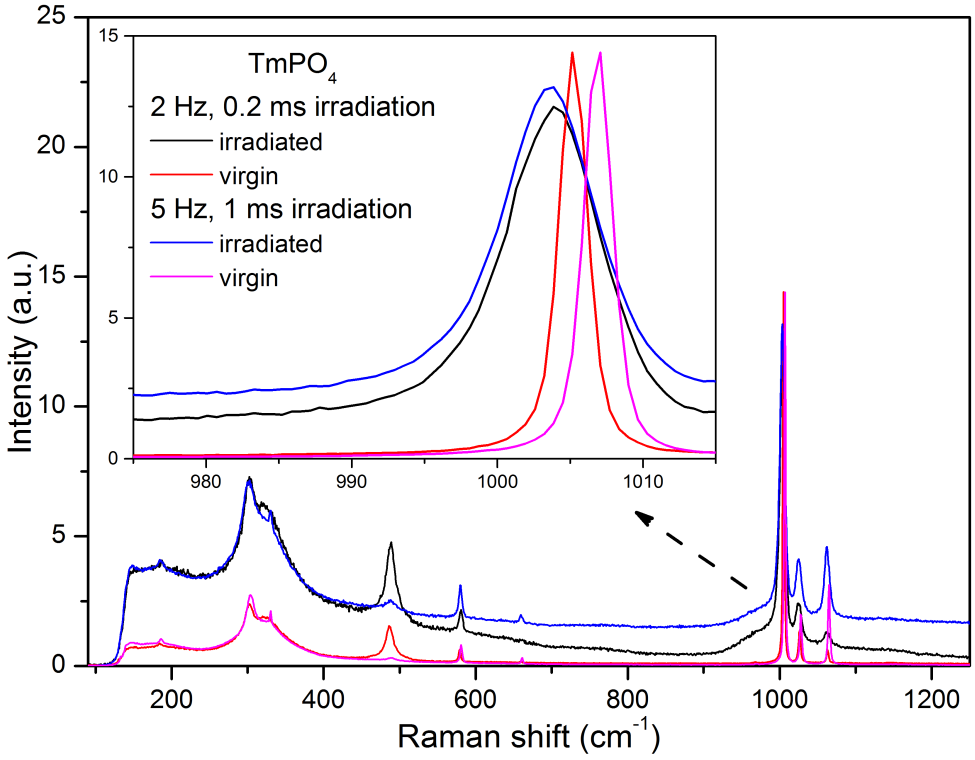

Figure 5.55: $TmPO_4$ irradiatied at 1×10^{12} ions/cm^2 by 1.5 GeV Xe ions using low repetition rate coupled with a low pulse intensity (5 Hz, 1 ms) and low repetition rate coupled with a high pulse intensity (2 Hz, 0.2 ms) ion beams.

Figure 5.54 shows the results of the Raman spectroscopy measurements of YPO_4 samples irradiated by Xe ion beams of two different beam structures: 2 Hz, 0.2 ms and 5 Hz, 1 ms. The first feature that could be observed, is the increase in intensity of the broad hump at 970 cm^{-1} for the high pulse intensity beam (2 Hz, 0.2 ms). This increase is accompanied by the decrease of all sharp bands attributed to the crystalline material fraction. This indicates an increased amorphous fraction when irradiating with the high pulse intensity beam in comparison with the low pulse intensity (5 Hz, 1 ms) Xe beam. The Raman peak positions in the irradiated samples in comparison with virgin crystals also suggest different values of relative Raman peak shifts for

particular irradiation conditions. The sample irradiated with the 2 Hz, 0.2 ms beam produces a Raman peak of the symmetric stretching mode (peak at 1001 cm^{-1}) with lower intensity, however less shifted to lower values than the sample exposed to the 5 Hz, 1 ms ion beam.

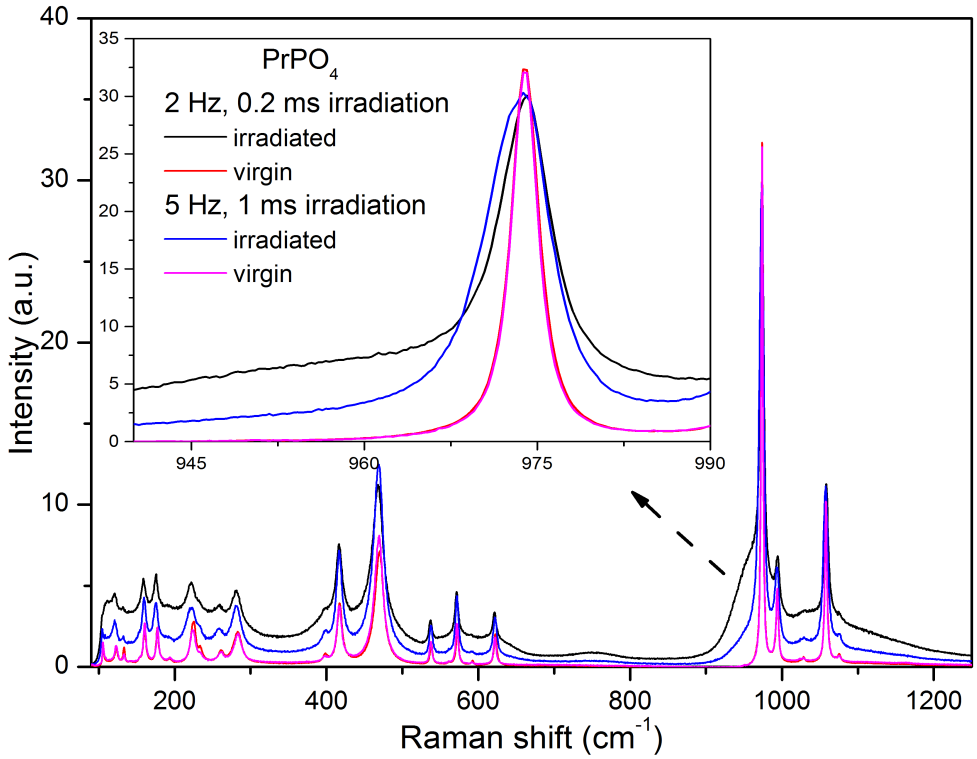

Figure 5.56: $PrPO_4$ irradiatied at 1×10^{12} ions/cm^2 by 1.5 GeV Xe ions using low repetition rate coupled with a low pulse intensity (5 Hz, 1 ms) and low repetition rate coupled with a high pulse intensity (2 Hz, 0.2 ms) ion beams.

This trend of the broad amorphous hump beeing more pronounced in the Raman spectra of the samples irradiated by the high pulse intensity beam persists through all irradiated samples of both tetragonal and monoclinic structures. In addition, for all samples the Raman peak shift of the symmetric stretching mode to the lower wavelength is always more distinct for the low pulse intensity beam. For $TmPO_4$ (fig. 5.55) in the Raman spectra the absolute positions of the symmetric stretching mode seem to be identical for both irradiations, however the shift relative to the corresponding virgin sample is significantly different (the shift of the absolute Raman peak positions here is an artifact of the instrument calibration). A very similar behavior could be observed in the Raman spectra of monoclinic $PrPO_4$ (fig. 5.56) and $SmPO_4$ (fig. 5.57). For the monoclinic phosphates, the shifts of the Raman peaks are slightly lower, but the increase of the broad hump intensity and decrease of sharp bands is still obvious.

In section 5.2.4 the shift of the Raman peaks was discussed and related to the formation of a defect halo around the amorphous track. I have also suggested the possibility of a partial defect recombination in the overlapping halos of the ion tracks (see fig. 5.21). This understanding of the damage formation could be extended to explain the difference in the material response to

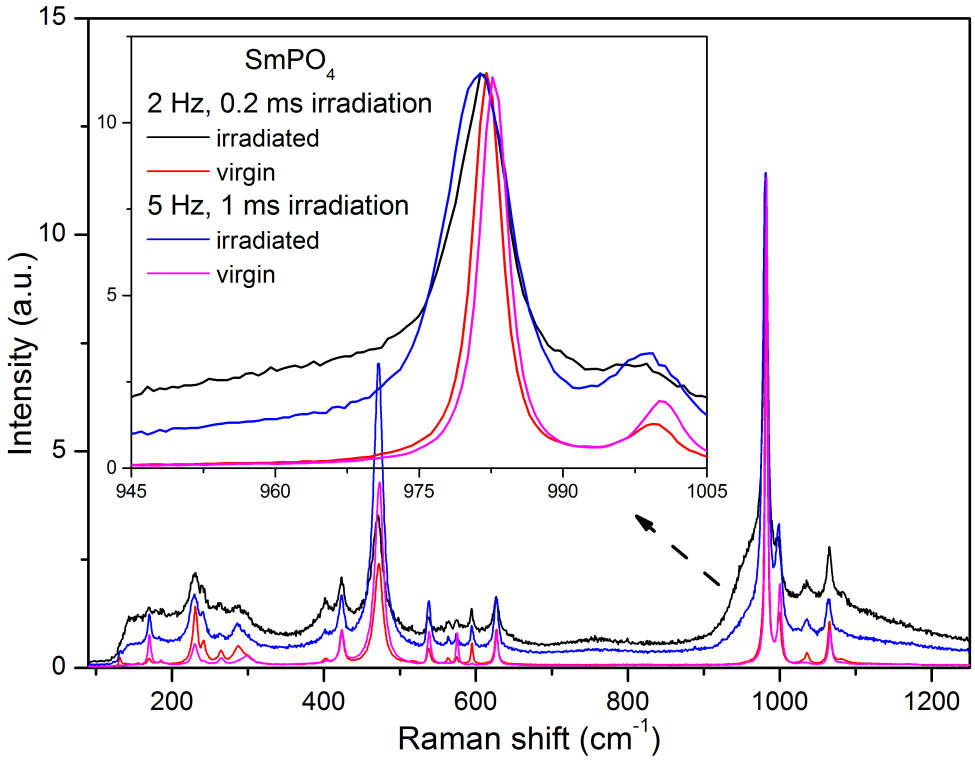

Figure 5.57: $SmPO_4$ irradiatied at 1×10^{12} ions/cm^2 by 1.5 GeV Xe ions using low repetition rate coupled with a low pulse intensity (5 Hz, 1 ms) and low repetition rate coupled with a high pulse intensity (2 Hz, 0.2 ms) ion beams.

the various ion beam pulse intensities. During the low pulse intensity irradiation we assume that in the particular sample volume a simultaneous overlap of ion tracks formed by several impacting projectiles never happens. In this case, the succeeding ion provides additional energy to induce partial damage recovery within the halo left from the previous impact. During the irradiation with the high pulse intensity we increase the chance of two or more simultaneous ion hits in adjacent regions (track overlapping during the ion impacts). The aggregated energy within an overlapping excitation cascades is enough to transform the sample material into an amorphous state. The decrease of material amount within the defected halos can be observed in Raman spectra as a smaller shift of the peaks position towards lower wavenumbers, whereas the larger amorphous volume increases the intensity in the broad hump in the spectra.

We can try to estimate the probability of the event of the material amorphization due to the simultaneous energy deposition from the impact of two or more ions. We immediately face the lack of a theoretical description and calculations of the electronic structure of rare earth phosphates. In the literature there are the estimations of radial electron distribution after the ionization in LiF [89] and diamond [90]. The radial distribution of the electron excitation could possibly reach a micrometer scale. However, taking into account that a simultaneous ionization produced by two or more different ions requires a time difference between impacts

to be below 10^{-12} s, it is questionable if this can happen with a sufficient probability, at least in the straightforward way that was previously suggested.

A flux effect by itself is reported in the literature both in the sense of flux-induced macroscopic temperature increase, and in the observation of complex defect formation due to an overlap of damage cascades from different ions [91]. A better understanding of the physical phenomena that appear during the irradiations with the intense pulsed ion beams requires both the accumulation of more experimental data as well as the development of a theoretical understanding of ion irradiation-induced damage formation.

5.4.3 Discussion and conclusions

In this section I have shown that detailed consideration of material degradation by shift heavy ion irradiation should take into account not only a total amount of accumulated ions (fluence), but also a rate (flux) at which this fluence was accumulated. Raman spectroscopy analysis of YPO_4 and $TmPO_4$ samples irradiated by 2.1 GeV Au ions have shown that increase of ion flux leads to partial damage annealing, most likely due to the macroscopic temperature increase of samples during the irradiation. In addition to the beam flux, an ion beam substructure was found to play crucial role in the amount of produced amorphization. YPO_4, $TmPO_4$, $PrPO_4$ and $SmPO_4$ samples were irradiated by the two kinds of Xe beam. The first provided a 1 ms long low intensity pulses with the repetition rate of 5 Hz with the total flux of 3.2×10^8 ions/cm$^2\cdot s$. The other beam had high intensity 0.2 ms pulses with the repetition rate of 2 Hz and total flux of 1.8×10^8 ions/cm$^2\cdot s$. For all the samples amount of amorphous material was found to be greater in the case of high pulse intensity beam. Further analysis of Raman data suggests that possible explanation or increased amorphous fraction for the pulsed ion beam could be induced by the mechanism of amorphization in the overlapping excitation cascades of different ions that were provided simultaneously to the sample.

6 Conclusions and outlook

Series of single-crystal rare earth phosphates ($REEPO_4$) were exposed to energetic heavy ion beams. After the irradiation with 2.1 GeV Au ions of fluence between 5×10^{11} and 5×10^{13} ions/cm^2, all samples experienced significant structural changes. That affected both macroscopic material properties producing visible specimen transformation, as well as amorphization that was observed and quantified by different experimental techniques. Sample fracturing, cracking, swelling and coloration lead to the direct observation of radiation-induced modifications. Stress created at the interface between the irradiated and nonirradiated material results in severe sample embrittlement. Amorphization of rare earth phosphates was studied mainly by the Raman spectroscopy. The evolution of the Raman spectra of irradiated monoclinic $NdPO_4$ and tetragonal $HoPO_4$ were analyzed as a function of ion fluence in order to determine amorphization cross sections for 2.1 GeV Au ions in both samples. The intensity of all sharp Raman peaks that existed in the virgin spectra were found to gradually decrease with the irradiation and completely vanish at a fluence of 1×10^{13} ions/cm^2. Luminescence present in the Raman spectra of virgin crystals also quickly disappeared when increasing the ion fluence. Amorphous background and broad hump at the region of the $(PO_4)^{3-}$ symmetric stretching modes are the only features in the Raman spectra of completely amorphized rare earth phosphates. Taking the ratio of a broad hump to the area of the corresponding symmetric stretching mode was the first approach used for quantification of the amorphous fraction at certain fluence step. This technique produced data that did not follow theoretical predictions for the direct impact amorphization process, and the deduced track radii did not match the results obtained by other experimental techniques (SAXS and TEM). The second approach consisted of rescaling the Raman spectra and taking into consideration only sharp Raman peaks. This method yielded significantly better results and predicted track radii close to 5.0 nm for both compounds. Further Raman investigations of $NdPO_4$ and $HoPO_4$ found an unusual dependence of a radiation-induced change of the position and width of the Raman bands. The Raman peak width for $NdPO_4$ tends to increase for the first fluence step of 5×10^{11} ions/cm^2 and then shrinks at larger fluences. In the case of $HoPO_4$ the Raman peak width increases up to 1×10^{12} ions/cm^2 and shrinks at subsequent irradiation steps. Similar behavior was observed for the Raman peak position consisting of an initial shift of the Raman peaks to lower wavenumbers followed by a shift of all peaks to higher values of Raman shift. This behavior is explained by the existence of a defect halo around the amorphous ion track. Calculation for $HoPO_4$ suggests the halo radius to be around 6.4 nm. Raman spectra measured along the ion trajectories supported the idea of electronic stopping power playing a dominant role in the damage production during the swift

heavy ion irradiation. Raman spectroscopy analysis was performed on a series of monoclinic and tetragonal phosphates with the purpose to test whether there exists a dependence of the track radius from the rare earth cation. Both Raman and small-angle X-ray spectroscopy data suggests little or no dependency of track radii for 2.1 GeV Au ions in monoclinic phosphates ([Nd,Pr,Sm,Eu]PO_4) and small increase of track radii from $NdPO_4$ to $EuPO_4$ could be explained by the density variation. Raman spectroscopy analysis of tetragonal phosphates suggests a slight trend of decreasing track radius with increasing REE atomic number. However, the precision of the Raman analysis is not sufficiently high and such possible trend requires further confirmation. In addition, the influence of ion beam parameters on the produced radiation damage was tested. The increase of the Au ion flux from 10^8 to 10^9 ions/cm^2·s was shown to induce partial damage recovery, most likely due to macroscopic sample heating. The irradiation of several monoclinic and tetragonal phosphates with Xe ions allowed studying of material degradation depending on the pulse intensity of the beam. Samples were irradiated with Xe ions of low repetition rate and high pulse intensity (2 Hz, 0.2 ms, flux 1.8×10^8 ions/cm^2·s), and low repetition rate and low pulse intensity (5 Hz, 1 ms, flux 3.2×10^8 ions/cm^2·s). For all studied rare earth phosphates samples irradiated up to exactly the same fluences, the high pulse intensity has shown to produce larger amorphization in comparison to low pulse intensity beam. This work opens a window for more reliable quantitative Raman spectroscopy analysis of radiation damage by proposing an alternative way of spectra analysis. Nevertheless, the uncertainty in the fluence determination and variation of sample orientation calls for on-line measurements of radiation damage with the full control of measurement geometry and stable position of measurement spot. Interesting extension of the presented work would be the irradiation with different ions to vary the electronic energy loss and determine the threshold for track formation. The results also demonstrate that beam parameters such as flux and pulse intensity play a crucial role for the radiation damage production. That is why the control of these parameters during irradiations and systematic research with their variation is necessary for the improvement of predictive capability of material degradation under particular irradiation conditions. The existence of a defect halo has to be confirmed with additional experimental techniques and ideally quantified in size or volume. High resolution TEM could help in the direct observation of the defect area around the amorphous track and halo size estimation.

Acknowledgements

I would like to express my sincerest gratitude to everybody who encouraged, supported me or has just been around during my PhD times.

- My Doctormutter Prof. Christina Trautmann for inviting me to Germany and for taking care of me in my rough times. Frankly speaking, I even don't know what I would do without you!
- My Doktorvater Prof. Franz Fujara for incredible support and for the quite extensive discussions during my presentations.
- Prof. Maik Lang for bringing me to the current scientific topic, for the fruitful discussions and simply for my wonderful USA trip.
- Dr. Marilena Tomut for being a very good friend and companion.
- Dr. Christian Hubert and all Hubert's family for being and awesome friends and just incredible people.
- Special thanks to everybody who has been with me on a beamtime. Separate greeting to you because we got a bit closer during that countless sleepless nights, so each of you left a small scar in my heart.
- All the GSI Materialforschung group for being good colleagues, friends and very noisy people, by the way!
- Additional greeting to the Russian-speaking community of our group: Liana Movsesyan and Alexei Prosvetov.
- Greeting also to the members of AG Fujara as I become good friend with many of them.
- Dr. Siegfried Klaumünzer for the help with XRD, for brilliant discussion on the various scientific topics.
- Prof. Patrick Kluth and Dr. Daniel Schauries for the SAXS measurements.
- Dr. Dominic Vogt for SEM measurements.
- Dr. Joachim Brötz for XRD measurements.
- Dr. Weixing Li for TEM measurements.

- Prof. Rodney C. Ewing for inviting me to the USA.
- Prof. Udo Becker for AFM measurements.
- My main support during all the time, Olena Lenchuk. I cannot even express by words everything I need to say to you.
- My second main support - my parents and my grandma. I simply love you and I hope I make you proud of me at least a bit.

Bibliography

[1] R. C. Ewing, The nuclear fuel cycle: A role for mineralogy and geochemistry, Elements 2 (2006) 331–334.

[2] P. Burgherr, P. Eckle, S. Hirschberg, E. Cazzoli, Report on Severe Accident Risk Including Key Indicators. Project No 213744, available on PSI website), accessed 20.03.16.

[3] W. Schenler, S. Hirschberg, P. Burgherr, M. Makowski and J. Granat, Final Report on Sustainability Assessment of Advanced Electricity Supply Options. Project No 502687, available on PSI website, accessed 20.03.16..

[4] R. Grover, Green growth and role of nuclear power: A perspective from India, Energy Strategy Reviews 1 (2013) 255 – 260. Nuclear Energy Today & Strategies for Tomorrow.

[5] "Radioactive waste management" (Updated October 2015), article from the website of World Nuclear Association, accessed 13.04.16.

[6] J. Bruno, R. C. Ewing, Spent nuclear fuel, Elements 2 (2006) 343–349.

[7] R. C. Ewing, L. Wang, Phosphates as nuclear waste forms, Reviews in Mineralogy and Geochemistry 48 (2002) 673–699.

[8] R. C. Ewing, Nuclear waste forms for actinides, Proceedings of the National Academy of Sciences 96 (1999) 3432–3439.

[9] R. C. Ewing, Ceramic matrices for plutonium disposition, Progress in Nuclear Energy 49 (2007) 635 – 643. Options for the Long-Term Management of Separated Plutonium.

[10] R. C. Ewing, Safe management of actinides in the nuclear fuel cycle: Role of mineralogy, Comptes Rendus Geoscience 343 (2011) 219 – 229.

[11] R. Ewing, The design and evaluation of nuclear-waste forms: clues from mineralogy, The Canadian Mineralogist 39 (2001) 697–715.

[12] A. Meldrum, L. Boatner, L. Wang, R. Ewing, Ion-beam-induced amorphization of $LaPO_4$ and $ScPO_4$, Nuclear Instruments and Methods in Physics Research B 127/128 (1997) 160–165.

[13] E. Oelkers, J.-M. Montel, Phosphates and Nuclear Waste Storage, Elements 4 (2008) 113–116.

[14] F. Karioris, K. A. Gowda, L. Cartz, J. Labbe, Damage cross-sections of heavy ions in crystal structures, Journal of Nuclear Materials 108 (1982) 748 – 750.

[15] A. Meldrum, L. Boatner, R. Ewing, Displacive radiation effects in the monazite- and zircon-structure orthophosphates, Physical Review B 56 (1997) 13805–13814.

[16] W. J. Weber, D. M. Duffy, L. Thomé, Y. Zhang, The role of electronic energy loss in ion beam modification of materials, Current Opinion in Solid State and Materials Science 19 (2015) 1 – 11. Ion Beam Modification of Materials.

[17] A. E. Grechanovsky, A. B. Brik, O. M. Ponomarenko, Influence of structure, character of chemical bonding and elastic properties on the radiation stability of silicates, phosphates and metal oxides deduced by computer simulations, Mineralogical Journal (Ukraine) 31 (2009) 30 – 37.

[18] K. Trachenko, Understanding resistance to amorphization by radiation damage, Journal of Physics: Condensed Matter 16 (2004) R1491–R1515.

[19] K. Nordlund, A. E. Sand, F. Granberg, S. J. Zinkle, R. Stoller, R. S. Averback, T. Suzudo, L. Malerba, F. Banhart, W. J. Weber, F. Willaime, S. Dudarev, D. Simeone, Primary Radiation Damage in Materials, Technical Report NEA/NSC/DOC(2015)9, Report prepared by the OECD/NEA Working Party on Multiscale Modelling of Fuels and Structural Materials for Nuclear Systems, Expert Group on Primary Radiation Damage, 2015.

[20] N. Itoh, D. M. Duffy, S. Khakshouri, A. M. Stoneham, Making tracks: electronic excitation roles in forming swift heavy ion tracks, Journal of Physics: Condensed Matter 21 (2009) 474205.

[21] D. Schauries, M. Lang, O. H. Pakarinen, S. Botis, B. Afra, M. D. Rodriguez, F. Djurabekova, K. Nordlund, D. Severin, M. Bender, W. X. Li, C. Trautmann, R. C. Ewing, N. Kirby, P. Kluth, Temperature dependence of ion track formation in quartz and apatite, Journal of Applied Crystallography 46 (2013) 1558–1563.

[22] O. H. Pakarinen, F. Djurabekova, K. Nordlund, Density evolution in formation of swift heavy ion tracks in insulators, Nuclear Instruments and Methods in Physics Research Section B: Beam Interactions with Materials and Atoms 268 (2010) 3163 – 3166. Proceedings of the 15th International Conference on Radiation Effects in Insulators (REI).

[23] W. Li, M. Lang, A. Gleadow, M. Zdorovets, R. Ewing, Thermal annealing of unetched fission tracks in apatite, Earth and Planetary Science Letters 321 - 322 (2012) 121 – 127.

[24] E. Enkelmann, R. Jonckheere, L. Ratschbacher, The effects of radiation damage accumulation and annealing on fission-track dating of titanite, Nuclear Instruments and Methods in

Physics Research Section B: Beam Interactions with Materials and Atoms 227 (2005) 567 – 576.

[25] M. Lang, F. Zhang, W. Li, D. Severin, M. Bender, S. Klaumünzer, C. Trautmann, R. Ewing, Swift heavy ion-induced amorphization of $CaZrO_3$ perovskite, Nuclear Instruments and Methods in Physics Research Section B: Beam Interactions with Materials and Atoms 286 (2012) 271 – 276. Proceedings of the Sixteenth International Conference on Radiation Effects in Insulators (REI).

[26] G. Sattonnay, N. Sellami, L. Thomé, C. Legros, C. Grygiel, I. Monnet, J. Jagielski, I. Jozwik-Biala, P. Simon, Structural stability of $Nd_2Zr_2O_7$ pyrochlore ion-irradiated in a broad energy range, Acta Materialia 61 (2013) 6492–6505.

[27] I. Jozwik-Biala, J. Jagielski, B. Arey, L. Kovarik, G. Sattonnay, A. Debelle, S. Mylonas, I. Monnet, L. Thomé, Effect of combined local variations in elastic and inelastic energy losses on the morphology of tracks in ion-irradiated materials, Acta Materialia 61 (2013) 4669 – 4675.

[28] M. Lang, M. Toulemonde, J. Zhang, F. Zhang, C. Tracy, J. Lian, Z. Wang, W. Weber, D. Severin, M. Bender, C. Trautmann, R. Ewing, Swift heavy ion track formation in $Gd_2Zr_{2-x}Ti_xO_7$ pyrochlore: Effect of electronic energy loss, Nuclear Instruments and Methods in Physics Research Section B 336 (2014) 102–115.

[29] K. Schwartz, A. Volkov, K.-O. Voss, M. Sorokin, C. Trautmann, R. Neumann, Thermal spike effect on defect evolution in NaCl irradiated with light and heavy ions at 8 and 300 K, Nuclear Instruments and Methods in Physics Research Section B: Beam Interactions with Materials and Atoms 245 (2006) 204 – 209. Proceedings of the Sixth International Symposium on Swift Heavy Ions in Matter (SHIM 2005).

[30] M. A. Rana, Mechanisms and kinetics of nuclear track etching and annealing: Free energy analysis of damage in fission fragment tracks, Nuclear Instruments and Methods in Physics Research Section A: Accelerators, Spectrometers, Detectors and Associated Equipment 672 (2012) 57 – 63.

[31] M. Lang, F. Zhang, J. Zhang, J. Wang, J. Lian, W. J. Weber, B. Schuster, C. Trautmann, R. Neumann, R. C. Ewing, Review of $A_2B_2O_7$ pyrochlore response to irradiation and pressure, Nuclear Instruments and Methods in Physics Research Section B: Beam Interactions with Materials and Atoms 268 (2010) 2951 – 2959. Proceedings of the 15th International Conference on Radiation Effects in Insulators (REI).

[32] E. A. Kenik, J. T. Busby, Radiation-induced degradation of stainless steel light water reactor internals, Materials Science and Engineering: R: Reports 73 (2012) 67 – 83.

[33] D. L. Fillmore, Literature Review of the Effects of Radiation and Temperature on the Aging of Concrete, 2004.

[34] K. Trachenko, E. Zarkadoula, I. Todorov, M. Dove, D. Dunstan, K. Nordlund, Modeling high-energy radiation damage in nuclear and fusion applications, Nuclear Instruments and Methods in Physics Research Section B: Beam Interactions with Materials and Atoms 277 (2012) 6 – 13. Basic Research on Ionic-Covalent Materials for Nuclear Applications.

[35] J. F. Ziegler, M. D. Ziegler, J. P. Biersack, SRIM - The stopping and range of ions in matter (2010), Nuclear Instruments and Methods in Physics Research B 268 (2010) 1818–1823.

[36] P. Sigmund, Particle Penetration and Radiation Effects: General Aspects and Stopping of Swift Point Charges, Springer-Verlag Berlin Heidelberg, Berlin Heidelberg, 2006.

[37] R. L. Fleisher, P. B. Price, R. M. Walker, Nuclear tracks in solids: Principles and applications, 1975.

[38] M. Toulemonde, C. Dufour, A. Meftah, E. Paumier, Transient thermal processes in heavy ion irradiation of crystalline inorganic insulators, Nuclear Instruments and Methods in Physics Research Section B: Beam Interactions with Materials and Atoms 166 - 167 (2000) 903 – 912.

[39] R. L. Fleischer, P. B. Price, R. M. Walker, E. L. Hubbard, Criterion for registration in dielectric track detectors, Physical Review 156 (1967) 353–355.

[40] R. Spohr, Ion Tracks and Microtechnology, Vieweg & Sohn Verlagsgesellschaft mbH, Braunschweig, 1990.

[41] S. Klaumünzer, M.-d. Hou, G. Schumacher, Coulomb explosions in a metallic glass due to the passage of fast heavy ions?, Physical Review Letter 57 (1986) 850–853.

[42] M. Toulemonde, E. Paumier, C. Dufour, Thermal spike model in the electronic stopping power regime, Radiation Effects and Defects in Solids 126 (1993) 201–206.

[43] M. Lang, R. Devanathan, M. Toulemonde, C. Trautmann, Advances in understanding of swift heavy-ion tracks in complex ceramics, Current Opinion in Solid State and Materials Science 19 (2015) 39–48.

[44] Klaumünzer, S.: Thermal-spike models for ion track physics: A critical examination. Matematisk-Fysiske Meddelelser 52, 293-328, 2006.

[45] R. Ewing, W. Weber, F. Clinard Jr, Radiation effects in nuclear waste forms for high-level radioactive waste, Progress in Nuclear Energy 29 (1995) 63 – 127.

[46] R. Ewing, L. Wang, Phosphates as Nuclear Waste Forms, Reviews in Mineralogy and Geochemistry 48 (2002) 673–699.

[47] R. Ewing, Nuclear waste forms for actinides, Proceedings of the National Academy of Sciences 96 (1999) 3432–3439.

[48] K. Momma, F. Izumi, *VESTA3* for three-dimensional visualization of crystal, volumetric and morphology data, Journal of Applied Crystallography 44 (2011) 1272–1276.

[49] Y. Ni, J. Hughes, A. Mariano, Crystal chemistry of the monazite and xenotime structures, American Mineralogist 80 (1995) 21–26.

[50] R. Feigelson, Synthesis and Single-Crystal Growth of Rare-Earth Orthophosphates, Journal of the American Ceramic Society 47 (1964) 257–258.

[51] L. Boatner, B. Sales, Radioactive Waste Forms for the Future. W. Lutze and R.C. Ewing, Eds., North-Holland Physics Publishing, Amsterdam, Netherlands, 1988.

[52] S. Ushakov, K. Helean, A. Navrotsky, L. Boatner, Thermochemistry of rare-earth orthophosphates, Journal of Materials Research 16 (2001) 2623–2633.

[53] E. Catlos, Generalizations about monazite: Implications for geochronologic studies, American Mineralogist 98 (2013) 819–832.

[54] G. Begun, G. Beall, L. Boatner, W. Gregor, Raman spectra of the Rare Earth Orthophosphates, Journal of Raman Spectroscopy 11 (1981) 273–278.

[55] E. Silva, A. Ayala, I. Guedes, C. Paschoal, R. Moreira, C.-K. Loong, L. Boatner, Vibrational spectra of monazite-type rare-earth orthophosphates, Optical Materials 29 (2006) 224 – 230.

[56] M. Poloznikova, V. Fomichev, The vibrational spectra and characteristic features of the orthophosphates of Group I-III elements, Russian Chemical Reviews 63 (1994) 399.

[57] E. R. Vance, K. K. S. Pillay, Fission fragment damage in crystalline phases possibly formed in solidified radioactive waste, Radiation Effects 62 (1982) 25–38.

[58] V. Picot, X. Deschanels, S. Peuget, B. Glorieux, A. Seydoux-Guillaume, R. Wirth, Ion beam radiation effects in monazite, Journal of Nuclear Materials 381 (2008) 290 – 296.

[59] L. Nasdala, R. Grötzschel, S. Probst, B. Bleisteiner, Irradiation damage in monazite-(ce): An example to establish the limits of Raman confocality and depth resolution, The Canadian Mineralogist 48 (2010) 351–359.

[60] https://www.gsi.de/start/aktuelles.htm, accessed 15.12.16.

[61] P. Spädtke, J. Bossler, H. Emig, K. Leible, C. Mühle, H. Schulte, K. Tinschert, Ion sources for accelerators, Nuclear Instruments and Methods in Physics Research Section B: Beam Interactions with Materials and Atoms 139 (1998) 145 – 149.

[62] Proceedings of IPAC2015, Richmond, VA, USA (IPAC 2015), volume 4: Hadron Accelerators of *A08 - Linear Accelerators*, 2015.

[63] K. Kupka, M. Tomut, P. Simon, C. Hubert, A. Romanenko, B. Lommel, C. Trautmann, Intense heavy ion beam-induced temperature effects in carbon-based stripper foils, Journal of Radioanalytical and Nuclear Chemistry 305 (2015) 875–882.

[64] S. Dedera, M. Burchard, U. A. Glasmacher, N. Schöppner, C. Trautmann, D. Severin, A. Romanenko, C. Hubert, On-line raman spectroscopy of calcite and malachite during irradiation with swift heavy ions, Nuclear Instruments and Methods in Physics Research Section B: Beam Interactions with Materials and Atoms 365, Part B (2015) 564 – 568. Swift Heavy Ions in Matter, 18 - 21 May, 2015, Darmstadt, Germany.

[65] W. Bolse, S. Amirthapandian, F. Schuchart, A new high-resolution scanning electron microscope for the in-situ investigation of ion beam modifications of solid surfaces, Verhandlungen der Deutschen Physikalischen Gesellschaft (2010) 045103.

[66] O. Baake, T. Seidl, U. H. Hossain, A. O. Delgado, M. Bender, D. Severin, W. Ensinger, An apparatus for in situ spectroscopy of radiation damage of polymers by bombardment with high-energy heavy ions, Review of Scientific Instruments 82 (2011) 045103.

[67] X. C. Tong, Advanced Materials for Integrated Optical Waveguides, volume 46 of *Springer Series in Advanced Microelectronics*, 1 ed., Springer International Publishing, Springer International Publishing Switzerland, 2014.

[68] D. Severin, Talk at CARAT Workshop at GSI, Darmstadt, http://www-carat.gsi.de/CARAT01/CARAT01Talks/Severin.pdf, accessed 13.04.16.

[69] S. Park, M. Lang, C. L. Tracy, J. Zhang, F. Zhang, C. Trautmann, P. Kluth, M. D. Rodriguez, R. C. Ewing, Swift heavy ion irradiation-induced amorphization of $La_2Ti_2O_7$, Nuclear Instruments and Methods in Physics Research Section B: Beam Interactions with Materials and Atoms 326 (2014) 145 – 149. 17th International Conference on Radiation Effects in Insulators (REI).

[70] Dimension FastScan AFM system, brochure from Brucker Website, https://cmi.epfl.ch/metrology/files/AFM/fastscan.pdf, accessed 20.06.16.

[71] W. Weber, Models and mechanisms of irradiation-induced amorphization in ceramics, Nuclear Instruments and Methods in Physics Research B 166-167 (2000) 98–106.

[72] M. Wojdyr, *Fityk*: a general-purpose peak fitting program, Journal of Applied Crystallography 43 (2010) 1126–1128.

[73] C. Hubert, K. O. Voss, M. Bender, K. Kupka, A. Romanenko, D. Severin, C. Trautmann, M. Tomut, Swift heavy ion-induced radiation damage in isotropic graphite studied by micro-indentation and in-situ electrical resistivity, Nuclear Instruments and Methods in Physics Research Section B: Beam Interactions with Materials and Atoms 365, Part B (2015) 509 – 514.

[74] C. Lemell, A. El-Said, W. Meissl, I. Gebeshuber, C. Trautmann, M. Toulemonde, J. Burgdörfer, F. Aumayr, On the nano-hillock formation induced by slow highly charged ions on insulator surfaces, Solid-State Electronics 51 (2007) 1398 – 1404. Special Issue: Papers Selected from the {NGC2007} Conference.

[75] C. Müller, A. Benyagoub, M. Lang, R. Neumann, K. Schwartz, M. Toulemonde, C. Trautmann, SFM study of ion-induced hillocks on lif exposed to thermal and optical annealing, Nuclear Instruments and Methods in Physics Research Section B: Beam Interactions with Materials and Atoms 209 (2003) 175 – 178. Fifth International Symposium on Swift Heavy Ions in Matter.

[76] A. El-Said, R. Neumann, K. Schwartz, C. Trautmann, Scanning force microscopy of heavy-ion induced damage in lanthanum fluoride single crystals, Surface and Coatings Technology 158 - 159 (2002) 522 – 525. Proceedings of the 12th International Conference on {SMMIB}.

[77] L. Nasdala, M. Wenzel, G. Vavra, G. Irmer, T. Wenzel, B. Kober, Metamictisation of natural zircon: accumulation versus thermal annealing of radioactivity-induced damage., Contributions to Mineralogy and Petrology 141 (2001) 125–144.

[78] L. Nasdala, G. Irmer, D. Wolf, The degree of metamictization in zircon: a Raman spectroscopic study, European Journal of Mineralogy 7 (1995) 471–478.

[79] M. Zhang, E. Salje, I. Farnan, A. Graeme-Barber, P. Daniel, R. Ewing, A. Clark, H. Leroux, Metamictization of zircon: Raman spectroscopic study, Journal of Physics: Condensed Matter 12 (2000) 1915–1925.

[80] B. Afra, M. D. Rodriguez, C. Trautmann, O. H. Pakarinen, F. Djurabekova, K. Nordlund, T. Bierschenk, R. Giulian, M. C. Ridgway, G. Rizza, N. Kirby, M. Toulemonde, P. Kluth, SAXS investigations of the morphology of swift heavy ion tracks in α-quartz, Journal of Physics: Condensed Matter 25 (2013) 045006.

[81] Mota-Santiago, P., Schauries, D., Nadzri, A., Vora, K., Ridgway, M. C., Kluth, P., Characterization of ion track morphology formed by swift heavy ion irradiation in silicon oxynitride films, EPJ Web of Conferences 91 (2015) 00008.

[82] J. O'Connell, R. Rymzhanov, V. Skuratov, A. Volkov, N. Kirilkin, Latent tracks and associated strain in Al_2O_3 irradiated with swift heavy ions, Nuclear Instruments and Methods in Physics Research Section B: Beam Interactions with Materials and Atoms 374 (2016) 97 – 101. Basic Research on Ionic-Covalent Materials.

[83] A. Meldrum, L. A. Boatner, R. C. Ewing, Electron-irradiation-induced nucleation and growth in amorphous $LaPO_4$, $ScPO_4$, and zircon, Journal of Materials Research 12 (1997) 1816–1827.

[84] A. Meldrum, L. A. Boatner, and R. C. Ewing, in Microstructure evolution during Irradiation, edited by I. M. Robertson, G. S. Was, L. W. Hobbs, and T. Diaz del la Rubia, MRS Symposia Proceedings No. 439, Materials Research Society, Pittsburgh, p. 697, 1997.

[85] M. R. Winter, D. R. Clarke, Oxide materials with low thermal conductivity, Journal of the American Ceramic Society 90 (2007) 533–540.

[86] C. Weise, K. G. van den Boogaart, R. Jonckheere, L. Ratschbacher, Annealing kinetics of Kr-tracks in monazite: Implications for fission-track modelling, Chemical Geology 260 (2009) 129 – 137.

[87] K. Gowda, F. Karioris, L. Cartz, T. Ehlert, Annealing of radiation damaged monazite, American Society for Testing and Materials, Special Technical Publication (1982) 799 – 805.

[88] M. R. Rafiuddin, A. P. Grosvenor, Probing the effect of radiation damage on the structure of rare-earth phosphates, Journal of Alloys and Compounds 653 (2015) 279 – 289.

[89] N. A. Medvedev, K. Schwartz, C. Trautmann, A. E. Volkov, Formation of the defect halo of swift heavy ion tracks in LiF due to spatial redistribution of valence holes, Physica Status Solidi (B) 250 (2013) 850–857.

[90] N. Medvedev, A. Volkov, B. Ziaja, Electronic and atomic kinetics in solids irradiated with free-electron lasers or swift-heavy ions, Nuclear Instruments and Methods in Physics Research Section B: Beam Interactions with Materials and Atoms 365, Part B (2015) 437 – 446.

[91] S. O. Kucheyev, H. Boudinov, J. S. Williams, C. Jagadish, G. Li, Effect of irradiation temperature and ion flux on electrical isolation of GaN, Journal of Applied Physics 91 (2002) 4117–4120.

Anton Romanenko

Akademischer Lebenslauf

✉ an.romanenko@gsi.de

Persönliche Angaben

Geburt **13. Mai 1987**, *Energodar, Ukraine*

Academische Ausbildung

12/2010–08/2016 **Promotion**, *Materialwissenschaften/Festkörperphysik*, Technische Universität Darmstadt, Thema: Strahlenschäden durch Schwerionenbestrahlung in Seltenerd-Phosphaten / Radiation damage produced by swift heavy ions in rare earth phosphates

2008–2010 **Master**, *Angewandte Mathematik und Physik*, Moskauer Institut für Physik und Technologie, Moskau, Russische Föderation, Thema: Study of giant mechanical and thermal pseudoelasticity in the Ni-Mn-Ga alloy system.

06/2010 **Abschluss**: *Master of Science - Angewandte Mathematik und Physik*

2004–2008 **Bachelor**, *Angewandte Physik*, Nationale Universität für Luftfahrt, Kiew, Ukraine, Thema: The effect of elasticity and superelasticity in nonstochiometric $Ni_xMn_yGa_z$-based alloys.

06/2008 **Abschluss**: *Bachelor of Science - Angewandte Physik.*

Schulische Ausbildung

2002–2004 **Vollständige mittlere Allgemeinbildung**, *Die Mittelschule in der Russischen Botschaft in der Islamischen Republik Iran, Stadt Teheran*

1994–2002 **Grund mittlere Allgemeinbildung**, *Schule Nr.3 der Stadt Energodar*

Berufspraxis

12/2010–08/2016 **Doktorand**, *GSI Helmholtzzentrum für Schwerionenforschung*, Darmstadt

08/2008–01/2010 **IT-Tester/QA-Engineer**, *CyberVision, Inc.*, Kiew

09/2007–07/2010 **Ingenieur (1/2 Stelle)**, *G. V. Kurdyumov Institute for Metal Physics, The National Academy of Sciences of Ukraine*, Kiew

09/2005–08/2007 **studentische Hilfskraft**, *Institute of Engineering Thermophysics of National Academy of Sciences of Ukraine*, Kiew

Publikationen

A. Romanenko, M. Lang, W. Li, R. C. Ewing, L. A. Boatner, F. Fujara, C. Trautmann, *Raman spectroscopy study of radiation damage produced by 2.1 GeV Au ions in holmium and neodymium orthophosphates*, prepared for submission

M. Cassinelli, A. Romanenko, H. Reith, F. Völklein, W. Sigle, C. Trautmann, M. E. Toimil-Molares, *Low temperature annealing effects on the stability of Bi nanowires*, Phys. Status Solidi A, Volume 213, Issue 3
p. 485-838, 2016

C. Hubert, K. O. Voss, M. Bender, K. Kupka, A. Romanenko, D. Severin, C. Trautmann, M. Tomut, *Swift heavy ion-induced radiation damage in isotropic graphite studied by micro-indentation and in-situ electrical resistivity*, Nuclear Instruments and Methods in Physics Research B, Volume 365, Part B
p. 509-514, 2015

K. Kupka, M. Tomut, P. Simon, C. Hubert, A. Romanenko, B. Lommel, C. Trautmann, *Intense heavy ion beam-induced temperature effects in carbon-based stripper foils*, J Radioanal Nucl Chem, Volume 305, Issue 3
p. 875-882, 2015

S. Dedera, M. Burchard, U. A. Glasmacher, N. Schoppner, C. Trautmann, D. Severin, A. Romanenko, C. Hubert, *On-line Raman spectroscopy of calcite and malachite during irradiation with swift heavy ions*, Nuclear Instruments and Methods in Physics Research B, Volume 365, Part B
p. 564-568, 2015

I. N. Glavatskyy, A. Romanenko, D. A. Musienko, N. I. Glavatska, *Giant Elasticity in the Ni-Mn-Ga Single Crystalline Shape-Memory Martensites*, XIX St.-Petersburg Readings About the Problems of Strength, St.-Petersburg, Russia, Volume 1, p. 266-269
2010

Publikationen: Jahresberichte

A. Romanenko, C. Trautmann, F. Fujara, M. Lang, *Swift heavy ion induced radiation damage in $EuPO_4$*, GSI Report 2014-1, 177 p. (2014)

A. Romanenko, M. Lang, F. Fujara, C. Trautmann, *Swift heavy ion induced radiation damage of $TmPO_4$*, GSI Report 2013-1, 389 p. (2013)

C. Hubert, M. Tomut, K. Kupka, A. Romanenko, B. Schuster, H.-P. Liermann, C. Trautmann, *High-Resolution Synchrotron X-Ray Diffraction of Swift Heavy Ion Irradiated Graphite*, GSI Report 2013-1, 408 p. (2013)

International conferences: poster

A. Romanenko, C. Trautmann, F. Fujara, M. Lang, *Raman spectroscopy analysis on swift heavy ion irradiated $HoPO_4$*, Workshop für Ionenstrahlen und Nanostrukturen 2015

A. Romanenko, F. Fujara, M. Lang, C. Trautmann, *Raman spectroscopy study of radiation damage produced by 2.1 GeV Au ions in holmium and neodymium orthophosphates*, Deutsche Tagung für Forschung mit Synchrotronstrahlung, Neutronen und Ionenstrahlen an Großgeräten 2014

A. Romanenko, C. Trautmann, *Swift heavy ion irradiation of xenotime and monazite - structured $REEPO_4$ compounds at ambient and lifted pressures*, Joint ICTP-IAEA Workshop on Physics of Radiation Effect and its Simulation for Non-Metallic Condensed Matter, 2012

Schools, workshops and travel grants

Workshop für Ionenstrahlen und Nanostrukturen, Heidelberg, Deutschland, 2015

"HGS-HIRe Abroad"grant for a research stay at the University of Michigan, Ann Arbor, USA, 2013

The 1st Workshop on Materials in Extreme Environments - MatX, Michigan, USA, 2013

Joint ICTP-IAEA Workshop on Physics of Radiation Effect and its Simulation for Non-Metallic Condensed Matter, Trieste, Italy, 2012

International school: Raman spectroscopy applied to earth sciences and cultural heritage, Nancy, France, 2012

43rd IFF Spring School Scattering Methods for Condensed Matter Research: Towards Novel Applications at Future Sources, Jülich, Germany, 2012

Soft skill trainings

HGS-HIRe soft skill course: "Leadership and Career Development", 2014

HGS-HIRe soft skill course: "Leading Teams in a Research Environment", 2013

HGS-HIRe soft skill course: "Making an Impact as an Effective Researcher", 2012